



저작자표시-비영리-변경금지 2.0 대한민국

이용자는 아래의 조건을 따르는 경우에 한하여 자유롭게

- 이 저작물을 복제, 배포, 전송, 전시, 공연 및 방송할 수 있습니다.

다음과 같은 조건을 따라야 합니다:



저작자표시. 귀하는 원저작자를 표시하여야 합니다.



비영리. 귀하는 이 저작물을 영리 목적으로 이용할 수 없습니다.



변경금지. 귀하는 이 저작물을 개작, 변형 또는 가공할 수 없습니다.

- 귀하는, 이 저작물의 재이용이나 배포의 경우, 이 저작물에 적용된 이용허락조건을 명확하게 나타내어야 합니다.
- 저작권자로부터 별도의 허가를 받으면 이러한 조건들은 적용되지 않습니다.

저작권법에 따른 이용자의 권리는 위의 내용에 의하여 영향을 받지 않습니다.

이것은 [이용허락규약\(Legal Code\)](#)을 이해하기 쉽게 요약한 것입니다.

[Disclaimer](#)

공학박사학위논문

**Nanopatterned 2D Materials**  
**using Block Copolymer Nano-Lithography**  
**for Superior Thermoelectrics**

블록공중합체의 나노 구조 제어를 통하여  
나노 패터닝된 이차원 물질의 열전 성능 극대화에 대한 연구

2018년 8월

서울대학교 대학원

화학생물공학부

오진우

**Nanopatterned 2D Materials**  
**using Block Copolymer Nano-Lithography**  
**for Superior Thermoelectrics**

**by**

**Jinwoo Oh**

**Adviser: Professor Jong-Chan Lee, Ph. D.**

**Submitted in Partial Fulfillment**  
**of the Requirements for the Degree of**  
**DOCTOR OF PHILOSOPHY**

**August, 2018**

**School of Chemical and Biological Engineering**  
**College of Engineering**  
**Graduate School**  
**Seoul National University**

## **Abstract**

This study presents fabrication and characterization of nano patterned low dimensional materials fabricated from block copolymer (BCP) self-assembly and nano lithography and application to the thermoelectrics. Also the thermoelectric generator from conductive polymer and rubbery BCP is prepared and applied to the self-powered devices. Firstly, universal method to prepare perpendicular BCP nanopattern is introduced. Universal solution for 3 different BCP including polystyrene-b-poly(methyl methacrylate) (PS-b-PMMA), polystyrene-b-polydimethylsiloxane (PS-b-PDMS) and polystyrene-b-poly(2-vinylpyridine) (PS-b-P2VP) is adopted to produce perpendicular micro domain. Short time plasma treatment was applied to the top surface of BCP which initiate the crosslinking reaction to produce crosslinking layer. The crosslinking layer exhibits physical immobilization effect to both BCP blocks. The crosslinking layer also applied to the bottom layer replacing random copolymer brush, and the bottom layer can act as a neutral layer to the BCP film. The perpendicular nanopattern from 3 different BCP was observed with scanning electron microscope (SEM) and grazing intensity small angle x-ray scattering (GI-SAXS). BCP with plasma treatment of both top and bottom has fully-perpendicular orientation from the bottom to the top. The

crosslinking layer on the top surface is more stiff than neat BCP, the wrinkle is induced after annealing process. In this reason, the thickness of crosslinking layer is controlled by varying the intensity and time of plasma treatment.

Secondary, graphene nano structure was fabricated from BCP self-assembly. The large graphene up to 2 centimeter scale was fabricated from chemical vapor deposition (CVD) and nano patterned using PS-b-P2VP sphere nanopattern. Thermoelectric properties of the graphene nanomesh structure with controlled neck width is enhanced up to 40 times higher than pristine graphene. The Seebeck coefficient of the bilayer graphene nanomesh with 8 nm neck width shows the highest value of  $\sim 520 \mu\text{V/K}$  among the graphene-related materials. The thermal conductivity of suspended graphene nanomesh is reduced to  $\sim 78 \text{ W/m}\cdot\text{K}$  which is the lowest thermal conductivity for graphene nanostructure. Classical and quantum mechanical calculations supported my nanomesh approach, which can achieve high thermal properties based on reduced thermal conductivity and higher thermopower due to the confined geometry. Also the heterostructure of graphene nanostructure and transition metal dicalcogenides was introduced. Molybdenum disulfide ( $\text{MoS}_2$ ) has extremely high Seebeck coefficient and low thermal conductivity, however, very low electrical conductivity. To enhance the electrical conductivity selectively, graphene nanoribbon is adopted as an “electron highways” to the  $\text{MoS}_2$  thin film. The large area graphene nanoribbon was fabrication from block copolymer

lithography, and was transferred to the MoS<sub>2</sub> atomic layer. The graphene nanostructure significantly enhances the electrical conductivity of the MoS<sub>2</sub> atomic layer more than 1000 times higher. We show that with heterostructure, the thermoelectric properties can be enhanced.

Finally, PEDOT:PSS with coaxial strut was introduced for thermoelectric generator applications. The increment of the data communication between machine to machine, machine to human and human to human leads the requirement of collecting data from any kinds of sensors. One of the most important sensor is pressure sensor which can give information of blood pressure, heart beating rate or something. And the electric energy source is required to these kinds of electric devices, and the energy source is also needed to be flexible for the wearable electric devices. Recently, wearable thermoelectric generator based on organic materials are reported and the wearable TEG can generate several microwatt energies. However, to apply these wearable TEG, any kind of electric device should be assembled together with TEG. We introduced coaxial structure for thermoelectric generator. It is found that shell structure of SEBS give the mechanical strength and recovery properties to the foam and PEDOT:PSS is well-known thermoelectric polymer which have moderate thermopower and high electrical conductivity and used to the thermoelectric foam structure for thermoelectric generator. This SPM was

assembled to the wearable thermoelectric generator and could generate 338 nW from the forearm.

Keywords : Block copolymer, Nanopattern, Lithography, Graphene, 2D Materials, Heterostructure, Thermoelectric, Wearable, Sensors

Student Number: 2014-30252

## **TABLE OF CONTENT**

<b>Abstract</b>	<b>i</b>
<b>List of Figures</b>	<b>ix</b>
<b>List of Tables</b>	<b>xv</b>

## **Chapter 1**

### **Introduction**

1.1 Block Copolymer Self-assembly for Nanolithography	2
1.2. 2 Dimensional Materials for Thermoelectrics and Size Effect in Low Dimensional Materials	4
1.3. Motivation	8
1.4. References	1 0

## **Chapter 2**

### **Control of Block Copolymer Nano Domains for Nanolithography**

2.1. Introduction	2 1
2.2. Experimental	2 4
2.3. Results and Discussion	2 7
2.4. Conclusion	3 4
2.5. References	3 5

## **Chapter 3**

### **Significantly reduced thermal conductivity and enhanced thermoelectric properties of single- and bi-layer graphene nanomeshes with sub-10 nm neck-width**

3.1. Introduction	5 8
3.2. Experimental	6 2

3.3. Results and Discussion	7 5
3.4. Conclusion	8 8
3.5. References	8 9

## **Chapter 4**

### **Van der Waals Heterostructure of Graphene Nanostructure and Molybdenum Disulfide for Superior Thermoelectric Materials**

4.1. Introduction	1 1 4
4.2. Experimental	1 1 7
4.3. Results and Discussion	1 2 1
4.4. Conclusion	1 2 4
4.5. References	1 2 5

## **Chapter 5**

### **Coaxial Struts and Microfractured Structures of Compressible Thermoelectric Foams for Self-powered Pressure Sensors**

5.1. Introduction	1 4 4
5.2. Experimental	1 4 7
5.3. Results and Discussion	1 5 2
5.4. Conclusion	1 6 1
5.5. Refences	1 6 2
<b>Abstract in Korean</b>	1 8 6

## List of Figures

Figure 1.1 Schematic illustration of block copolymer and its morphology	1 6
Figure 1.2 Schematic image of (a) graphene and (b) molybdenum disulfide	1 7
Figure 1.3 Density of state (DOS) for bulk, 2D, 1D and 0D materials.	1 8
Figure 1.4 Schematic image of phonon scattering at the edge or grain boundary	1 9
Figure 2.1 Schematic of the plasma topcoat assisted directional self-assembly method.	4 0
Figure 2.2 Chemical structure of PS-b-PDMS, PS-b-PMMA and PS-b-P2VP.	4 1
Figure 2.3 Low magnitude SEM image of PS-b-PDMS (11k – 5k)	4 2
Figure 2.4 High magnitude SEM image of PS-b-PDMS (11k – 5k)	4 3
Figure 2.5 SEM image of PS-b-PDMS nanopatterns with varied plasma power and treatment time.	4 4
Figure 2.6 Phase diagram of PS-b-PDMS nanopatterns with varied plasma power and treatment time at high argon flow.	4 5

Figure 2.7 SEM images of PS-b-PMMA nanopatterns with varied plasma power and treatment time.	4 6
Figure 2.8 SEM images of PS-b-PMMA nanopatterns with varied plasma power and treatment time.	4 7
Figure 2.9 Angle-resolved X-ray photoelectron spectroscopy of Ar plasma treated PS-b-PMMA pattern.	4 8
Figure 2.10 Carbon ratio at ester group of Ar plasma treated PS-b-PMMA pattern detected by angle-resolved X-ray photoelectron spectroscopy.	4 9
Figure 2.11 Phase diagram of PS-b-PMMA nanopatterns with varied plasma power and treatment time.	5 0
Figure 2.12 SEM image of SML (a, d), SDC (b, e) and SVL (c, f) after thermal annealing.	5 1
Figure 2.13 Schematic of the top and bottom plasma treatment to prepare fully-perpendicular orientation to the BCP film.	5 2
Figure 2.14 SEM image of nano patterns with different morphology	5 3
Figure 2.15 GI-SAXS image for PS-b-PDMS (a-c) and PS-b-PMMA (d-f)	5 4
Figure 2.16 SEM image of top plasma treated PS-b-PDMS after solvent annealing.	5 5

Figure 2.17 XPS results for PS-b-PMMA, PS-b-PDMS and PS-b-P2VP with and without surface crosslinking layer.	5 6
Figure 3.1 Fabrication and thermal measurements of a sub-10 nm GNM.	1 0 0
Figure 3.2 Structures of the GNM	1 0 1
Figure 3.3 Neck width and porosity of the GNMs. Neck width and porosity of the SGNMs and BGNMs as a function of RIE time from the image analysis.	1 0 2
Figure 3.4 Raman spectra and mapping image of the GNMs.	1 0 3
Figure 3.5 Thermal conductivity of the suspended SLG, BLG, SGNM and BGNM using an optothermal Raman technique	1 0 4
Figure 3.6 Electric and thermoelectric properties of graphenes and GNMs.	1 0 5
Figure 3.7 Theoretical prediction of thermal conductivity and thermoelectric properties of graphenes and GNMs.	1 0 6
Figure 3.8 (a) Optical microscope image and (b) SEM image of edge area between CVD grown single layer graphene (SLG) and repeatedly transferred bilayer graphene (BLG) on SiO <sub>2</sub> (100 nm)/Si substrates.	1 0 7
Figure 3.9 The radius of (a, c) neck width and (b, d) pore diameter of (a, b) SGNM and (c, d) BGNM as a function of RIE time.	1 0 8

Figure 3.10 Arrhenius plot for the conductivity of a, SGNM12 and b, BGNM8 plotted with respect to the inverse of the operating temperature from 150 K to 300 K.	1 0 9
Figure 3.11 (a) Structure and (b and c) theoretical prediction of thermal conductivity and thermoelectric properties of graphenes and GNMs.	1 1 0
Figure 3.12 Raman intensity at 520 cm <sup>-1</sup> of cleaved Au/Si substrate	1 1 1
Figure 3.13 The fabrication process of cross-shaped isolated mesh area and source and drain electrodes of the GNM FETs using E-beam lithography.	1 1 2
Figure 4.1 Preparation of GNR/MoS <sub>2</sub> heterostructure	1 3 0
Figure 4.2 Schematic image of GNR/MoS <sub>2</sub> heterostructure	1 3 1
Figure 4.3 Schematic image of preparation of GNR/MoS <sub>2</sub> heterostructure	1 3 2
Figure 4.4 Raman spectroscopy of GNR/MoS <sub>2</sub> heterostructure	1 3 3
Figure 4.5 Raman mapping of GNR/MoS <sub>2</sub> heterostructure.	1 3 4
Figure 4.6 TEM image and SAED pattern of GNR/MoS <sub>2</sub> heterostructure	1 3 5
Figure 4.7 The electrical conductivity of GNR/MoS <sub>2</sub> heterostructure	1 3 6
Figure 4.8 SEM image of GNR with different linewidth	1 3 7

Figure 4.9 Film thickness and line width versus etching time	1 3 8
Figure 4.10 Raman spectroscopy of GNR with different etching time	1 3 9
Figure 4.11 Schematic image of preparing GNR/MoS2 heterostructure	1 4 0
Figure 4.12 Schematic image of preparing MoS2 and SEM image of MoS2 on substrate.	1 4 1
Figure 4.13 Basic properties of CVD graphene.	1 4 2
Figure 5.1 Schematic image of preparing coaxial 3D cellular conductor with micro-fractured morphology	1 7 0
Figure 5.2 (a-c) SEM image of melamine foam (MF), PEDOT:PSS infiltrated foam (PM), and PM covered with SEBS (SPM)	1 7 1
Figure 5.3 Characteristics of the PEDOT:PSS-melamine (PM) foam and SEBS-PEDOT:PSS-melamine (SPM) foam with differently repetitive PEDOT:PSS infiltration process	1 7 2
Figure 5.4 Thermoelectric module of SPM5.	1 7 3
Figure 5.5 Resistance change under pressure of (a) PM and (b) SPM	1 7 4
Figure 5.6 Pressure sensing performance of 95% compressed PM and SPM foams	1 7 5

Figure 5.7 (a) Digital image of self-powered pressure sensor test and (b) I/I0 with repeated pressure loading and unloading test under temperature difference of 50 K.

1 7 6

Figure 5.8 The strut widths as a function of PEDOT:PSS infiltration times. 1 7 7

Figure 5.9 SEM image of PM (a, b) and SPM (c, d) after repeated pressure loading and unloading test. 1 7 8

Figure 5.10 (a) Schematic image of PM foam with measurement direction, (b) relative electrical conductivity, thermal conductivity and Seebeck coefficient against to horizontal direction (x-axis). 1 7 9

Figure 5.11 Digital image of SPM1 and laterally compressed SPM1 foam. SPM1 is compressed with external strain machine. 1 8 0

Figure 5.12 Digital images of PM and SPM. (a) The digital image of MF and PM with different infiltration number. 1 8 1

Figure 5.13 Pressure-sensing performance of 95%-compressed SPM foams with different thickness of PEDOT:PSS conductive path. 1 8 2

Figure 5.14 Pressure-sensing performance of 95%-compressed SPM3 and SPM5. 1 8 3

Figure 5.15 The measured I-V curves of self-powered pressure sensor based on 9 of SPM5 cells. 1 8 4

Figure 5.16 Fatigue test setup with moving coil linear stage to evaluate the durability of the sensor

1 8 5

# **Chapter 1**

## **Introduction**

## 1.1 Block Copolymer Self-assembly for Nanolithography

Directed self-assembly of block copolymer is a strategy for patterning at a sublithographic resolution in which self-assembly block copolymers multiply the density of features in comparison with a lithographically derived template[1–3]. On chemical patterns generated from 193 nm immersed photolithography with an 85 nm pitch, for example, directed self-assembly of polystyrene-block-poly(methyl methacrylate) (PS-*b*-PMMA) with a 28 nm pitch line pattern has been demonstrated with extremely low levels of defects, approaching those required for semiconductor manufacturing. Unfortunately, PS-*b*-PMMA as a resolution limit approximately 11 nm. Therefore, it is imperative to investigate block copolymers with higher  $\chi$  (Flory-Huggins interaction parameter) than PS-*b*-PMMA to achieve sub-10-nm features. However, for most block copolymers, except for PS-*b*-PMMA, the constituent blocks have considerably dissimilar surface energies, which thus precludes facile assembly of perpendicular micro domains. Block copolymer (BCP) self-assembly has attracted considerable attention for many decades because it can yield ordered structures in a wide range of morphologies, including spheres, cylinders, bicontinuous structures, lamellae, vesicles, and many other complex or hierarchical assemblies. These aggregates provide potential or practical applications in many fields. The present tutorial review introduces the primary

principles of BCP self-assembly in bulk and in solution, by describing experiments, theories, accessible morphologies and morphological transitions, factors affecting the morphology, thermodynamics and kinetics, among others.

The formation of thermodynamically stable BCP aggregates of various morphologies is governed by three contributions to the free energy of the system: the degree of stretching of the core-forming blocks, the interfacial tension between the micelle core and the solvent outside the core, and the repulsive interactions among corona-forming chains. The morphologies can therefore be controlled by factors affecting any of the three contributions, e.g. through variations in copolymer composition and concentration, water content in the solution, nature of the common solvent, presence of additives such as ions or homopolymers, etc. The present section discusses some of the major factors that influence the morphology of the aggregates, and gives the possible reasons for their effectiveness, focusing on PS-b-PAA systems.

## 1.2. 2 Dimensional Materials for Thermoelectrics and Size Effect in Low Dimensional Materials

Graphene, 2 Dimensional materials which have great potential in microelectronics due to its superior properties such as high electrical conductivity[4–7], zero bandgap structure and thin layer thickness. For further applications, tuning the properties of graphene is required. In this reason, several approaches are tried such as to fabricate graphene bilayer, graphene nana ribbon structure or graphene nanomesh structures. However, due to the difficulties of fabrication and handling atomic layers of nano patterned graphene derivatives, experimental study is still limited.

From the theoretical studies, graphene based nano patterns could have higher figure of merits (ZT) in thermoelectrics. The Mott relation is[8,9]

$$S = \frac{\pi^2 k_B}{3 q} k_B T \left( \frac{d[\ln(\sigma(E))]}{dE} \right)_{E=E_F}$$

From the equation, the Seebeck coefficient, S is related to the differential of density of state. The differential of density of state dramatically increased with the decrement of feature size. Due to the quantum confinement effect, the Seebeck

coefficient of nano materials such as quantum dots, quantum wires and quantum wells has much higher than that of 3D bulk materials[7,10,11].

The thermal conductivity is the property of a material to conduct heat. It is evaluated primarily in terms of the Fourier's Law for heat conduction. In general, thermal conductivity is a tensor property, expressing the anisotropy of the property[12,13]. Heat transfer occurs at a lower rate in materials of low thermal conductivity than in materials of high thermal conductivity. Correspondingly, materials of high thermal conductivity are widely used in heat sink applications and materials of low thermal conductivity are used as thermal insulation[13,14]. The thermal conductivity of a material may depend on temperature. The effect of temperature on thermal conductivity is different for metals and nonmetals. In metals, heat conductivity is primarily due to free electrons. Following the Wiedemann–Franz law, thermal conductivity of metals is approximately proportional to the absolute temperature (in kelvins) times electrical conductivity. In pure metals the electrical conductivity decreases with increasing temperature and thus the product of the two, the thermal conductivity, stays approximately constant. However, as temperatures approach absolute zero, the thermal conductivity decreases sharply.[12]

On the other hand, heat conductivity in nonmetals is mainly due to lattice vibrations (phonons). Except for high quality crystals at low temperatures, the

phonon mean free path is not reduced significantly at higher temperatures[13]. Thus, the thermal conductivity of nonmetals is approximately constant at high temperatures. At low temperatures well below the Debye temperature, thermal conductivity decreases, as does the heat capacity, due to carrier scattering from defects at very low temperatures.

Umklapp scattering (also U-process or Umklapp process) is the transformation, like a reflection or a translation, of a wave vector to another Brillouin zone as a result of a scattering process, for example an electron-lattice potential scattering or an anharmonic phonon-phonon (or electron-phonon) scattering process, reflecting an electronic state or creating a phonon with a momentum k-vector outside the first Brillouin zone. Umklapp scattering is one process limiting the thermal conductivity in crystalline materials, the others being phonon scattering on crystal defects and at the surface of the sample. In case of nano materials or nano patterned materials, the thermal conductivity is suppressed by phonon umklapp scattering.

Boundary scattering is particularly important for low-dimensional nanostructures and its relaxation time is given by:

$$\frac{1}{\tau_B} = \frac{V}{D} (1 - p)$$

where D is the dimension of the system and p represents the surface roughness parameter. The value p=1 means a smooth perfect surface that the scattering is

purely specular and the relaxation time goes to  $\infty$ ; hence, boundary scattering does not affect thermal transport. The value  $p=0$  represents a very rough surface that the scattering is then purely diffusive which gives:

$$\frac{1}{\tau_B} = \frac{V}{D}$$

This equation is also known as Casimir limit[15].

### **1.3. Motivation**

Researchers calculate the electric and thermal properties of low dimensional material with nano patterns including band structure, electrical conductivity, thermal conductivity and thermoelectric properties. However hence the difficulties in preparations and handling nano engineered 2 D material make huddle to the experimental researches. From the block copolymer nanolithography, large area periodic pattern with 5 to 100 nm pattern can be transferred to 2 D materials. To prove the enhancement in thermoelectrics by introducing nano patterns to the 2 D materials, the concept of my thesis was fixed: firstly, preparation of perpendicular block copolymer micro domain for nanolithography, secondly, fabrication nano patterns on 2 D materials to transfer periodic morphology to thin films, and lastly, characterization of the thermoelectric properties, electrical properties and thermal properties of nano patterned 2 D materials. This is the first study of measuring the characteristic nano patterned 2 D materials in centimeter scale.[16]

By changing the gear, thermoelectric generator based on micro structures with conducting polymer and rubbery block copolymer is produced for self-powered pressure sensor. The uses of thermoelectric generator for wearable devices are

considered hence the increment of the data collecting and exchanging between human to human, human to device, device to device. The requirement of steady data collection, the power consumed by sensor is one of the main problem to be solved. It is necessary to have larger batteries or be combined with power generator module for actual applications. Here, new concept of self-powered pressure sensor based on fracture design of coaxial structure of thermoelectric material is introduced[17,18]. By introducing other 2 D materials to the coaxial structure with shell which keeps the 2 D materials from delamination, the coaxial structure is more powerful approaches for wearable thermoelectric applications.

## 1.4. References

- [1] C. J. Hawker, T. P. and P. Thomas, "Block Copolymer Lithography : Merging ' Bottom- Up ' with ' Top- Down ' Processes," *MRS Bull.*, vol. 30, no. December, pp. 952–966, 2005.
- [2] J. K. Cheng, C. T. Rettner, D. P. Sanders, H. C. Kim, and W. D. Hinsberg, "Dense self-assembly on sparse chemical patterns: Rectifying and multiplying lithographic patterns using block copolymers," *Adv. Mater.*, vol. 20, no. 16, pp. 3155–3158, 2008.
- [3] I. Bitai, J. K. W. Yang, Y. S. Jung, C. A. Ross, E. L. Thomas, and K. K. Berggren, "Graphoepitaxy of Self-Assembled Block Copolymers on Two-Dimensional Periodic Patterned Templates," *Science (80-. )*, vol. 321, no. August, pp. 939–944, 2008.
- [4] S.-J. Choi, M. P. Kim, S.-J. Lee, B. J. Kim, and I.-D. Kim, "Facile Au catalyst loading on the inner shell of hollow SnO<sub>2</sub> spheres using Au-decorated block copolymer sphere templates and their selective H<sub>2</sub>S sensing characteristics," *Nanoscale*, vol. 6, no. 20, pp. 11898–11903, 2014.
- [5] D. E. Angelescu, J. H. Waller, D. H. Adamson, R. A. Register, and P. M. Chaikin, "Enhanced order of block copolymer cylinders in single-layer films using a sweeping solidification front," *Adv. Mater.*, vol. 19, no. 18, pp. 2687–2690, 2007.

- [6] S. Ham et al., "Microdomain Orientation of PS- b -PMMA by Controlled Interfacial Interactions," *Macromolecules*, vol. 41, no. 17, pp. 6431–6437, 2008.
- [7] J. P. Yang, S. B. Qadri, and B. R. Ratna, "Structural and morphological characterization of PbS nanocrystallites synthesized in the bicontinuous cubic phase of a lipid," *J. Phys. Chem.*, vol. 100, no. 43, pp. 17255–17259, 1996.
- [8] Y. Wang et al., "Nanoporous metal membranes with bicontinuous morphology from recyclable block-copolymer templates," *Adv. Mater.*, vol. 22, no. 18, pp. 2068–2072, 2010.
- [9] G. Liu et al., "Epitaxial graphene nanoribbon array fabrication using BCP-assisted nanolithography," *ACS Nano*, vol. 6, no. 8, pp. 6786–6792, 2012.
- [10] A. Laiho, P. Hiekkataipale, J. Ruokolainen, and O. Ikkala, "Directing the smectic layer orientation by shear flow in hierarchical lamellar-withinlamellar liquid crystalline diblock copolymers," *Macromol. Chem. Phys.*, vol. 210, no. 15, pp. 1218–1223, 2009.
- [11] Q. Chen, H. Schönherr, and G. J. Vancso, "Block-copolymer vesicles as nanoreactors for enzymatic reactions," *Small*, vol. 5, no. 12, pp. 1436–1445, 2009.

- [12] B. Yan, D. Han, O. Boissière, P. Ayotte, and Y. Zhao, “Manipulation of block copolymer vesicles using CO<sub>2</sub>: dissociation or ‘breathing,’” *Soft Matter*, vol. 9, no. 6, p. 2011, 2013.
- [13] T. Hirai, M. Leolukman, T. Hayakawa, M. A. Kakimoto, and P. Gopalan, “Hierarchical nanostructures of organosilicate nanosheets within self-organized block copolymer films,” *Macromolecules*, vol. 41, no. 13, pp. 4558–4560, 2008.
- [14] Y. H. Ha et al., “An orientationally ordered hierarchical exfoliated clay-block copolymer nanocomposite,” *Macromolecules*, vol. 38, no. 12, pp. 5170–5179, 2005.
- [15] L. Zhang and A. Eisenberg, “Multiple Morphologies of ‘Crew-Cut’ Aggregates of Polystyrene-*b*-poly (acrylic acid) Block Copolymers,” *Science* (80-. ), vol. 268, no. 5218, pp. 1728–1731, 1995.
- [16] C. Allen, D. Maysinger, and A. Eisenberg, “Nano-engineering block copolymer aggregates for drug delivery,” *Colloids Surfaces B Biointerfaces*, vol. 16, no. 1–4, pp. 3–27, 1999.
- [17] Y. Huang and D. R. Paul, “Effect of Molecular Weight and Temperature on Physical Aging of Thin Glassy Poly(2,6-dimethyl-1,4-phenylene oxide) Films,” *J. Polym. Sci. Part B Polym. Phys.*, vol. 45, no. April, pp. 1390–1398, 2007.

- [18] D. Yan, K. Dai, Z. Xiang, Z. Li, X. Ji, and W. Zhang, “Electrical Conductivity and Major Mechanical and Thermal Properties of Carbon Nanotube-Filled Polyurethane Foams,” *J. Appl. Polym. Sci.*, vol. 120, pp. 3014–3019, 2011.
- [19] X. Li et al., “Large area synthesis of high quality and uniform graphene films on copper foils,” *Science (80-. )*, vol. 324, no. 5932, pp. 1312–1314, 2009.
- [20] C. Lee, X. Wei, J. W. Kysar, and J. Hone, “Measurement of the elastic properties and intrinsic strength of monolayer graphene,” *Science (80-. )*, vol. 321, no. July, pp. 385–388, 2008.
- [21] R. R. Nair et al., “Fine structure constant defines visual transparency of graphene,” *Science (80-. )*, vol. 320, no. 5881, p. 1308, 2008.
- [22] K. S. Novoselov et al., “Two-dimensional gas of massless Dirac fermions in graphene,” *Nature*, vol. 438, no. 7065, pp. 197–200, 2005.
- [23] M. P. Zaitlin and A. C. Anderson, “Phonon thermal transport in noncrystalline materials,” *Phys. Rev. B*, vol. 12, no. 10, pp. 4475–4486, 1975.
- [24] K. S. Kim et al., “Large-scale pattern growth of graphene films for stretchable transparent electrodes,” *Nature*, vol. 457, no. 7230, pp. 706–710, 2009.

- [25] Y. Zhang, Y. W. Tan, H. L. Stormer, and P. Kim, “Experimental observation of the quantum Hall effect and Berry’s phase in graphene,” *Nature*, vol. 438, no. 7065, pp. 201–204, 2005.
- [26] T. Löfwander and M. Fogelström, “Impurity scattering and Mott’s formula in graphene,” *Phys. Rev. B - Condens. Matter Mater. Phys.*, vol. 76, no. 19, pp. 10–13, 2007.
- [27] O. Bubnova et al., “Optimization of the thermoelectric figure of merit in the conducting polymer poly ( 3 , 4-ethylenedioxythiophene ),” *Nat. Mater.*, vol. 10, no. 6, pp. 429–433, 2011.
- [28] G. K. Chang and R. E. Jones, “Low-Temperature Thermal Conductivity of Amorphous Solids,” *Phys. Rev.*, vol. 126, no. 6, pp. 2055–2058, 1962.
- [29] M. P. Zaitlin, L. M. Scherr, and A. C. Anderson, “Boundary scattering of phonons in noncrystalline materials,” *Phys. Rev. B*, vol. 12, no. 10, pp. 4487–4492, 1975.
- [30] J. Y. Kim, J.-H. Lee, and J. C. Grossman, “Thermal transport in functionalized graphene.,” *ACS Nano*, vol. 6, no. 10, pp. 9050–9057, 2012.

- [31] A. J. Minnich, M. S. Dresselhaus, Z. F. Ren, and G. Chen, “Bulk nanostructured thermoelectric materials: current research and future prospects,” *Energy Environ. Sci.*, vol. 2, no. 5, p. 466, 2009.
- [32] F. Zhang, Y. Zang, D. Huang, C. Di, and D. Zhu, “frame-supported organic thermoelectric materials,” *Nat. Commun.*, vol. 6, no. May, pp. 1–10, 2015.
- [33] M. Hyland, H. Hunter, J. Liu, E. Veety, and D. Vashaee, “Wearable thermoelectric generators for human body heat harvesting,” *Appl. Energy*, vol. 182, pp. 518–524, 2016.

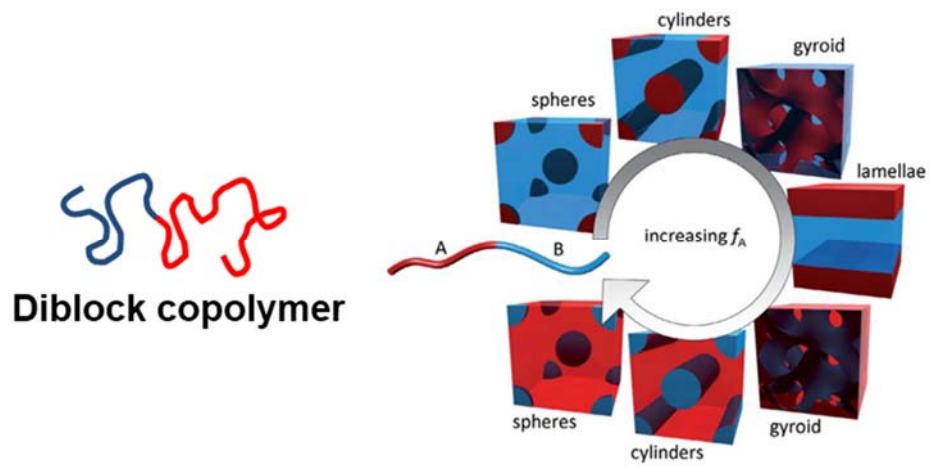
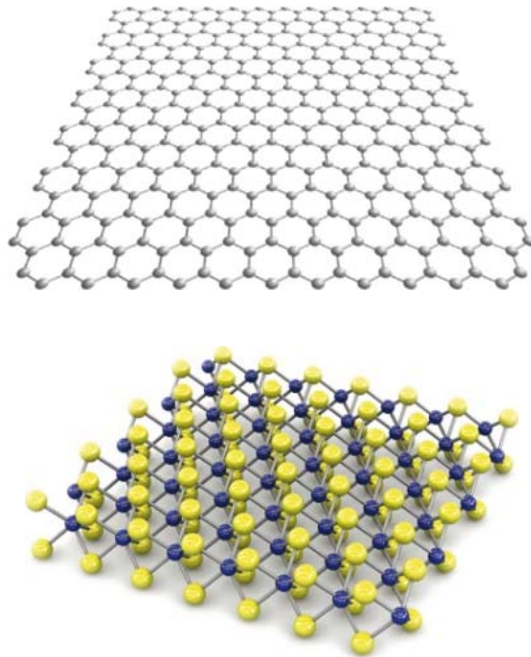
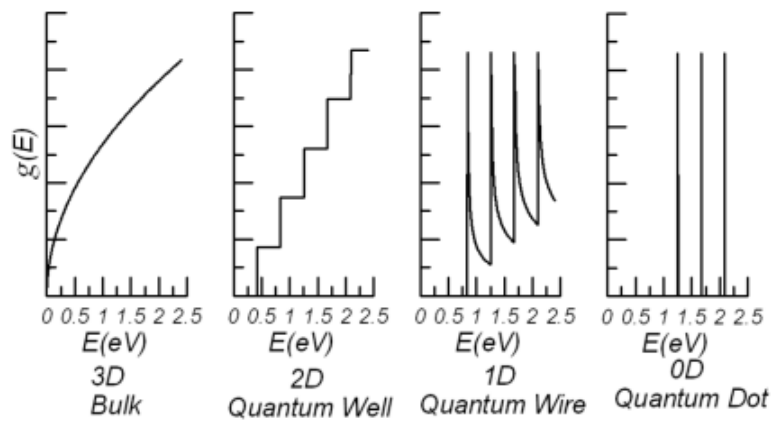


Figure 1.1. Schematic illustration of block copolymer and its morphology



**Figure 1.2. Schematic image of (a) graphene and (b) molybdenum disulfide**



**Figure 1.3. Density of state (DOS) for bulk, 2D, 1D and 0D materials.**

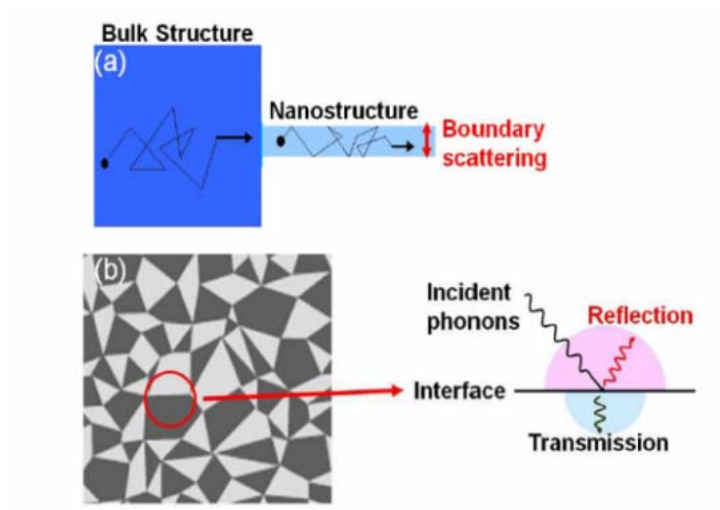


**Figure 1.4. Schematic image of phonon scattering at the edge or grain boundary**

## **Chapter 2**

# **Control of Block Copolymer Nano Domains for Nanolithography**

## 2.1. Introduction

Sub-10 nm pattern prepared by directed self-assembly (DSA) of block copolymer (BCP) thin film is a breakthrough for the sub-lithography with densely packed nano patterns. In BCP thin film, the interfacial energy is critical value for the perpendicular orientation of micro domains. Several approaches produced neutral surface to both interfaces of BCP, however, it is restricted to certain kinds of BCP. Here, we introduced universal solution for the BCP to have the perpendicular micro domain with short and strong plasma treatment to the BCP interfaces. By crosslinking the surface of the BCP not only keeps the BCP immobilized, but also produces the layer with neutral surface energy to both interfaces of BCP. Crosslinked layers of different BCP species were induced by flash plasma and change the orientation of the BCP micro domain from parallel to fully-perpendicular direction. Quick, simple and universal method have ability to prepare perpendicular orientation to any kind of BCP with different  $\chi$  parameters.

Perpendicular micro domain of the block copolymer (BCP) from directed self-assembly (DSA) is breakthrough for patterning at a sublithographic resolution in which the self-assembled BCP could prepare sub-10 nm pattern with higher packing density[1]–[4]. With optical lithography, 193 nm pattern could be served with 65 nm half-pitch structure only[5]. On the other hand, DSA of BCP could prepare

narrower patterns, for example, polystyrene-block-poly(methyl methacrylate) (PS-b-PMMA) with 27 nm half-pitch dot patterns[6] and polystyrene-block-poly(dimethyl siloxane) with 18 nm half-pitch dot and line patterns[7], [8] have been demonstrated with low level of density. In polymeric thin film, one of the internal factor which affects to the pattern size is  $\chi$  (Flory–Huggins interaction parameter), and PS-b-PMMA has a resolution limit of approximately 11 nm for its low  $\chi$ [9]–[11]. BCP with higher  $\chi$  shows narrower feature size, however, the preference for one of the blocks to the surface occurs. Eventually, with conventional annealing method, BCP with high  $\chi$  has parallel patterns on surfaces[7], [8], [12]. Several approaches have been suggested to overcome the surface energy difference such as introduction of random copolymer with similar surface energy to the top and the bottom[13], [14], solvent annealing with neutral surface energy[7], [12] and applying electric[15] or magnetic fields[16].

In case of the top coat layer, the random copolymer designed for the certain BCP, is a well-studied method to prepare neutral surface and perpendicular orientations[17], [18]. The problem of top coat approach is that the top coat is limited to certain BCP films. To solve the problem of the random copolymer top coat, Suh et al. introduced chemical vapor deposition to deposit a topcoat grafting on the BCP film to produced perpendicular orientation for BCP film[19]. They could prepare topcoat layer to BCP by introducing initiators (monomers) and the

crosslinked layer without concerning about the surface energy of the topcoat layer. However, with this method, the surface energy of bottom layer should be considered with annealing process, unless the BCP will have parallel layer on the bottom. In this study, we applied plasma treatment to BCP film to form the crosslinked layer of BCP on the top surface. Also, the crosslinked film will have neutral surface energy to untreated BCP film which will act as a neutral brush layer to the bottom. Finally, crosslinked layer was applied to the top and bottom of the BCP film (sandwich structure) to produce fully-perpendicular micro domain. This simple and quick method to produce perpendicular orientation to any kind of BCP could be the universal solution to prepare vertical orientation for further nanolithography applications. This strategy was applied to 3 different BCP with different  $\chi$  including lamellae PS-b-PMMA (SML), cylindrical polystyrene-block-poly(dimethyl siloxane) (SDC) and lamellae polystyrene-block-poly(2-vinylpyridine) (SVL).

## 2.2. Experimental

### **Preparing BCP films and plasma induced top and bottom layer and thermal annealing for DSA**

3 different BCP including lamellae PS-*b*-PMMA ( $M_n,PS \sim 50,000$  g/mol,  $M_n,PMMA 48,000$  g/mol,  $PDI \sim 1.09$ ), cylindrical PS-*b*-PDMS ( $M_n,PS \sim 11,000$  g/mol,  $M_n,PDMS 5,000$  g/mol,  $PDI \sim 1.09$ ) and lamellae PS-*b*-P2VP ( $M_n,PS \sim 40,000$  g/mol,  $M_n,P2VP 44,000$  g/mol,  $PDI \sim 1.09$ ) were used for DSA. To prepare randomly casted BCP film, chloroform for SML, SVL, cyclohexane for SDC were chosen as solvent for spin coating and 200 nm to 300 thick film were prepared by spin coating with Laurell spin coater. Top crosslinked layer was introduced by flash plasma with varied power from 100W to 300 W and differed time from 1 s to 10 s to form the crosslinked layer with different thickness and the crosslinking density. Short time of plasma also applied to the BCP thin film with 10 nm thickness to prepare bottom plasma treated layer. DSA was done by solvent annealing and thermal annealing. Solvent annealing with acetone vapor was done in 9.3 ml jar with controlled leakage and thermal annealing was performed in the

vacuum oven at 250 °C for 5 hours, and then cooled down to room temperature.

### **Characterization of BCP nanopatterns**

For SML, topcoat and PMMA part was removed selectively by O<sub>2</sub> RIE (O<sub>2</sub>, 90 W, 10 sccm, 10 mTorr, for 25 s). For SDC, two steps of RIE was done to remove topcoat (CF<sub>4</sub> + O<sub>2</sub>, ICP power 450W, 10 sccm, 10 mTorr, for 10s) and PS part (O<sub>2</sub> plasma, 90 W, 10 sccm, 10 mTorr, for 15s). SML and SDC were Pt coated (10 mA, for 30 s) after etching process. For SVL, Au nanoparticle was infiltrated to P2VP part selectively[20]. In brief, PS-b-P2VP film was immersed in 10 mmol of H<sub>2</sub>AuCl<sub>4</sub> in 0.9 % HF solution for 10 min and rinsed with DI water several times. RIE (300 W, O<sub>2</sub>, for 30 s) was treated to remove organic part selectively. To confirm the cross section of BCPs, BCP films were put into liquid nitrogen for 5 min and cut into pieces and O<sub>2</sub> RIE was applied to the cross section.

### **Phase diagram of block copolymer**

To optimize plasma condition, argon plasma with different condition including power, time and pressure was applied to the BCP film. The argon plasma was applied with plasma machine (Reactive ion etching Plasma,

Oxford), with 15 mTorr or 150 mTorr. The time was varied from 1 s to 10 s with the plasma generation power of 100, 150, 200, 250 and 300 W. Plasma treated BCP film was located to the vacuum oven and thermally annealed at 190 °C for 5 hours. To obtain SEM images, short time of oxygen plasma (10 mTorr, 10 sccm, 10 s) was applied to the sample.

### **Angle resolved X-ray photoelectron spectroscopy(ARXPS)**

The XPS spectra were obtained using K-Alpha Surface Analysis (Thermo scientific) spectrometer equipped with a monochromatized Al K $\alpha$  source and operated at 1,486.8 eV. Survey scans were conducted at take-off angles of 0, 7, 14, 21, 28, 35, 42, 49, 56, 63 and 70° with the surface normal to the sample surface and at different penetration depths. During the XPS analysis, the sample charge was compensated by a 200 mV e-beam at a high neutralization current by means of a flood gun. The pass energy was 200 eV for survey scans and 50 eV for high-resolution scans. The pressure during the analysis was kept below  $7 \times 10^{-8}$  Torr. A 400  $\mu$ m diameter beam was used in the analysis.

## **Preparation of top- and bottom- plasma treated BCP film**

To crosslink BCP films, short time of plasma treatment was done. The plasma was generated with varied power of 100 W to 300 W power for 1 to 10 seconds, while the pressure was kept at 15 mTorr. The etching rate of air plasma and nitrogen plasma with 300 W power is 2 nm / s.

## **Solvent and thermal annealing condition of BCPs**

Solvent annealing conditions : For BP, TP, SW and neat PS-b-PDMS were exposed to controlled acetone vapour (2 ml of toluene in a 9.3 ml volume for 30 min. Thermal annealing conditions : For PS-b-PMMA, PS-b-PDMS and PS-b-P2VP was placed to vacuum oven of 250 °C. After 3 hours, specimens were taken out from the vacuum oven and cooled down to room temperature.

## **GI-SAXS**

Thin films of SML and SDC with TP, BP and SWP were prepared and thermally annealed at 250 °C for 5 hours. The GISAXS measurements were made along the 9A beamline of a Pohang Light Source. A 2D detector consisting of  $1,920 \times 1,920$  pixel<sup>2</sup> was used to collect data. The X-ray wavelength was 0.6202 Å and the sample-to-detector distance was 4 m. The

incident angle  $\alpha_i$  was varied from around  $0.08^\circ$  for the top to around  $0.14^\circ$  for the whole of the self-assembled BCP films.

### 2.3. Results and Discussion

Figure 2.1 shows the schematic image of the plasma assisted directed self-assembly method. Thin film of BCP with 200 nm thickness is prepared by spin coating. Short time of argon plasma is applied to the BCP film to crosslink the surface layer. As the crosslinked layer is consist of block copolymer, the surface energy is neutral to both polymer blocks. 3 different BCPs with different polymer composition were used to prepare perpendicular orientation. BCP thin film is affect by the interfacial energy, so the BCP with high  $\chi$ -parameter should have parallel mixed or orientation for the entropic reason. However, BCP film with crosslinked BCP layer can have perpendicular orientation as the crosslinked top coat layer acts as a neutral layer for two blocks of BCP and BCP immobilized the BCP chain. Figure 2.2a-c show the chemical structure of poly(styrene-b-dimethylsiloxane), poly(styrene-b-(methyl methacrylate)) and poly(styrene-b-2-vinylpyridine). Surface energy,  $\gamma$  of PS, PMMA, PDMS and P2VP is 40.7 mN/m, 41 mN/m, 19.8 mN/m and 53 mN/m, respectively. Cylindrical poly(styrene-b-dimethylsiloxane) ( $M_n$  : 11 kg/mol – 5 kg/mol) (SDC), lamellae poly(styrene-b-(methyl methacrylate)) ( $M_n$  : 50 kg/mol – 48 kg/mol) (SML) and lamellae poly(styrene-b-2-vinylpyridine) ( $M_n$  : 40 kg/mol – 44 kg/mol) (SVM) were used to further experiments.

To verify the effect of the plasma treatment, short time of argon plasma was

applied to SDC. SEM images of SDC with and without plasma treatment is shown in figure 2.3. SDC without plasma treatment has parallel cylinder on the top surface after thermal annealing process (figure 2.3a). However, SDC with crosslinked layer on the top, cylinder pattern with perpendicular orientation is observed (figure 2.3d-f). Hence the topcoat layer produced by plasma-induced crosslinking has higher young's modulus than neat polymers, wrinkled surfaced is formed with annealing process (figure 2.4b-d). To optimize the condition, we varied the factors such as plasma power, time and pressure, which affect to the plasma and surface chemistries.

Figure 2.5 display the SEM images of SDC with varied plasma time and pressure. In the simplified phase diagram(figure 2.6), wrinkled surface is confirmed at higher plasma power and longer treatment time, which make the stiff layer at the top which is consist of crosslinked PS and silica. When short time of plasma is applied to the film with proper plasma power, perpendicular cylinder without wrinkle is observed.

Argon plasma with different condition is also applied to SML (figure 2.7). In case of SML, PMMA part can be decomposed with UV/VUV from plasma treatment. As the penetration depth of UV/VUV is about sever hundreds of nanometers, molecular weight ratio of PS-b-PMMA can be changed under long time of plasma exposure[23]. In this reason, the area of perpendicular lamellar in SML is restricted to short and high power region (figure 2.8). According to D. B.

Graves et al,[24], the thickness of crosslinking layer prepared by plasma keeps same value about  $\sim 2$  nm regardless of treatment time. To verify the thickness of crosslinked layer, angle resolved X-ray photoelectron spectroscopy (AR-XPS) (figure 2.9) detected ester group in PMMA which confirms that decomposed PMMA by UV/VUV from plasma atmosphere. Ester group is detected by ARXPS from neat SML and SML with 1 second of plasma treatment (figure 2.9a and b). Figure 2.10 display the carbon ratio and oxygen ratio in ester group. The ester group decopomosed under UV condition, the molecular ratio of oxygen in estergroup decreases linearly with plasma time. Insterstingly, 2  $\sim$  3 nm of amorphous carbon layer (ACL) is produced with short time plasma treatment. To avoid decomposition of PMMA by UV/VUV, short and strong plasma treatment was done for SML. In the phase diagram with higher pressure of 150 mTorr, perpendicular lamellar was observed with broader area in short time plasma condition (figure 2.11). Short and strong argon plasma was applied to SML, SDC and SVL, respectively, and perpendicular nanopatterns were successfully prepared (figure 2.12).

Figure 2.13 shows the schematic images of plasma treated bottom layers (BP layers) and BCP film with sandwich plasma treatment (SWP). To form BP layer, flash plasma was applied to thin BCP film with 7 nm thickness. BP layers are insoluble to the solvent, and have a neutral surface energy to BCP films. BP layers can replace the random copolymer brushes to prepare vertical orientation from the

bottom. TP was additionally applied to BCP with BP layer, and SWP was gained. We applied BP, TP and SWP to SML and SDC BCP thin films and observed the morphology of the BCP micro domain with SEM and grazing incidence small-angle X-ray scattering (GISAXS).

The surface and cross section images of SDC and SML with BP (Fig 2.14a, d, g, and j) show partially perpendicular orientation only at the below surface which has neutral surface energy to BCP films with BP layers. Figure 2.14b, e, h and k display BCP pattern of SML and SDC with TP. On contrary to BCP with BP, BCP with TP has perpendicular orientation only at the top surface. On the other hand, BCPs with SWP having fully-perpendicular micro domain is observed with surface and cross section SEM images (Fig 2.14c, f, i and j). SEM images also support that the flash plasma on the top and bottom layer produces a layer with neutral surface energy to BCP films. Feature size of 10 nm and 30 nm for SDC and SML, respectively, was prepared with SWP within centimeter scale.

GISAXS patterns with different angle from  $0.08^\circ$  to  $0.14^\circ$  of SDC and SML with BP, TP and SWP show the overall morphology of the BCP micro domains (Fig 2.15). The critical angle,  $a_c$  for GISAXS is  $0.08^\circ$ , the obtained GISAXS patterns at incidence angle,  $a_i = a_c$ , show the morphology at the top of the BCP nano patterns. GISAXS patterns at  $a_i > a_c$ , show the overall morphology of BCP micro domain. GISAXS patterns shown in Fig 6 indicate the morphology of BCP nano patters at

the top (left) and the overall (right) film. In case of top images, the perpendicular orientation is observed TP and SWP in SDC and SML as the BCP films with TP layers which prepare the perpendicular orientation on the top of BCP layers (Fig 2.15b, c, e and f). In the overall images, on the other hand, perpendicular orientation is observed in every sample with crosslinked layers. TP and BP layer have mixed orientation through the film, the GISAXS pattern at  $a_i > a_c$  shows the pattern of both perpendicular and parallel orientation. In contrast, as SDC and SML with SWP have fully perpendicular orientation, the q-value of GISAXS patterns at  $a_i > a_c$  and  $a_i = a_c$ , are just same.

## 2.4. Conclusion

In summary, flash plasma induced crosslinked layer is demonstrated as a simple and universally adoptable way to produce perpendicular orientation of BCP micro domain. The perpendicular orientation can be produced without considering surface energy differences or without using difficult and expensive methods. The surface chemistry was identified with AR-XPS, and 2 – 3 nm of amorphous carbon layer is produced with flash plasma treatment. We also replace the random copolymer brush with crosslinked BCP. The new concept to prepare perpendicular orientation to the BCP film can be adopted to directed self assembly of BCP with high  $\chi$  parameter like PS-b-PDMS. Our results show the potential functionality of flash plasma to enable nanoscale patterning of the periodic BCP structures. As the flash plasma process is very quick and simple and also can be readily scaled up to a larger area to tens of centimeter size, the flash plasma method will enable to apply in nanomanufacturing to creat nanometer scale patterns

## 2.5. References

- [1] Z. Nie and E. Kumacheva, "Patterning surfaces with functional polymers," *Nat. Mater.*, vol. 7, no. 4, pp. 277–290, 2008.
- [2] J. K. W. Yang et al., "Complex self-assembled patterns using sparse commensurate templates with locally varying motifs," *Nat. Nanotechnol.*, vol. 5, no. 4, pp. 256–260, 2010.
- [3] C. C. Liu et al., "Fabrication of lithographically defined chemically patterned polymer brushes and mats," *Macromolecules*, vol. 44, no. 7, pp. 1876–1885, 2011.
- [4] G. Liu et al., "Epitaxial graphene nanoribbon array fabrication using BCP-assisted nanolithography," *ACS Nano*, vol. 6, no. 8, pp. 6786–6792, 2012.
- [5] Y. S. Jung, J. B. Chang, E. Verploegen, K. K. Berggren, and C. A. Ross, "A path to ultranarrow patterns using self-assembled lithography," *Nano Lett.*, vol. 10, no. 3, pp. 1000–1005, 2010.
- [6] C. J. Hawker, T. P. and P. Thomas, "Block Copolymer Lithography: Merging 'Bottom-Up' with 'Top-Down' Processes," *MRS Bull.*, vol. 30, no. December, pp. 952–966, 2005.

- [7] P. W. Majewski, M. Gopinadhan, and C. O. Osuji, "Magnetic field alignment of block copolymers and polymer nanocomposites: Scalable microstructure control in functional soft materials," *J. Polym. Sci. Part B Polym. Phys.*, vol. 50, no. 1, pp. 2–8, 2012.
- [8] D. E. Angelescu, J. H. Waller, D. H. Adamson, R. A. Register, and P. M. Chaikin, "Enhanced order of block copolymer cylinders in single-layer films using a sweeping solidification front," *Adv. Mater.*, vol. 19, no. 18, pp. 2687–2690, 2007.
- [9] H. Cho, H. Park, T. P. Russell, and S. Park, "Precise placements of metal nanoparticles from reversible block copolymer nanostructures," *J. Mater. Chem.*, vol. 20, no. 24, pp. 5047–5051, 2010.
- [10] J. G. Son, X. Bulliard, H. Kang, P. F. Nealey, and K. Char, "Surfactant-assisted orientation of thin diblock copolymer films," *Adv. Mater.*, vol. 20, no. 19, pp. 3643–3648, 2008.
- [11] S. Ji et al., "Generalization of the Use of Random Copolymers To Control the Wetting Behavior of Block Copolymer Films," *Macromolecules*, vol. 41, no. 23, pp. 9098–9103, 2008.
- [12] E. Han, K. O. Stuen, Y. H. La, P. F. Nealey, and P. Gopalan, "Effect of composition of substrate-modifying random copolymers on the orientation of

symmetric and asymmetric diblock copolymer domains,” *Macromolecules*, vol. 41, no. 23, pp. 9090–9097, 2008.

[13] A. Tavakkoli, K. W. Gotrik, A. F. Hannon, A. Alexander-Katz, C. A. Ross, and K. K. Berggren, “Templating Three-Dimensional Self-Assembled Structures in Bilayer Templating Three-Dimensional Self-Assembled Structures in Bilayer Block Copolymer Films,” vol. 1294, no. June, pp. 1294–1299, 2012.

[14] Y. S. Jung and C. A. Ross, “Orientation-controlled self-assembled nanolithography using a polystyrene - polydimethylsiloxane block copolymer,” *Nano Lett.*, vol. 7, no. 7, pp. 2046–2050, 2007.

[15] A. Laiho, P. Hiekkataipale, J. Ruokolainen, and O. Ikkala, “Directing the smectic layer orientation by shear flow in hierarchical lamellar-withinlamellar liquid crystalline diblock copolymers,” *Macromol. Chem. Phys.*, vol. 210, no. 15, pp. 1218–1223, 2009.

[16] D. Y. Ryu, K. Shin, E. Drockenmuller, C. J. Hawker, and T. P. Russel, “A Generalized Approach to the Modification of Solid Surfaces,” *Science (80-. )*, vol. 308, no. 2005, pp. 236–238, 2004.

[17] K. S. Kim et al., “Large-scale pattern growth of graphene films for stretchable transparent electrodes,” *Nature*, vol. 457, no. 7230, pp. 706–710, 2009.

- [18] R. Glass, M. Möller, and J. P. Spatz, “Block copolymer micelle nanolithography,” *Nanotechnology*, vol. 14, no. 10, pp. 1153–1160, 2003.
- [19] J. Bang, U. Jeong, D. Y. Ryu, T. P. Russell, and C. J Hawker, “Block copolymer nanolithography: Translation of molecular level control to nanoscale patterns,” *Adv. Mater.*, vol. 21, no. 47, pp. 4769–4792, 2009.
- [20] E. Kim, W. Kim, K. H. Lee, C. A. Ross, and J. G. Son, “A top coat with solvent annealing enables perpendicular orientation of sub-10 nm microdomains in Si-containing block copolymer thin films,” *Adv. Funct. Mater.*, vol. 24, no. 44, pp. 6981–6988, 2014.
- [21] E. Yoon, E. Kim, D. Kim, and J. G. Son, “Top-coat dewetting for the highly ordered lateral alignment of block copolymer microdomains in thin films,” *Adv. Funct. Mater.*, vol. 25, no. 6, pp. 913–919, 2015.
- [22] H. S. Suh et al., “Sub-10-nm patterning via directed self-assembly of block copolymer films with a vapour-phase deposited topcoat,” *Nat. Nanotechnol.*, vol. 12, no. 6, pp. 575–581, 2017.
- [23] G. S. Oehrlein, “Formation of nanometer-thick delaminated amorphous carbon layer by two-step plasma processing of methacrylate-based polymer”, *J. Vac. Sci. & Tech. B*, Vol 33, pp. 051601-051607, 2015

[24] N. Fox-Lyon, G. S. Oehrlein, N. Ning, and D. B. Graves, "Hydrogenation and surface density changes in hydrocarbon films during erosion using Ar/H<sub>2</sub> plasmas", *J. Appl. Phys.*, Vol 110, pp.104314-104319, 2011.

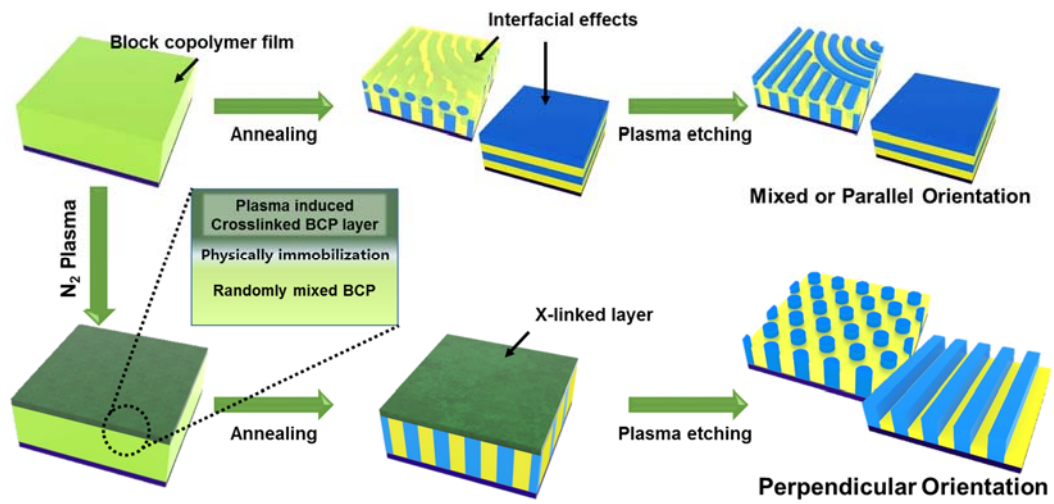


**Figure 2.1. Schematic of the plasma topcoat assisted directional self-assembly method.**

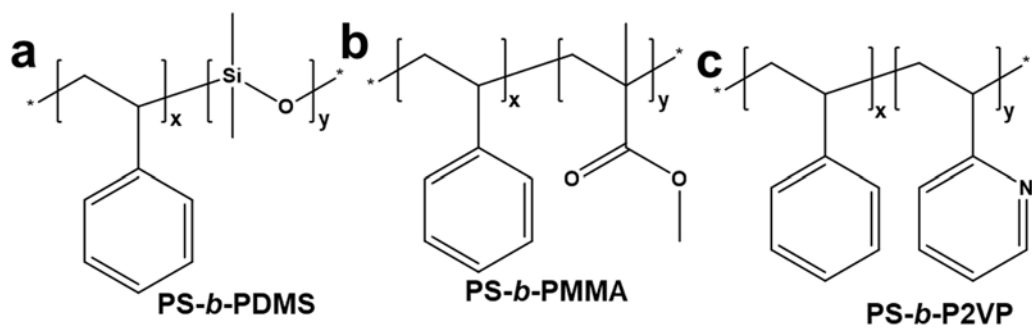


**Figure 2.2. Chemical structure of PS-*b*-PDMS, PS-*b*-PMMA and PS-*b*-P2VP.**

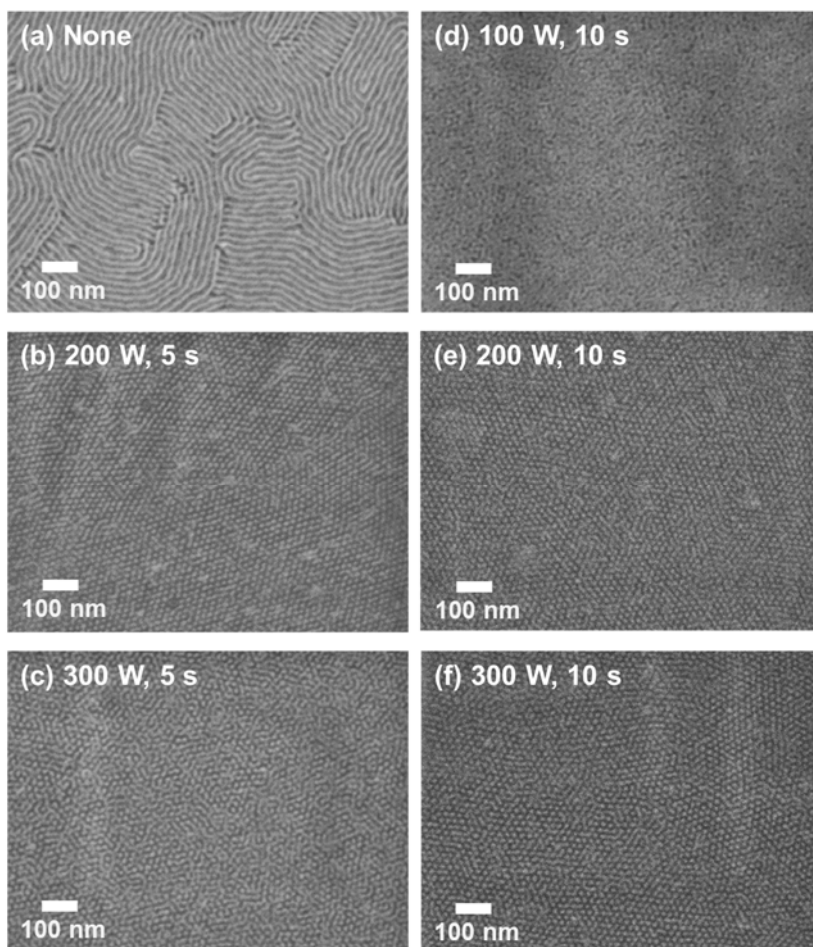


**Figure 2.3. Low magnitude SEM image of PS-b-PDMS (11k – 5k)**

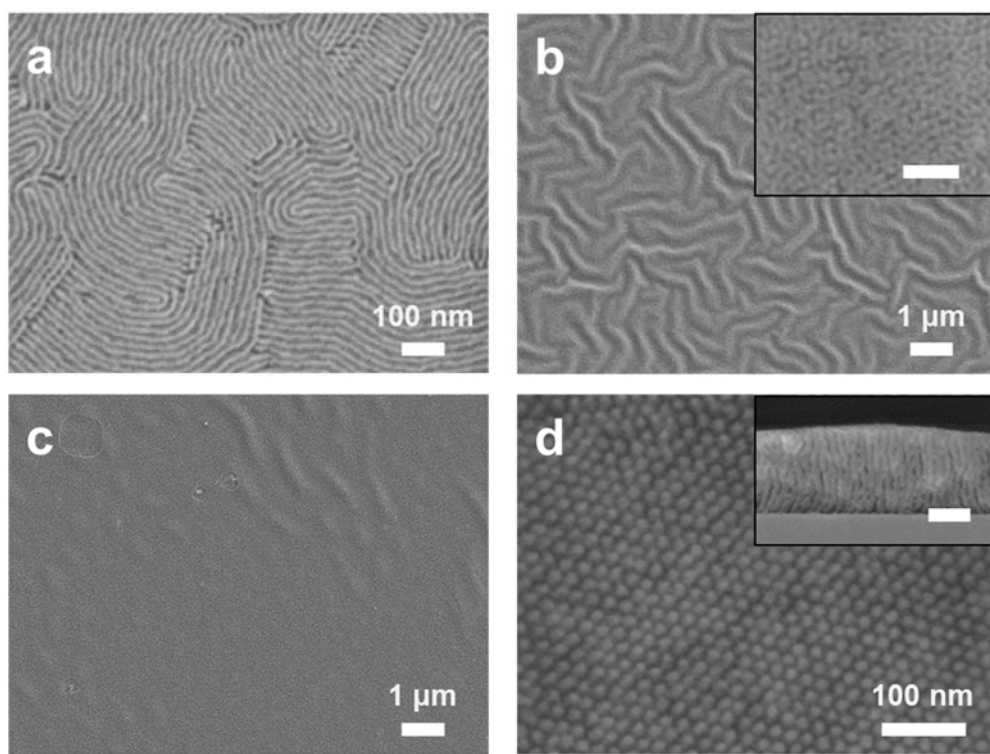


**Figure 2.4. High magnitude SEM image of PS-b-PDMS (11k – 5k).**

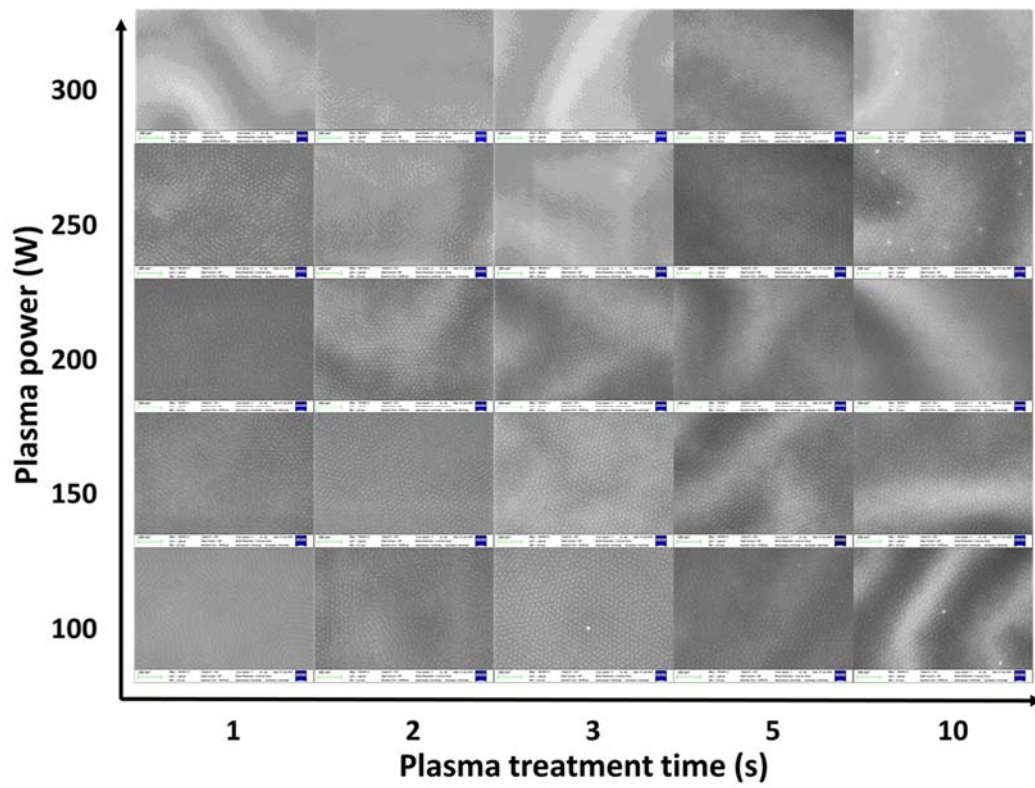


**Figure 2.5. SEM image of PS-b-PDMS nanopatterns with varied plasma power and treatment time.**

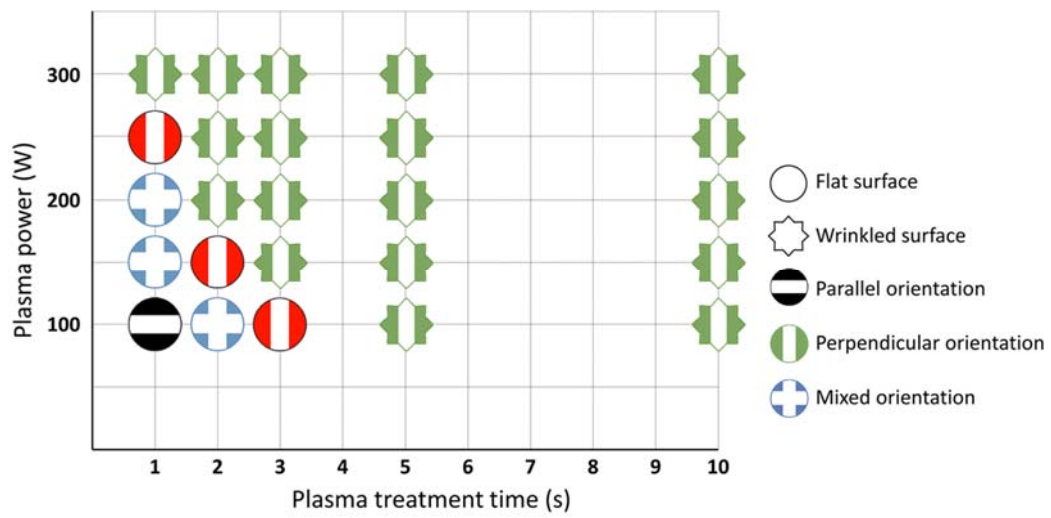


**Figure 2.6. Phase diagram of PS-b-PDMS nanopatterns with varied plasma power and treatment time at high argon flow.**

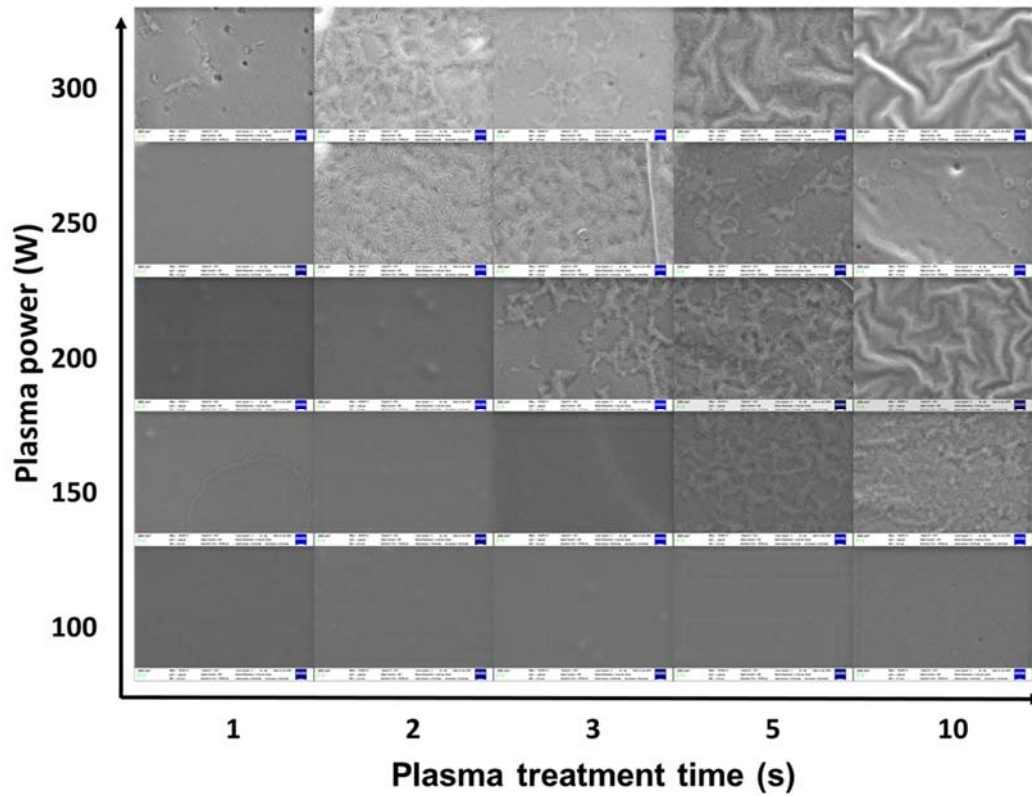


**Figure 2.7. SEM images of PS-b-PMMA nanopatterns with varied plasma power and treatment time.**

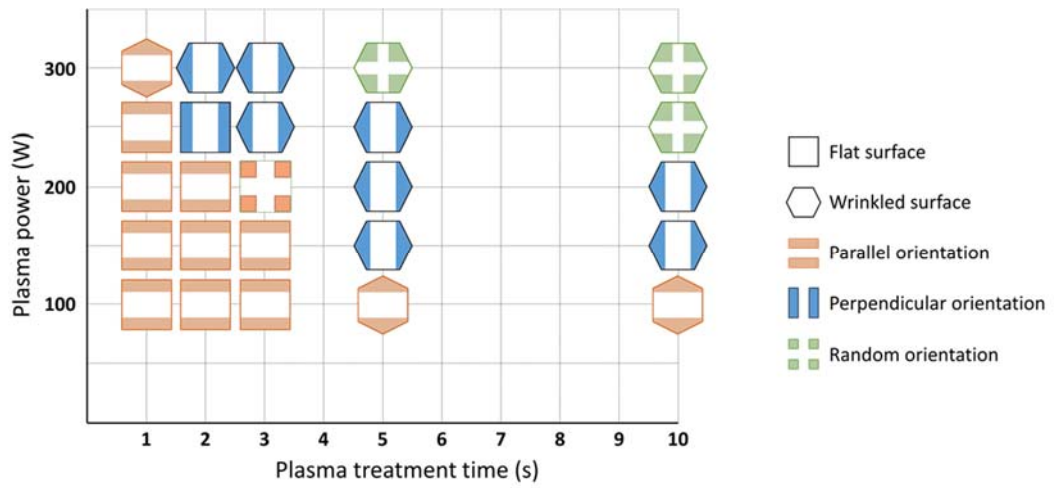


**Figure 2.8. SEM images of PS-b-PMMA nanopatterns with varied plasma power and treatment time.**

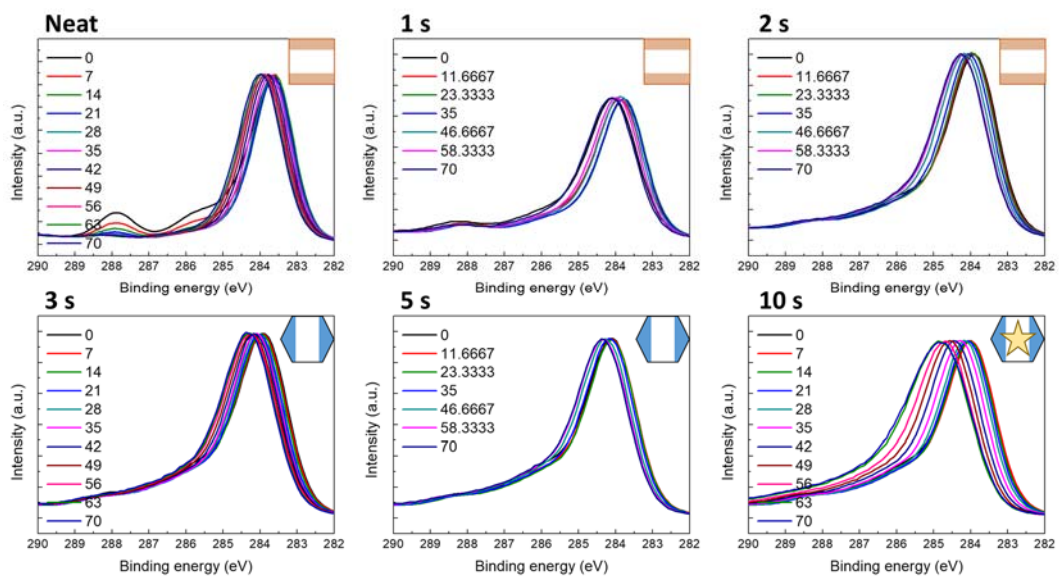


**Figure 2.9. Angle-resolved X-ray photoelectron spectroscopy of Ar plasma treated PS-b-PMMA pattern.**

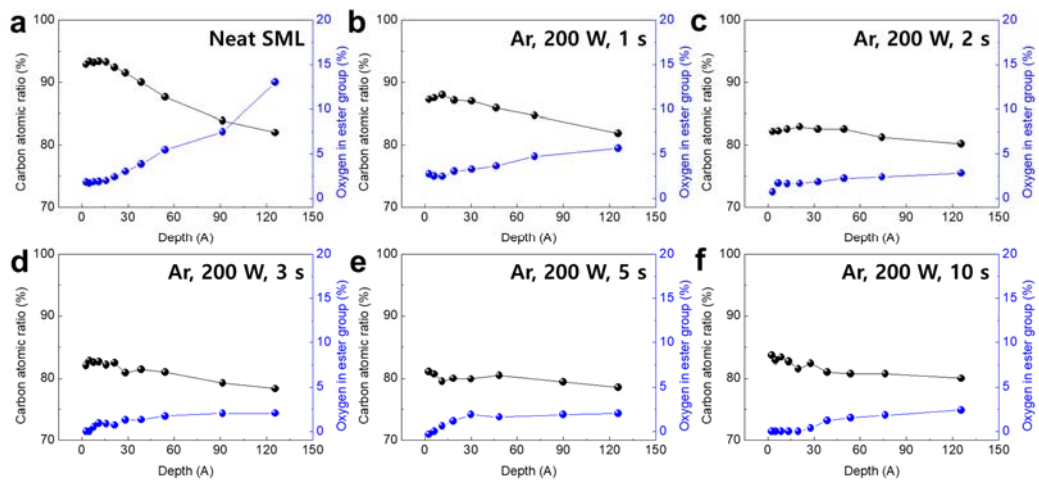


**Figure 2.10. Carbon ratio at ester group of Ar plasma treated PS-b-PMMA pattern detected by angle-resolved X-ray photoelectron spectroscopy.**

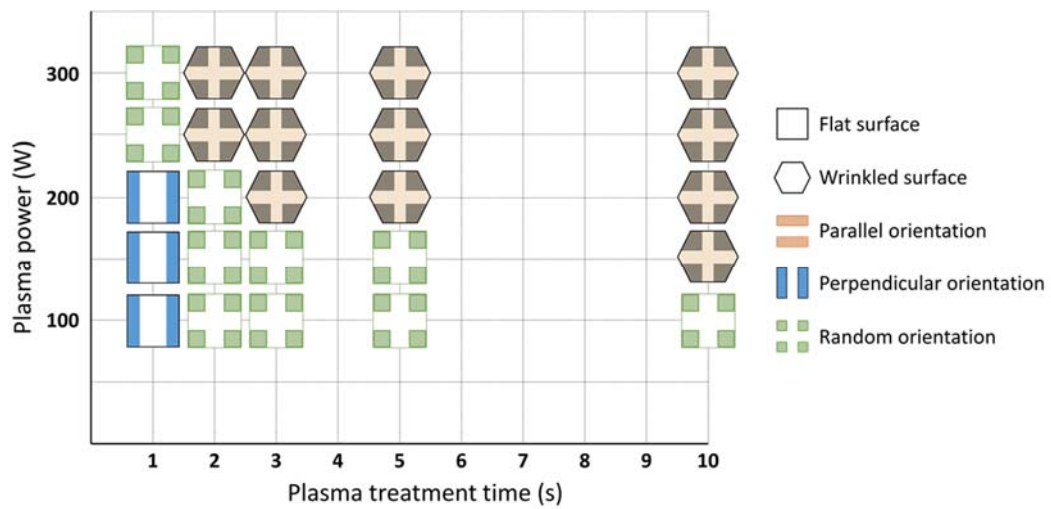


**Figure 2.11. Phase diagram of PS-b-PMMA nanopatterns with varied plasma power and treatment time.**

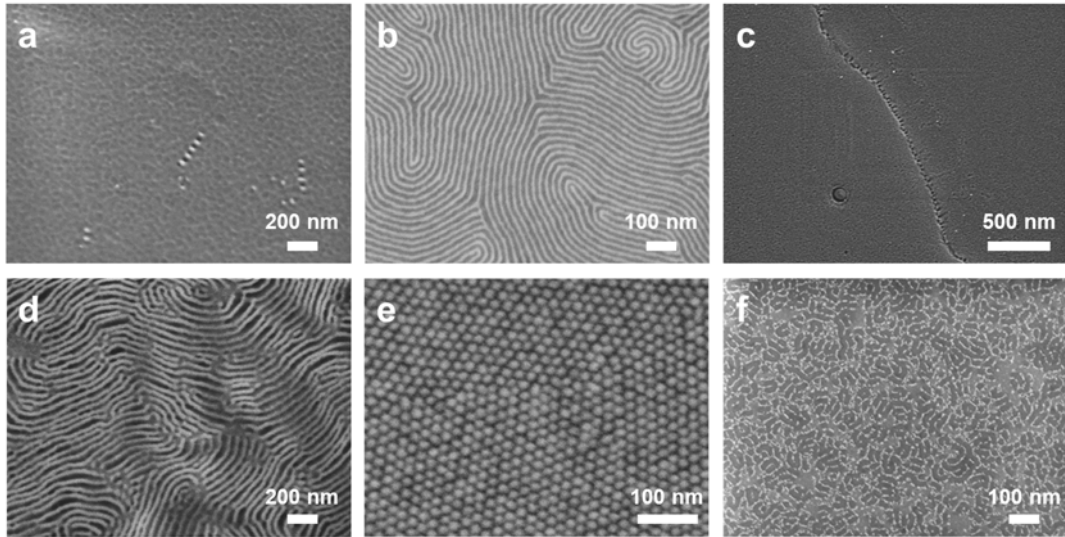


**Figure 2.12. SEM image of SML (a, d), SDC (b, e) and SVL (c, f) after thermal annealing.**

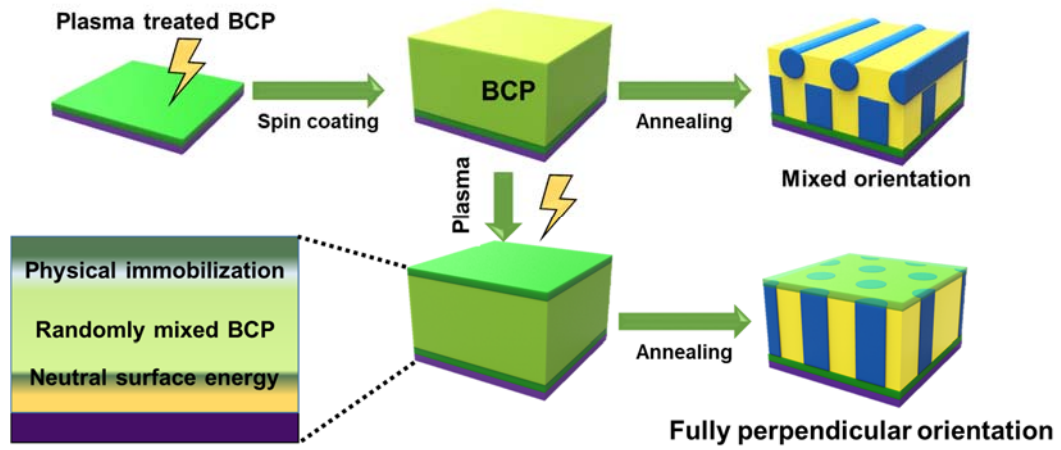


**Figure 2.13. Schematic of the top and bottom plasma treatment to prepare fully-perpendicular orientation to the BCP film.**

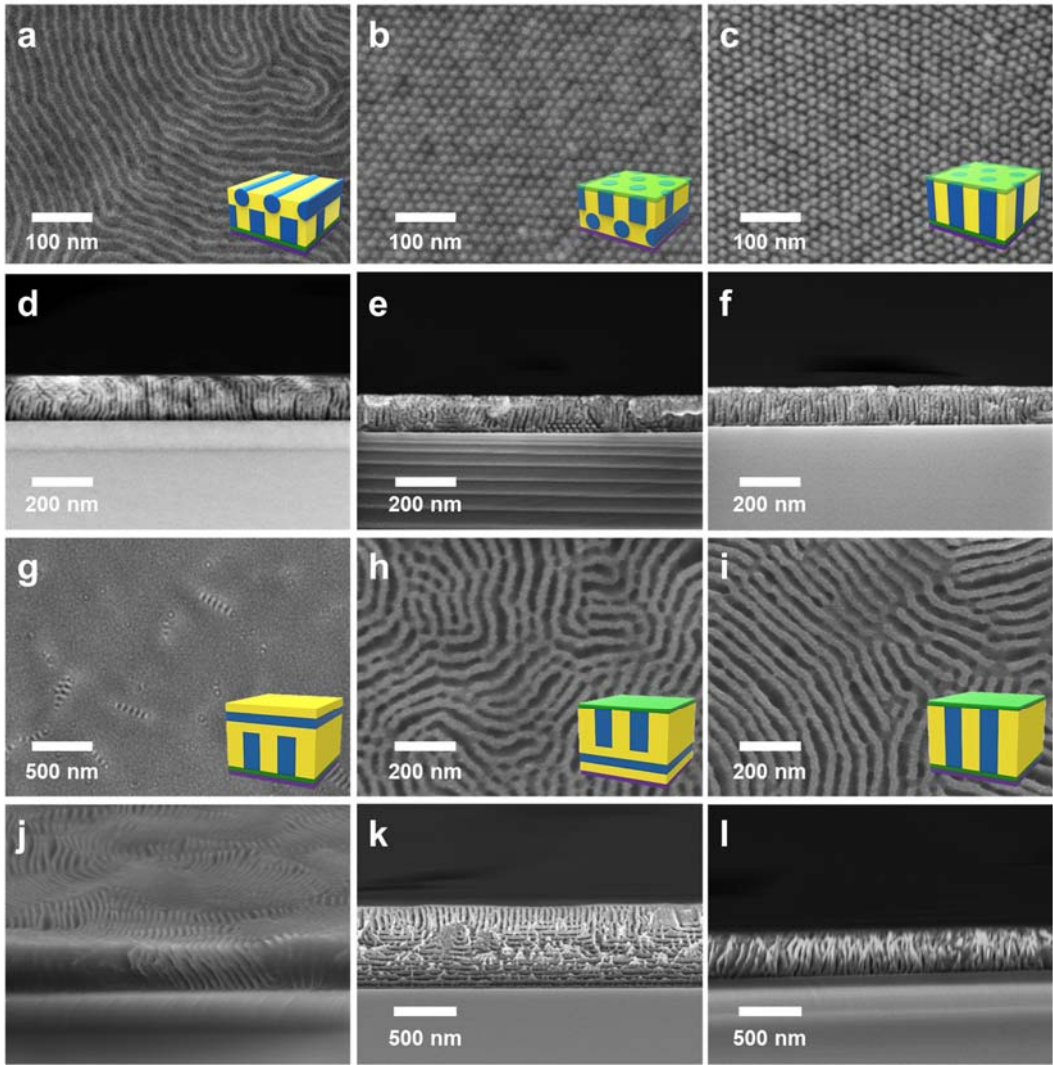


**Figure 2.14. SEM image of nano patterns with different morphology**

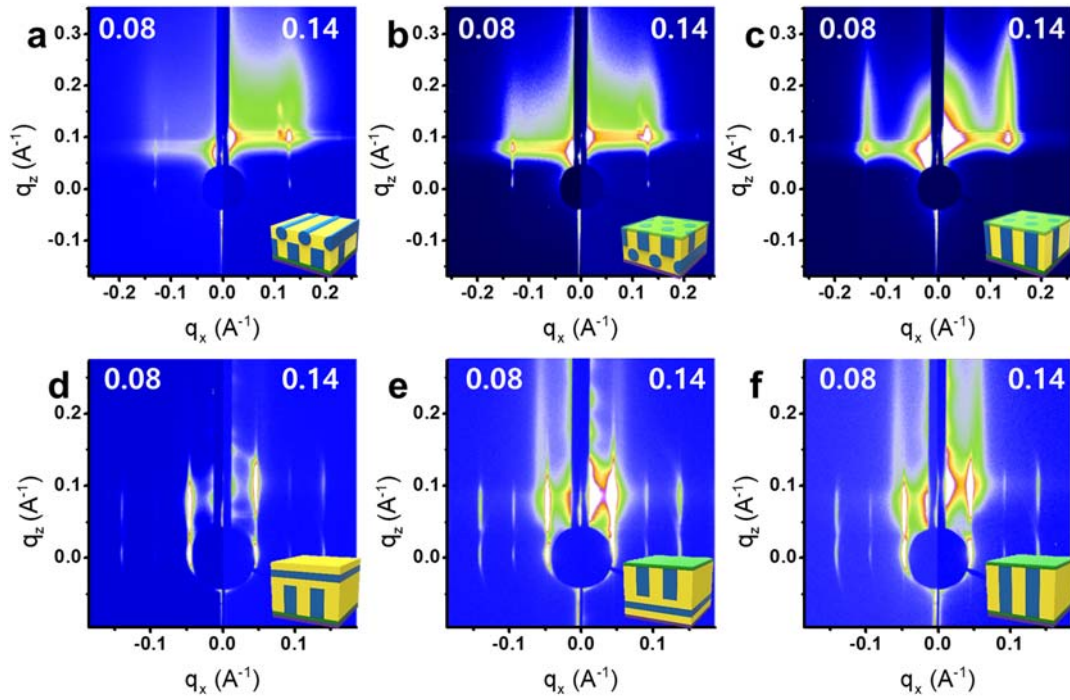
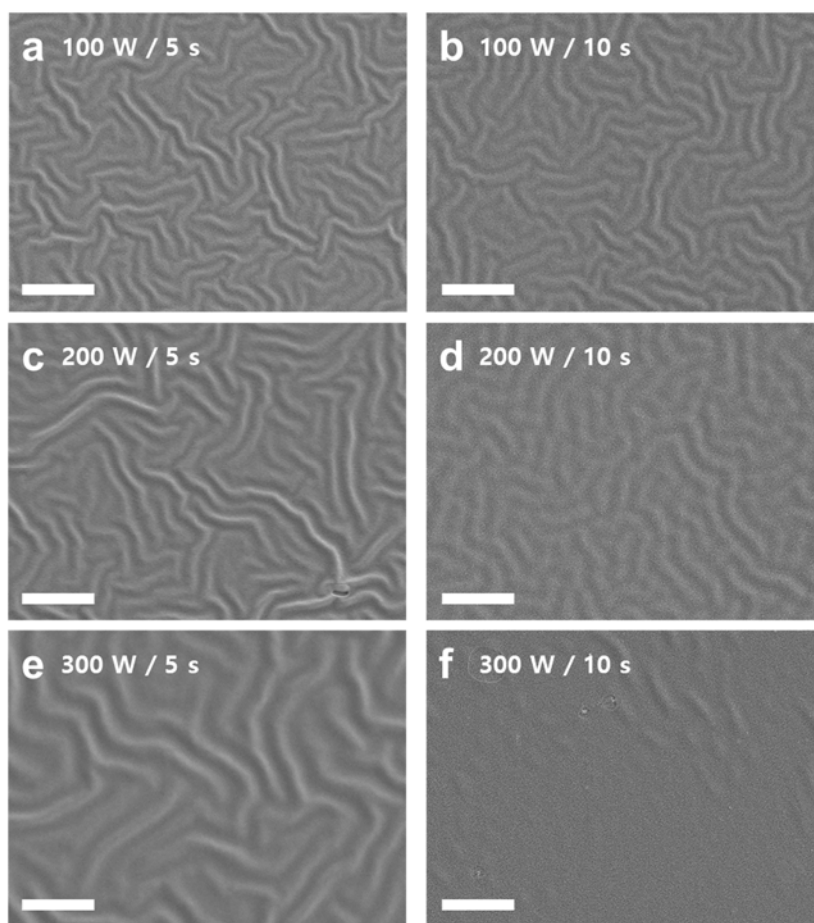
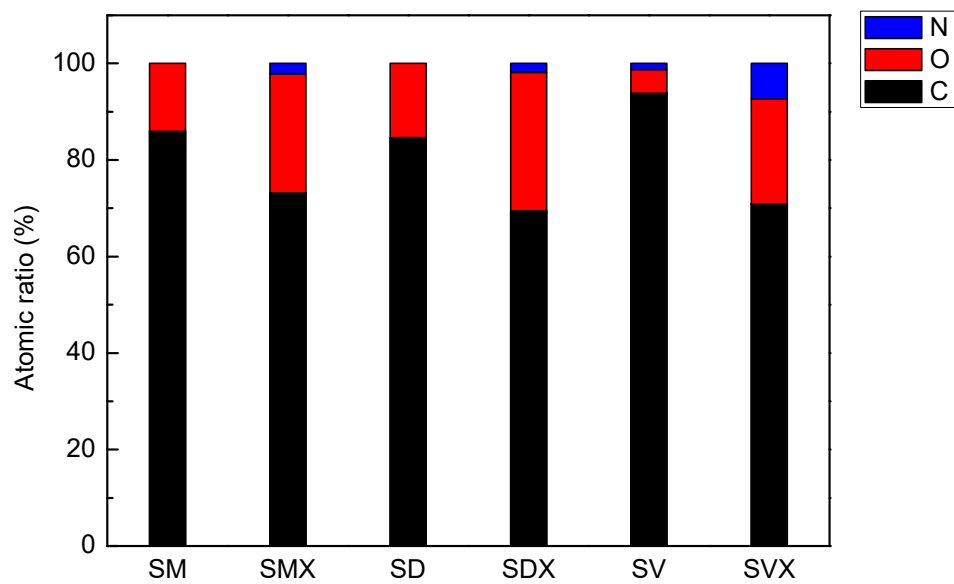


Figure 2.15. GI-SAXS image for PS-b-PDMS (a-c) and PS-b-PMMA (d-f)



**Figure 2.16. SEM image of top plasma treated PS-b-PDMS after solvent annealing.**



**Figure 2.17. XPS results for PS-b-PMMA, PS-b-PDMS and PS-b-P2VP with and without surface crosslinking layer.**

## **Chapter 3**

**Significantly reduced thermal conductivity  
and enhanced thermoelectric properties of  
single- and bi-layer graphene nanomeshes  
with sub-10 nm neck-width**

### 3.1. Introduction

Graphene, as an atomically thin 2-dimensional allotrope of carbon materials, exhibits exceptional properties, such as superior electrical and thermal conductivity, high transparency,[1] intrinsic zero bandgap and semi-metallic nature. The modification of graphene structures including hydrogenation,[2] doping[3] and patterning[4] can maintain their superior properties and simultaneously tailor or enhance specific properties for various applications. When graphene is modified into graphene nanoribbons (GNRs) or nanomeshes (GNMs), a noticeable bandgap is, however, induced due to quantum confinement and a high on/off current ratio in field effect can be achieved.[4]–[9] Bilayer graphene structure also can derive the bandgap because of an inversion symmetry breaking.[10], [11] Several graphene nanostructure fabrication methods were suggested, including unzipping carbon nanotubes,[8] nanowire etch masks[9] and e-beam lithography.[4] However, these methods are not suitable for a large-area production of the modified graphene structures. Instead, a microphase-separated block copolymer (BCP) self-assembly[12]–[14] can be more suitable for the etching mask to achieve 5 - 50 nm periodical GNMs[15]–[17] and GNR bundles[18]–[20] in large scale.

Thermal conductivity of graphene[21]–[23] also has been late but actively

investigated after the first measurement of thermal conductivity from Balandin group in 2008,[24] because of unusual thermal transport behavior from the low dimensional crystal. The thermal conductivity of single layer graphene was measured extremely high over  $3000 \text{ W}\cdot\text{m}^{-1}\cdot\text{K}^{-1}$ , [21], [22] which is far above the bulk graphite limit. It mainly originated from the lattice vibration from strong covalent  $\text{sp}^2$  bonding and long mean free path of phonon. Nanostructured defects which induce phonon-edge scattering and phonon spectra modification are known to significantly reduce and systematically control the thermal conductivity of low dimensional materials including graphene. However, thermal transport in nanostructured or defected graphene has not fully understand and not yet been proven experimentally. Only limited thermal conductivity measurements have been reported such as isotopically modified graphene by  $^{13}\text{C}$  atoms[25] and 45-nm-wide e-beam patterned GNRs on substrate.[26]

The thermoelectric effect can be described as a temperature difference creates an electric potential. The thermoelectric efficiency is quantified by a figure of merit, given by

$$ZT = \frac{S^2 \sigma}{\kappa} T$$

where  $S$ ,  $\sigma$ ,  $T$ , and  $\kappa$  are the Seebeck coefficient (thermopower), electrical conductivity, temperature, and thermal conductivity, respectively. In case of

graphene, the notably high electrical conductivity can be a superior advantage; however, thermal conductivity is severely high. Furthermore, graphene intrinsically has a relatively low thermopower value less than  $100 \mu\text{V}\cdot\text{K}^{-1}$  due to the zero-bandgap nature.[27] Therefore, for a better thermoelectric efficiency, it is required to reduce the thermal conductivity and increase thermopower while maintaining the intrinsic high electrical conductivity.[21]–[23] Many computational researchers have suggested various graphene nanostructures in the range of 10 nm scale for significant enhancement of thermoelectric efficiency. This can be achieved in zigzag and armchair GNRs,[28]–[30] GNMs[31]–[33] and graphene superlattice[34], [35] with controlled number of graphene layers[36], [37] by tuning band structures for superior thermopower and reducing thermal conductivity through the dominant phonon-edge scattering. However, no experimental results have been reported for nanostructured graphene. There was only a report on the enhancement of thermopower of a few-layer graphene by an oxygen plasma treatment.[38]

In this paper, we fabricated centimeter-scale single- and bilayer graphene nanomeshes (SGNMs and BGNMs) with various neck width from 8 nm to 21 nm using BCP self-assembly on CVD-grown graphene. The GNR is more ideal structure for investigating the quantum confinement effect, but the GNM structure was chosen because the nanomesh is quasi-isotropically periodic nano-patterns in

a large scale for engaging the quantum confinement and providing directional freedom during the macroscopic measurement and macroscopically interconnected network for higher mechanical stability at suspended geometry. By introducing sub-10 nm patterns into graphene, the quantum confinement can simultaneously and effectively control the electronic and phononic band structures and frequency of phonon scattering, whereas sub-100 nm patterns in graphene only reduce the mean free path of the phonon and rarely affect the band structures and thermopower value. We also investigated the effect of cross-plane coupling in the BGNMs on the thermal and thermoelectric properties. To measure the thermal conductivity of the suspended GNM, we transferred the nanomeshes to micro-sized holey membranes and used the optothermal Raman technique.[24], [25], [39]–[42] We also prepared 2-cm-long GNMs on an insulating substrate to measure the thermopower value from the conventional Seebeck coefficient measuring system, carrier concentration and mobility from Hall effect measurements and bandgap from FET characteristic measurements.

## 3.2. Experimental

### Materials

First, graphene monolayer sheets were grown using a low-pressure CVD process on Cu foil at 1,000 °C with controlled H<sub>2</sub> and CH<sub>4</sub> gas flows. The as-synthesized graphene with a supporting poly(methyl methacrylate) (PMMA) layer was transferred to a SiO<sub>2</sub>-deposited Si wafer and rinsed with acetone to remove residual polymers; then, an optional second graphene sheet was repeatedly transferred onto the first graphene/SiO<sub>2</sub>/Si substrate for twisted bilayer graphene. Figure S1 in the Electronic Supplementary Information shows the morphology and Raman spectra of the double-transferred graphene sheets on the SiO<sub>2</sub>/Si wafer, which corresponded well with the properties of BLG.[43]–[45] On the transferred SLGs or BLGs, 66.5 kg·mol<sup>-1</sup> of PS-*b*-P2VP (76.7 vol% of PS) was spin-coated and solvent-annealed with slightly PS selective toluene vapor in 1 h to form hexagonally packed spherical nanostructures.[46] To develop topographical hole patterns of BCPs, P2VP spherical domains were selectively swelled by immersing in ethanol at 60 °C for 30 min;[47] 42 nm period hole patterns can be seen in the SEM image. We then etched the exposed nanohole area of graphene using an O<sub>2</sub> RIE process (90 W, 10 mTorr, 10 sccm). Etching times from 8 s to 23 s were

sufficient to punch holes to the basal plain of SLG/BLG. Rinsing in toluene and thermal treatment at 400 °C for 1 h in an Ar atmosphere was performed to remove the residuals from the samples. For transmission electron microscopy (TEM) analysis and thermal conductivity measurement using the optothermal Raman technique we additionally transferred the fabricated GNMs or graphenes to Au-coated silicon nitride (SiN<sub>x</sub>) membranes with 2.5- $\mu$ m-diameter holes using a PMMA support layer. Other measurements including the Seebeck coefficients and FETs were carried out with supported geometry on a SiO<sub>2</sub>/Si substrate.

### **Synthesis of graphene from chemical vapor deposition**

In this research, graphene was grown by low-pressure CVD process on thin Cu foil (25  $\mu$ m, Alfa Aesar). The Cu foil was cleaned by 5% nitric acid for 2 min and rinsed with water, methanol and IPA. And then, the Cu foil was put into the furnace and annealed at 1000 °C for 30 min with 100 sccm of H<sub>2</sub> gas flow. We synthesized monolayer of graphene for 10 min with 100 sccm of CH<sub>4</sub> and 40 sccm of H<sub>2</sub> at same temperature, and the quenching process was followed. To transfer the graphene for the device fabrication, poly(methyl methacrylate) (PMMA, Sigma Aldrich, Mw ~ 350,000) was spin coated on the graphene/Cu foil. Cu was etched by immersing in a 114 g/L of ammonium persulfate ((NH<sub>4</sub>)<sub>2</sub>S<sub>2</sub>O<sub>8</sub>) aqueous solution

for 1 hour and PMMA/graphene film floating on the Cu etchant was washed by D.I. water several times. PMMA/graphene film was transferred by scooping up to the device or substrate and dried at 60 °C. To fabricate fine quality graphene, solvent annealing process was done. PMMA coated graphene on the substrate was put into a jar of 9.7 ml with acetone and sealed with controlled vent and the jar was put in the hood for an hour to spread the film to the substrate perfectly. After the solvent annealing process, PMMA was removed by dipping into acetone for 30 min and rinsed using methanol and IPA. To prevent contamination, graphene on substrate was kept in the vacuum.

### **BCP self-assembly on graphene and fabrication of the GNM**

The single and bilayer graphene were treated with a hydroxyl-terminated PMMA homopolymer ( $M_n \sim 4,000$ , PDI  $\sim 1.15$ , Polymer Source) by spin-coating from 1 wt% chloroform solution, annealing at 170 °C for 3 h in vacuum and rinsing with chloroform for avoiding dewetting phenomena of BCP film. PS-*b*-P2VP ( $M_{n,PS} \sim 50,000$ ,  $M_{n,P2VP} \sim 16,500$ , PDI  $\sim 1.09$ ) were purchased from Polymer Source, Inc. A 1 wt% solution of PS-*b*-P2VP in toluene was spin-coated to form 30-nm-thick films on the graphene. The BCP films were exposed to controlled toluene vapor (0.6 mL of toluene in a 9.3 mL volume glass chamber with a controlled leak) for 1

h and were immersed in ethanol for 30 min at 60 °C for the nanostructure reconstruction. The annealed BCP/graphene films were treated with O<sub>2</sub> RIE (90 W, 10 sccm, 10 mTorr, 10 s) to etch the graphene following solvent annealing. To remove the residual polymer, the nanomesh was thermally treated at 400 °C for 1 h in an Ar atmosphere.

### **GNM Characterization**

The morphology of the graphene and BCP films was examined by field emission scanning electron microscopy (FE-SEM, JEOL JSM-6701F) at 10 kV, transmission electron microscopy (TEM, FEI Tecnai G2 F20) at 80 keV, atomic force microscopy (AFM, Asylum Research MFP-3D), and optical microscopy (OM, Nikon Optiphot). Raman spectroscopy (Renishaw inVia) with a 633 nm laser and 100× objective lens was used to analyze the graphene structures. For the sample preparation for TEM and thermal conductivity measurements using the optothermal Raman technique, we transferred the fabricated GNMs to Au-coated silicon nitride membranes with 2.5 μm-diameter holes (Ted Pella, PELCO<sup>®</sup> holey silicon nitride support film) using a PMMA support layer. The thermopower and electrical conductivity of the GNM or unpatterned graphene films on 2 cm × 2 cm SiO<sub>2</sub>/Si substrates were measured by a TEP-600 (Seepel Instrument, Korea) thermoelectric

measurement instrument in the temperature range from 300 to 520 K under an Ar atmosphere. When we applied temperature differences (0.5, 1.5, and 2.5 °C in one direction and -0.5, -1.5, and -2.5 °C in the opposite direction) to the two ends of the sample, the probes measured the potential difference and yielded the Seebeck coefficients. The linear correlation coefficients of the linear fit were greater than 0.99. Regarding the confirmation of the instrument reliability, the  $\sigma$  and  $S$  of Ni (99.99%) were  $1.4 \times 10^7 \text{ S} \cdot \text{m}^{-1}$  and  $-21.5 \text{ } \mu\text{V} \cdot \text{K}^{-1}$ , respectively. The carrier concentration and mobility were obtained by the Hall effect measurement system (Ecopia, HMS-5500) at a 0.55 T magnetic field and 100 nA electric current with previously prepared thermoelectric samples at room temperature. We also prepared at least 5 GNM samples for each thermopower and electrical conductivities measurement and expressed standard deviation by error bars.

## **Thermal conductivity measurements**

We used non-contact Raman optothermal method[21], [25], [39], [40] for the measuring thermal conductivity of graphene and graphene nanomeshes (GNMs). A 633 nm beam of He-Ne laser was focused on the center of the suspended graphene or GNM samples using a 100 $\times$  objective lens with a numerical aperture of 0.85.

Figure 3.4c shows a Raman mapping image of successfully transferred graphene & GNMs to Au-coated SiN<sub>x</sub> holey membrane with 2.5 μm holes.

The radius of the laser spot was calculated by knife-edge method [39]. In brief, 200 nm thick Au film was deposited onto the Si wafer and cleaved using a diamond knife for the freshly cleaved Si edge. We then executed micro-Raman scan across an edge of the Au/Si substrate. The integrated intensity (I) of the Si peak at ~520 cm<sup>-1</sup> can be proportional to total laser incidence to the Si wafer. Figure 3.12 shows the Raman intensity and its differential value as a function of the distance (x) of the laser beam. The slope  $dI/dx$  can be fitted to a Gaussian function  $\exp(-x^2/r_0^2)$  and the beam size,  $r_0$  was obtained. For the 100× objective lens, the  $r_0 = 0.27 \mu\text{m}$ .

The temperature rising from the Raman laser heating can be determined from the linear shift of Raman 2D peak according to the temperature. We measured the Raman 2D peak with weak laser power (~0.05 mW) meanwhile the sample was directly heated by hot plate to obtain a linear calibration between the temperatures versus the Raman 2D peak, as shown in Figure 5a. The slopes for the temperature versus the Raman 2D peak were -6.4, -3.4, -5.0 and  $-2.8 \times 10^{-2} \text{ cm}^{-1} \cdot \text{K}^{-1}$  for SLG, tBLG, SGNM, BGNM, respectively. The absorbed laser power of pristine graphene Q could be obtained from the difference between the power measured by power meter at an empty hole and that of a graphene-covered hole. The optical absorption of single layer graphene (SLG) and bilayer graphene (BLG) were measured  $2.9 \pm$

1.0 % and  $5.7 \pm 1.6$  % at 633 nm wavelength, respectively. The absorbed laser power of GNMs, which were also measured by power meter, have linear correlation with graphene coverage  $(1-\rho)$  and can be expressed as  $Q(1-\rho)$ . In order to calculate the thermal conductivity, we used the heat diffusion equation in cylindrical coordinates from the previous research [25]. The thermal conductivity  $K$  of the graphene or GNMs can be described as

$$K = \frac{\alpha \times \ln\left(\frac{R}{r_0}\right)}{2\pi t[(T_m - T_0)/(Q - Q_{air})(1 - \rho)]}$$

where  $R$  is the radius of the holes of  $1.25 \mu\text{m}$ ;  $r_0$  is the radius of the laser beam of  $0.27 \mu\text{m}$ ;  $t$  is the thickness of the graphenes or GNMs;  $\alpha$  is 0.98 for the  $100\times$  objective lens;  $T_m$  is the measured temperature;  $T_0$  is the room temperature;  $\rho$  is the areal porosity of GNMs which was measured by TEM and averaged in figure 3.2;  $Q_{air}$  is the heat loss in air as

$$Q_{air} = \int_{r_0}^R 2\pi g(T(r) - T_0)rdr + \pi r_0^2 g(T_m - T_0)$$

and temperature profile  $T(r)$  can be simply adopted from the literature about two-laser Raman thermometry with actual measurement of temperature distribution from the laser [41],

$$T(r) - T_0 = -\frac{\ln\left(\frac{r}{R}\right)}{\ln\left(\frac{R}{r_0}\right)}(T_m - T_0)$$

In this system, the heat transfer coefficient  $g$  was set as  $2.9 \times 10^4 \text{ W}\cdot\text{m}^{-2}\cdot\text{K}^{-1}$  [25]. For the standard deviation of our measurement, we measured the 2D peak shift of GNMs repeatedly, and the standard deviation is displayed as error bars for figure 3.5a and 3.5b, and based on this error, the temperature deviation (x-axis) of figure 3.5c and 3.5d was determined. To calculate the thermal conductivities of GNMs, temperature deviation, laser absorbance to GNMs and heat transfer to air were considered and marked as y-axis error bars.

## **Fabrication Process of GNM Field Effect Transistors**

We firstly executed E-beam patterning on PMMA resist coated GNMs and etched using RIE with  $\text{O}_2$  (50 W, 90 sccm, 100 mTorr, 3 min) at the area to be deposited the source and drain electrodes to avoid contact with metal electrode and residual GNMs. Cross-shaped isolated mesh area was reserved for measuring electrical properties. The source and drain electrodes were deposited using second E-beam lithography again followed by electron-beam evaporation of Ti/Au. The electrical properties of SGNM12 and BGNM8 devices were characterized in vacuum in the temperature ranges of 1.5–300 K with an Agilent B1500 semiconductor parameter analyzer.

Source drain current ( $I_{\text{DS}}$ ) was measured with an application of a constant source-drain bias voltage ( $V_{\text{DS}}$ ) of 1 mV as a function of back-gate voltage ( $V_{\text{G}}$ ).

When the samples are inserted in a cryostat for the temperature dependent measurement, the samples were annealed by the application of high current up to  $\sim 300 \mu\text{A}$  to avoid the effect of dopants attached in ambient condition such as water and oxygen. Most of the samples showed the p-type behavior before the annealing but they change to the slightly n-type doped or neutral after the annealing. At 1.5 K, the  $I_{\text{DS}}$  at charge neutrality is fully suppressed which confirms that the dominating conduction is thermionic emission at this gate voltage.

## **Electronic structure calculations**

We performed the first-principles calculations within the framework of density functional theory (DFT) as implemented in the plane-wave basis VASP code [44]. For treatment of the exchange-correlation energy, the projected augmented wave (PAW) pseudopotentials [44] with the PW91 [45] generalized gradient approximation (GGA) of Perdew and Wang is used. The GNM samples considered in electronic structure calculations have the hexagonal unit cell with the size  $\sim 22 \text{ \AA}$  (see Figure S4a), where the edges of holes are passivated with H atoms. We focus on the simple hexagonal holes with pure armchair-type edges. The interlayer distance between the two GNM (AB stacking) is fixed with graphite interlayer spacing ( $3.35 \text{ \AA}$ ). Geometry optimizations are performed using the conjugate gradient scheme until force components on every atom are less than  $0.01 \text{ eV \AA}^{-1}$ .

The fully relaxed structures are used to compute the electronic band structure. A plane-wave cutoff energy of 600 eV and an energy convergence criterion of  $10^{-7}$  eV for self-consistent cycle are adopted. For ionic relaxation a  $5 \times 5 \times 1$  Monkhorst-Pack  $\mathbf{k}$ -mesh are used for the unit cell of GNM samples. For transport coefficients calculations, a much denser  $\mathbf{k}$ -mesh of  $23 \times 23 \times 1$  is used. Both SGNM and BGNM samples with coverage 0.45 and 0.7 are considered. Figure 3.11b and c shows our computed band structure of SGNM and BGNM sample with coverage 0.7.

## Transport coefficient calculations

For transport coefficient calculations, we employ semi-classical Boltzmann theory within the constant relaxation time approximation, as implemented in the BOLTZTRAP code.[46] The electrical conductivity ( $\sigma$ ) and Seebeck coefficient (S) are calculated by defining the following function

$$L^{(\alpha)} = e^2 \tau \sum_n \int \frac{dk}{4\pi^3} v_n(k) v_n(k) (\varepsilon_n(k) - \mu)^\alpha \left(-\frac{\partial f}{\partial \varepsilon}\right)_{\varepsilon=\varepsilon_n(k)}$$

and obtained from  $\sigma = L^{(\alpha)}$ , and  $S = 1/eT(L^{(0)})^{-1}L^{-1}$ , where  $e$  is the electronic charge,  $\tau$  the relaxation time,  $v_n(k) = \left(\frac{1}{\hbar}\right) \nabla_k \varepsilon_n(k)$  the group velocity in the  $n$ th band at  $\mathbf{k}$ ,  $\varepsilon_n(\mathbf{k})$  the energy eigenvalues obtained from DFT,  $\mu$  the chemical

potential, and  $f$  the Fermi-Dirac function at a given temperature  $T$ . Simulations are carried out at temperatures ranging from 300 – 600 K.

We considered the scattering due to electron-phonon interactions to compute transport coefficients by calculating energy dependent relaxation time ( $\tau(\varepsilon)$ ), which is mainly determined by the acoustic deformation potential scattering, rather than using constant  $\tau$  value. Here, we only considered the acoustic phonon scattering, and the relaxation time can be expressed as

$$\frac{1}{\tau(\varepsilon_k)} = \frac{2\pi k_B T D_{ac}^2}{A \rho_m v_{ph}^2} \sum_{k'} \delta(\varepsilon_k - \varepsilon_{k'}),$$

where  $k_B$  is the Boltzmann constant,  $D_{ac}$  is the deformation-potential coupling constant (16 eV),  $\rho_m$  the graphene mass density,  $v_{ph}$  the graphene sound velocity, and  $A$  the area of the sample. The term  $\sum_{k'} \delta(\varepsilon_k - \varepsilon_{k'}) / A$  yields the density of states of graphene nanomesh samples. Our calculated Seebeck coefficients ( $S$ ) of pristine graphene as a function of carrier concentration are in good agreement with measured Seebeck coefficients. And also, since the electronic band structure of graphene is invariant in the studied temperature region (300 K to 600 K), we used rigid band approximation in transport coefficient calculations.

## Thermal conductivity calculations

The lattice thermal conductivities for graphene nanomesh (GNM) systems are calculated with a classical molecular dynamics (MD) simulations employed within the LAMMPS package [47]. The thermal conductivity is computed from the fluctuations of the heat current, using the Einstein relation [34], [48], [49].

$$K_{\alpha} = \frac{1}{k_B V T^2} \lim_{t \rightarrow \infty} \frac{1}{2t} \langle [R_{\alpha}(t) - R_{\alpha}(0)]^2 \rangle$$

where  $k_B$  is the Boltzmann constant,  $V$  the system volume and  $T$  the temperature, respectively.  $\langle \dots \rangle$  is the mean square displacement of the integrated microscopic heat flux along the  $\alpha$  direction, given by  $R_{\alpha} = \sum_i \varepsilon_{i\alpha} r_i$ , where  $\varepsilon_i$  is the energy of atom  $i$  at position  $r_i$ . The volume is calculated as the product of the unit cell planar area times 3.35 Å and 6.7 Å for single layer and bilayer samples, respectively. To describe the covalent bonding interactions between C atoms, we used the Tersoff potential [50], [51], and the van der Waals interaction between graphene layers is described by the Lennard-Jones (LJ) potential [52]. All simulations are carried out at 300 K with a time step of 0.2 fs. To obtain converged results, 10 separate simulations are averaged for each system, each with different initial conditions. In each run, after a 100 ps equilibration period, the microscopic heat flux is recorded for  $2 \times 10^7$  MD steps (4 ns) in order to obtain a converged thermal conductivity value. The GNM systems studied in thermal conductivity calculations have the rectangular

unit cell with the size of 50 Å, and circular holes with disordered edge are arranged in two-dimensional square lattice. We consider both SGNM and BGNM samples with different graphene coverages ranging from 0.4 to 1.

### 3.3. Results and Discussion

Figure 3.1 schematically illustrates the GNM fabrication based on the BCP self-assembly and reactive ion etching (RIE) process on CVD-grown graphene sheets. First, graphene monolayer sheets were grown using a low-pressure CVD process on Cu foil at 1,000 °C with controlled H<sub>2</sub> and CH<sub>4</sub> gas flows. The as-synthesized graphene with a supporting poly(methyl methacrylate) (PMMA) layer was transferred to a SiO<sub>2</sub>-deposited Si wafer and rinsed with acetone to remove residual polymers; then, an optional second graphene sheet was repeatedly transferred onto the first graphene/SiO<sub>2</sub>/Si substrate for twisted bilayer graphene. Figure S1 in the Electronic Supplementary Information shows the morphology and Raman spectra of the double-transferred graphene sheets on the SiO<sub>2</sub>/Si wafer, which corresponded well with the properties of BLG.[53]–[55] On the transferred SLGs or BLGs, 66.5 kg·mol<sup>-1</sup> of PS-*b*-P2VP (76.7 vol% of PS) was spin-coated and solvent-annealed with slightly PS selective toluene vapor in 1 h to form hexagonally packed spherical nanostructures.[56] To develop topographical hole patterns of BCPs, P2VP spherical domains were selectively swelled by immersing in ethanol at 60 °C for 30 min;[57] 42 nm period hole patterns can be seen in the SEM image of Figure 3.2a. We then etched the exposed nanohole area of graphene using an O<sub>2</sub> RIE process (90 W, 10 mTorr, 10 sccm). Etching times from 8 s to 23

s were sufficient to punch holes to the basal plain of SLG/BLG. Rinsing in toluene and thermal treatment at 400 °C for 1 h in an Ar atmosphere was performed to remove the residuals from the samples. For transmission electron microscopy (TEM) analysis and thermal conductivity measurement using the optothermal Raman technique (figure 3.1b) we additionally transferred the fabricated GNMs or graphenes to Au-coated silicon nitride (SiN<sub>x</sub>) membranes with 2.5- $\mu$ m-diameter holes using a PMMA support layer. Other measurements including the Seebeck coefficients and FETs were carried out with supported geometry on a SiO<sub>2</sub>/Si substrate (figure 3.1c).

In the AFM image of SGNM in figure 2b, hexagonally holed GNM structures were fully developed in a large area of the films without impurities, and the height difference between the mesh and holes was approximately 1 nm, which is comparable to monolayer graphene in the AFM experiments.[38] We controlled the neck width of graphene nanomesh patterns by varying the etching time from 8 to 23 s. Transmission electron microscopy (TEM) studies were then carried out for precise characterization of the GNM nanostructures. Figures 3.2c-g show the TEM images of SGNMs (c, d) and BGNMs (e-g) with variable neck widths. They clearly exhibit hexagonally arranged and circular-shaped nanoholes. The SGNM samples with an etching time of 13 and 18 s exhibit the averaged neck width of 16.3 nm and 12.2 nm, respectively. The BGNMs with 13 s, 18 s and 23 s of etching time show

their average neck width of 21.1 nm, 14.4 nm and 8.2 nm, respectively. For the simplicity we hereafter denote the samples as SGNM16, SGNM12, BGNM21, BGNM14 and BGNM8 as their neck widths. The statistical analysis of the neck width and porosity of SGNMs and BGNMs are conducted and the results are shown in figure 3.3 and distribution diagrams are shown in figure 3.9. The standard deviations of variously etched neck widths, which is exhibited by error bars, are relatively narrow (approximately 2 nm) and can represent the ensemble average thermal and thermoelectric properties of graphene nanomeshes within endurable irregularity. The neck widths of the BGNMs were slightly thicker than those of the SGNMs at the same etching time because of the additional etching time required to punch the additional graphene layer of the BLG. We could not produce GNMs with smaller neck width because upon further etching time longer than 18 s for SGNMs and 23 s for BGNM the some of the holes start to merge due to the imperfection of anisotropic etching. We also estimated the porosity of the GNMs, the relative area of holes to the total area ( $\rho = A_h/A_{tot}$ ) of the sample, by an image analysis and it significantly increases from ~16 % for BGNM21 to ~59 % for BGNM8. The coverage of graphene in nanomesh ( $1 - \rho$ ) is necessary for the calculation of thermal conductivity.

Raman spectroscopy was performed under 633 nm He-Ne laser light excitation to verify the chemical condition of the suspended GNM structures as well as the

spectra of the starting materials of SLG and BLG for comparison, as shown in figure 3.4. For both the SGNMs and the BGNMs, the Raman G and 2D peaks maintain their shape and sharpness although their intensities are slightly lowered compare to those for the pristine samples. This suggests that the  $sp^2$  structures still remain at the basal plain after the etching process. The intensities of D and D' peaks increase with increasing the etching time, which is attributed to the fact that the total length of the disordered edge increases as the holes are enlarged.[58] Figure 3.4c shows a Raman mapping image of successfully transferred graphene & GNMs and fully covered to Au-coated SiNx holey membrane with 2.5  $\mu\text{m}$  holes.

Among the several method for measuring thermal conductivity of 2D materials, such as micro-fabricated electrical heater/thermometer[26], [59], [60] and optothermal Raman method, we chose the optothermal Raman technique[25], [39]–[41] for measuring from suspended geometry of GNMs. The laser light focused on the suspended GNMs at the center of a membrane hole acts as a heating source and the heat flows through the sample to the heat sink, the Au-coated membrane. By varying laser power, one can change the temperature of the sample at the laser-irradiated point and the temperature is estimated by the Raman 2D peak position using a pre-calibrated temperature-2D peak position chart and linear regression. The calibration data is shown in figure 3.5a. For the calibration, we used a low laser power of 0.05 mW to avoid the laser heating. The slopes of the 2D peak position

versus temperature were  $-0.064 \text{ cm}^{-1} \cdot \text{K}^{-1}$ ,  $-0.034 \text{ cm}^{-1} \cdot \text{K}^{-1}$ ,  $-0.050 \text{ cm}^{-1} \cdot \text{K}^{-1}$ , and  $-0.028 \text{ cm}^{-1} \cdot \text{K}^{-1}$  for the SLG, BLG, SGNM and BGNM, respectively. The obtained coefficients are similar to the values for SLG and BLG reported in a previous study[61]. After the calibration the 2D peak position is used as a measure of local sample temperature. Figure 3.5b shows the 2D peak position as a function of the incident laser power. Thermal conductivity can be calculated by a heat-diffusion equation in cylindrical coordinates using the local temperature measured by Raman 2D peak shift and the absorbed laser power.[25], [39]

The absorbed laser power of pristine graphene  $Q$  could be obtained from the difference between the power measured by power meter at an empty hole and that of a graphene-covered hole. The optical absorption of SLG and BLG were measured  $2.9 \pm 1.0 \%$  and  $5.7 \pm 1.6 \%$  at 633 nm wavelength, respectively. The absorbed laser power of GNMs, which were also measured by power meter, have linear correlation with graphene coverage  $(1-\rho)$  and can be expressed as  $Q(1-\rho)$ . In order to calculate the thermal conductivity, we used the heat diffusion equation in cylindrical coordinates from the previous research.[25] The thermal conductivity  $k$  of the graphene or GNMs can be described as

$$k = \frac{\alpha \ln t_0 \left(\frac{R}{r_0}\right)}{2\pi t \left[\frac{T_m - T_0}{(Q - Q_{air})(1 - \rho)}\right]}$$

where  $R$  is the radius of the holes of  $1.25 \mu\text{m}$ ;  $r_0$  is the radius of the laser beam of  $0.27 \mu\text{m}$  from the by knife-edge method[39];  $t$  is the thickness of the graphenes or GNMs;  $\alpha$  is 0.98 for the  $100\times$  objective lens;  $T_m$  is the measured temperature;  $T_0$  is the room temperature;  $\rho$  is the areal porosity of GNMs which was measured by TEM and averaged in figure 3.3;  $Q_{\text{air}}$  is the heat loss in air as

$$Q_{\text{air}} = \int_{r_0}^R 2\pi g(T(r) - T_0)rdr + \pi r_0^2 g(T_m - T_0)$$

and temperature profile  $T(r)$  can be simply adopted from the literature about two-laser Raman thermometry with actual measurement of temperature distribution from the laser,[41]

$$T(r) - T_0 = -\frac{\ln\left(\frac{r}{R}\right)}{\ln\left(\frac{R}{r_0}\right)}(T_m - T_0).$$

In this system, the heat transfer coefficient  $g$  was set as  $2.9 \times 10^4 \text{ W}\cdot\text{m}^{-2}\cdot\text{K}^{-1}$ . [25]

Measured thermal conductivity as a function of temperature from the Raman peak shift of the SLG, BLG, SGNM and BGNM is plotted in figures 3.5c and d. At 305 K, the thermal conductivity of pristine SLG and BLG were approximately  $3,170 \pm 1,280 \text{ W}\cdot\text{m}^{-1}\cdot\text{K}^{-1}$  and  $1,650 \pm 197 \text{ W}\cdot\text{m}^{-1}\cdot\text{K}^{-1}$ , respectively. As temperature increases, the thermal conductivity of the pristine samples gradually decreases to to  $\sim 910 \text{ W}\cdot\text{m}^{-1}\cdot\text{K}^{-1}$  for SLG and  $\sim 550 \text{ W}\cdot\text{m}^{-1}\cdot\text{K}^{-1}$  for BLG, respectively, which are the

representative temperature dependency ( $k \sim T^{-1}$ ) of intrinsic phonon-phonon Umklapp scattering and consistent with previous results.[25], [39], [40] The thermal conductivity of the BLG was lower than that of the SLG because of interlayer phonon scattering.[61], [62] For all the graphene nanomesh samples, thermal conductivity was lower than that measured on the pristine samples,  $<500 \text{ W}\cdot\text{m}^{-1}\cdot\text{K}^{-1}$  in the measured temperature range. With decreases in the neck width of the GNMs, the thermal conductivities gradually decreased from  $\sim 579 \pm 42 \text{ W}\cdot\text{m}^{-1}\cdot\text{K}^{-1}$  for SGNM16 to  $\sim 337 \pm 26 \text{ W}\cdot\text{m}^{-1}\cdot\text{K}^{-1}$  for SGNM12 in the SGNM sample sets and from  $\sim 440 \pm 59 \text{ W}\cdot\text{m}^{-1}\cdot\text{K}^{-1}$  (BGNM21) and  $\sim 220 \pm 28 \text{ W}\cdot\text{m}^{-1}\cdot\text{K}^{-1}$  (BGNM14) to  $\sim 78 \pm 10 \text{ W}\cdot\text{m}^{-1}\cdot\text{K}^{-1}$  (BGNM8) near 350 K in the BGNM samples. Our sub-20 nm GNMs show relatively very low temperature dependence of thermal conductivities from 300 K to 450 K.

Even though conventional thermal conductivity reduction of the solid material of porous structures, which derived by Eucken for the thermal conductivity of cylindrical porous solids,  $\kappa_{\text{solid}} = \kappa_{\text{porous}}(1+2\phi/3)/(1-\phi)$ , [63], [64] the ratio between solid thermal conductivity of SGNM12 and SGNM14 against to SLG was 0.537 and 0.229 and those of BGNM14 and BGNM8 against to BLG was 0.39 and 0.181. Because the classic Eucken model is only valid when the material dimensions are much larger than the phonon MFP, extrinsic phonon-edge scattering from the mesh-edges and phonon spectrum change from phonon confinement lead to a significant

thermal conductivity decrease of our sub-20 nm neck-width GNMs and dramatic discrepancy to the Eucken model. Especially in sub-20 nm nanomesh structure, the phonon energy spectra can be quantized due to the confinement of acoustic phonons which usually decrease phonon group velocity.[65] For the phonon-boundary scattering, the mean free path (MFP) can be described as  $\Lambda = D(1+p)/(1-p)$ , where  $D$  is the nanostructure size and  $p$  is a probability of scattering at the boundary. If the phonon scattering dominantly occurs from rough boundary like our GNM's edge disorders ( $p \rightarrow 0$ ), the  $D$  regulates the phonon MFP equivalently. The phonon MFP in pristine graphene was estimated up to  $\sim 800$  nm at RT[66] while our nanomesh neck-widths  $D$  are in the range from 8 nm to 20 nm and the GNMs inevitably have complex configuration of edges. Therefore, phonon MFP of GNMs can be considerably reduced to comparable dimension of GNM nanostructures. Relatively, electron MFP of pristine graphene is approximately  $\sim 20$  nm,[26] thus, edge disorder can successfully affects thermal transport more strongly than charge transport in our sub-20 nm GNMs. Also, because the extrinsic geometrical scattering including phonon edge scattering is rarely correlated with temperature,[21], [22] less temperature dependence of thermal conductivities of our GNMs are under control of edge phonon scattering regime. Comparing similar neck widths of SGNMs and BGNMs, such as SGNM12 and BGNM14, the thermal conductivity of BGNM14 is still slightly lower than that of SGNM12, which originates from the additional

interlayer phonon scattering or existence of residuals in between two basal plains of BGNMs. Note that the thermal conductivity value for BGNM8 ( $\sim 78 \text{ W}\cdot\text{m}^{-1}\cdot\text{K}^{-1}$ ) is the lowest thermal conductivity among the suspended graphene structures ever reported. This could be achieved dominantly by the edge phonon scattering and modification of phonon dispersion from the sub-10 nm neck width of the nanomesh structure and additionally by interlayer phonon scattering from the bilayer structure.

The temperature-dependent thermopower and electrical conductivity of  $2 \text{ cm} \times 2 \text{ cm}$ -sized graphene and GNMs on the  $\text{SiO}_x/\text{Si}$  substrate were measured by conventional thin film-type thermoelectric measurement systems, as shown in figure 3.6a and b. Carrier concentration and mobility are also important parameters for interpreting the thermoelectric properties. These values were obtained using the Hall effect measurement (figure 3.6c). As the temperature increases from 300 K to 520 K, the Seebeck coefficient gradually increases from  $5 \pm 2 \mu\text{V}\cdot\text{K}^{-1}$  to  $41 \pm 17 \mu\text{V}\cdot\text{K}^{-1}$  for SLG and from  $-22 \pm 20 \mu\text{V}\cdot\text{K}^{-1}$  to  $-120 \pm 21 \mu\text{V}\cdot\text{K}^{-1}$  for BLG, which exhibit an agreement with the semiclassical Mott relation.[67] The sign indicates the p-type and n-type characteristics, for the SLG and BLG, and it may be originated from different doping conditions from different geometries of ambipolar 2D materials. The electrical conductivity of pristine SLG was in the range of  $\sim 4 \times 10^6 \text{ S}\cdot\text{m}^{-1}$  and was slightly higher than that of BLG ( $\sim 2 \times 10^6 \text{ S}\cdot\text{m}^{-1}$ ). The higher absolute value of the thermopower and the lower electrical

conductivity of the BLG compared with the SLG is comparable with previous results[23], [38] and is caused by the lower carrier concentration shown in figure 3. 6c. The difference may result from the one-side (less) surface/substrate doping at each layer of the BLG compared with both-side doping at the SLG.

For the GNMs, the thermopower of SGNM12 gradually increased from  $-12 \pm 5 \mu\text{V}\cdot\text{K}^{-1}$  to  $-150 \pm 27 \mu\text{V}\cdot\text{K}^{-1}$  at the same temperature range, and the electrical conductivity decreased to  $\sim 2 \times 10^5 \text{ S}\cdot\text{m}^{-1}$  which difference is approximately 1 order of magnitude. For the BGNMs, the wider neck width of BGNM14 exhibited higher thermopower from  $-54 \pm 23 \mu\text{V}\cdot\text{K}^{-1}$  to  $-200 \pm 30 \mu\text{V}\cdot\text{K}^{-1}$  and less electrical conductivity ( $\sim 8 \times 10^4 \text{ S}\cdot\text{m}^{-1}$ ) compared with that of SGNM12. Further decreasing the neck width of the BGNMs to 8 nm (BGNM8), the thermopower was considerably higher ( $-190 \pm 80 \mu\text{V}\cdot\text{K}^{-1}$  at 300 K and  $-520 \pm 92 \mu\text{V}\cdot\text{K}^{-1}$  at 520 K), which has not been demonstrated before in carbon-based nano-materials, with decreasing electrical conductivity to  $\sim 2 \times 10^4 \text{ S}\cdot\text{m}^{-1}$ . While the graphene edges from oxygen plasma usually bring the p-type doping by oxygen dangling bonds,[68] our all GNMs showed n-type characteristics. The graphene shows ambipolar transport in FETs, and the major carrier and their concentration was dominantly affected by the doping from the chemical condition of top surface and bottom substrate, and dangling bonds at the edge of the graphene.[69] Therefore, we optimized the temperature of thermal treatment at 400 °C in Ar atmosphere to minimize the effect

of surface/substrate doping and dangling bonds at the edges. The carrier concentration and mobility behavior of the SGNMs and BGNMs were quite different. While the mesh structure in the SGNMs relatively lowered the mobility from  $\sim 700 \text{ cm}^2 \cdot \text{V}^{-1} \cdot \text{s}^{-1}$  to  $\sim 200 \text{ cm}^2 \cdot \text{V}^{-1} \cdot \text{s}^{-1}$  and less reduced the carrier concentration from  $\sim 2 \times 10^{13} \text{ cm}^{-2}$  to  $\sim 5 \times 10^{12} \text{ cm}^{-2}$ , that of the BGNMs fairly conserved the mobility (slightly changed from  $\sim 730$  to  $\sim 530 \text{ cm}^2 \cdot \text{V}^{-1} \cdot \text{s}^{-1}$ ) and significantly reduced the carrier concentrations from  $\sim 1.6 \times 10^{13} \text{ cm}^{-2}$  to  $\sim 2.2 \times 10^{11} \text{ cm}^{-2}$ , at the rate of  $\sim 1/70$  (BGNM8). The significant reduction of the carrier concentration was related to the decreasing basal plain area of the porous GNM structures and severely confined geometry from the narrower neck width. Because the Seebeck coefficient is inversely proportional to the carrier concentration and proportional to temperature for high carrier concentrations, [21]–[23], [70] dramatic decrease of the carrier concentration, especially in the BGNM8, influenced the high thermopower values and high temperature dependency of thermopower.

In order to estimate the effective bandgap of the samples and to investigate its effect on thermoelectric properties, we fabricated GNM FETs on top of a highly doped Si substrate with a 300 nm thick thermally grown SiO<sub>2</sub> using electron beam lithography and O<sub>2</sub> plasma patterning. The fabrication details are described in Supplementary Information. Source drain current (IDS) was measured with an application of a constant source-drain bias voltage (VDS) of 1 mV as a function of

back-gate voltage (VG). Figure 3.6d shows the representative IDS-VDS curves measured for a GNM-FET at various temperatures. The bandgap of the sample is estimated by the Arrhenius plot as shown in the figure 3.10, using the formula of  $IDS = IDS,0 \cdot \exp[E_g/(2kBT)]$ . Here,  $E_g$  is the energy bandgap and  $kB$  is the Boltzmann constant. The measured bandgap of SGNM12 was  $\sim 60$  meV, which is comparable with previous results,[16] whereas the bandgap of the narrower neck-width BGNM8 was  $\sim 25$  meV, considerably lower than that of the SGNMs. This smaller bandgap of BGNMs can be attributed to the interlayer interaction induced parabolic band which leads to larger carrier dispersion near zero energy than the Dirac cones for SGNM. Because the bandgap in graphene has an inverse relationship with carrier mobility,[71] we attributed that our BGNM structures avoid significant loss of mobility for maintaining electrical conductivity, effectively reduce the carrier concentration for increasing Seebeck coefficient. Based on these thermoelectric measurements, we achieved a power factor ( $S^2\sigma$ ) of BGNM8 up to  $\sim 8,200 \mu W \cdot m^{-1} \cdot K^{-2}$  at 520 K due to relatively maintained electrical conductivity and superior thermopower.

Using classical and quantum mechanical calculations, we investigated the effect of both sub-10 nm patterns and cross-plane coupling on thermal conductivity and thermoelectric properties of graphene nanomeshes. The thermal conductivity ( $\kappa$ ) calculations of 42 nm pattern period of GNMs with different coverages were

performed using molecular dynamics simulations,[34], [47]–[49] and our computed  $\kappa$  values are shown in figure 3.7a. The significant reduction in  $\kappa$  for GNM samples is due to the presence of circular edges in nanomesh structure, inducing strong phonon scattering at this edge disorders. With decreasing coverage of GNMs,  $\kappa$  reduces further due to the narrower neck width of the nanomesh structure. Because of the dominant edge-phonon scattering of GNMs, interlayer phonon scattering from the BGNM was relatively less affected to the reduction of thermal conductivity. Our calculated thermal conductivity is on the similar order of magnitude of the experimentally measured value of graphene. For estimations of the electron transport in the GNMs, we employed ab initio electronic structure calculations and the Boltzmann transport approach.[43]–[45] Based on our computed configuration and band structures of GNMs in figure 3.10, the band gap of BGNM is smaller than that of SGNM at the same coverage of GNMs. Figure 3.7b shows our calculated thermopower values as a function of temperature for SGNM and BGNM samples with different coverage. Here, the thermopower values of each sample are obtained at intrinsic carrier concentration of corresponding experimental GNM samples. The coverage of graphene in nanomesh is directly proportional to the carrier concentration, thus, the less coverage GNM has a larger thermopower value. These results suggest that quantum confinement from a narrower neck width and less bandgap from the bilayer structure led to better thermoelectric efficiency.

### 3.4. Conclusion

In conclusion, we fabricated large-sized SGNMs and BGNMs with 8-nm neck widths using BCP self-assembly and firstly measured the thermal conductivity of nano-patterned graphene with unsupported geometry using the optothermal Raman technique and also firstly obtained the thermoelectric properties of nano-patterned graphene. From our measurements, we achieved significantly reduced thermal conductivity of  $\sim 78 \text{ W}\cdot\text{m}^{-1}\cdot\text{K}^{-1}$  from the BGNM with 8 nm neck-width, which is the lowest thermal conductivity of graphene nanostructures, and a maximum thermopower of  $-520 \mu\text{V}\cdot\text{K}^{-1}$  while maintaining their high carrier mobility. Our GNM nanostructures successfully induced dominant phonon-edge scattering within sub-10 nm neck-width scale and quantum confinement for the control of electron and phonon transport behaviors. Because BCP lithography provides a robust fabrication route for forming sub-10 nm nanomesh structure over large areas, our approach can be an excellent platform to investigate the nano-pattern effect or pattern geometry effect on thermal and thermoelectric phenomena of nano-patterned 2D materials including graphene, MoS<sub>2</sub> or other dicalcogenides. And also, the nano-patterned 2D materials can be expected to contribute for obtaining highly efficient and flexible thermoelectric materials for the self-powered devices of wearable electronics.

### 3.5. References

- [1] A. K. Geim, “Graphene: status and prospects.,” *Science* (80-. ), vol. 324, no. 5934, pp. 1530–1534, Jun. 2009.
- [2] J. S. Burgess et al., “Tuning the electronic properties of graphene by hydrogenation in a plasma enhanced chemical vapor deposition reactor,” *Carbon N. Y.*, vol. 49, no. 13, pp. 4420–4426, Nov. 2011.
- [3] S. Zhou, D. Siegel, A. Fedorov, and A. Lanzara, “Metal to Insulator Transition in Epitaxial Graphene Induced by Molecular Doping,” *Phys. Rev. Lett.*, vol. 101, no. 8, p. 086402, Aug. 2008.
- [4] M. Han, B. Özyilmaz, Y. Zhang, and P. Kim, “Energy Band-Gap Engineering of Graphene Nanoribbons,” *Phys. Rev. Lett.*, vol. 98, no. 20, p. 206805, May 2007.
- [5] Z. Chen, Y.-M. Lin, M. J. Rooks, and P. Avouris, “Graphene nano-ribbon electronics,” *Phys. E*, vol. 40, no. 2, pp. 228–232, Dec. 2007.
- [6] K. Nakada, M. Fujita, G. Dresselhaus, and M. Dresselhaus, “Edge state in graphene ribbons: Nanometer size effect and edge shape dependence.,” *Phys. Rev. B*, vol. 54, no. 24, pp. 17954–17961, Dec. 1996.

- [7] X. Li, X. Wang, L. Zhang, S. Lee, and H. Dai, “Chemically derived, ultrasmooth graphene nanoribbon semiconductors.,” *Science* (80-. ), vol. 319, no. 5867, pp. 1229–1232, Mar. 2008.
- [8] L. Jiao, L. Zhang, X. Wang, G. Diankov, and H. Dai, “Narrow graphene nanoribbons from carbon nanotubes,” *Nature*, vol. 458, pp. 877–880, 2009.
- [9] J. Bai, X. Duan, and Y. Huang, “Rational Fabrication of Graphene Nanoribbons Using a Nanowire Etch Mask,” *Nano Lett.*, vol. 9, no. 5, pp. 2083–2087, 2009.
- [10] W. J. Yu and X. Duan, “Tunable transport gap in narrow bilayer graphene nanoribbons.,” *Sci. Rep.*, vol. 3, p. 1248, Jan. 2013.
- [11] D. S. Lee et al., “Quantum Hall effect in twisted bilayer graphene,” *Phys. Rev. Lett.*, vol. 107, no. 21, p. 216602, 2011.
- [12] “International Technology Roadmap for Semiconductors, ITRS 2011 Edition,” 2011.
- [13] F. S. Bates and G. H. Fredrickson, “Block copolymer thermodynamics: theory and experiment.,” *Annu. Rev. Phys. Chem.*, vol. 41, pp. 525–557, Jan. 1990.

- [14] M. Park, C. Harrison, P. M. Chaikin, R. A. Register, and D. H. Adamson, “Block Copolymer Lithography: Periodic Arrays of  $\sim 10^{11}$  Holes in 1 Square Centimeter,” *Science* (80-. ), vol. 276, pp. 1401–1404, May 1997.
- [15] J. Bai, X. Zhong, S. Jiang, Y. Huang, and X. Duan, “Graphene nanomesh.,” *Nat. Nanotechnol.*, vol. 5, no. 3, pp. 190–194, Mar. 2010.
- [16] X. Liang et al., “Formation of bandgap and subbands in graphene nanomeshes with sub-10 nm ribbon width fabricated via nanoimprint lithography.,” *Nano Lett.*, vol. 10, no. 7, pp. 2454–2460, Jul. 2010.
- [17] M. Kim, N. S. Safron, E. Han, M. S. Arnold, and P. Gopalan, “Fabrication and characterization of large-area, semiconducting nanoporated graphene materials.,” *Nano Lett.*, vol. 10, no. 4, pp. 1125–1131, Apr. 2010.
- [18] G. Liu et al., “Epitaxial graphene nanoribbon array fabrication using BCP-assisted nanolithography,” *ACS Nano*, vol. 6, no. 8, pp. 6786–6792, 2012.
- [19] X. Liang and S. Wi, “Transport Characteristics of Multichannel Transistors Made from Densely Aligned Sub-10 nm Half-Pitch Graphene Nanoribbons,” *ACS Nano*, vol. 6, no. 11, pp. 9700–9710, 2012.

- [20] J. G. Son et al., “Sub-10 nm Graphene Nanoribbon Array Field-Effect Transistors Fabricated by Block Copolymer Lithography,” *Adv. Mater.*, vol. 25, pp. 4723–4728, Jun. 2013.
- [21] A. A. Balandin, “Thermal properties of graphene and nanostructured carbon materials,” *Nat. Mater.*, vol. 10, no. 8, pp. 569–581, Aug. 2011.
- [22] Y. Xu, Z. Li, and W. Duan, “Thermal and Thermoelectric Properties of Graphene,” *Small*, vol. 10, no. 11, pp. 2182–2199, Mar. 2014.
- [23] P. Dollfus, V. Hung Nguyen, and J. Saint-Martin, “Thermoelectric effects in graphene nanostructures,” *J. Phys. Condens. Matter*, vol. 27, no. 13, p. 133204, 2015.
- [24] A. A. Balandin et al., “Superior thermal conductivity of single-layer graphene,” *Nano Lett.*, vol. 8, no. 3, pp. 902–907, 2008.
- [25] S. Chen et al., “Thermal conductivity of isotopically modified graphene,” *Nat. Mater.*, vol. 11, no. 3, pp. 203–207, 2012.
- [26] M.-H. Bae et al., “Ballistic to diffusive crossover of heat flow in graphene ribbons,” *Nat. Commun.*, vol. 4, p. 1734, Jan. 2013.
- [27] Y. Ouyang and J. Guo, “A theoretical study on thermoelectric properties of graphene nanoribbons,” *Appl. Phys. Lett.*, vol. 94, p. 263107, 2009.

- [28] H. Sevinçli and G. Cuniberti, “Enhanced thermoelectric figure of merit in edge-disordered zigzag graphene nanoribbons,” *Phys. Rev. B*, vol. 81, no. 11, p. 113401, Mar. 2010.
- [29] Y. Chen, T. Jayasekera, A. Calzolari, K. W. Kim, and M. B. Nardelli, “Thermoelectric properties of graphene nanoribbons, junctions and superlattices,” *J. Phys. Condens. Matter*, vol. 22, no. 37, p. 372202, Sep. 2010.
- [30] F. Mazzamuto et al., “Enhanced thermoelectric properties in graphene nanoribbons by resonant tunneling of electrons,” *Phys. Rev. B*, vol. 83, no. 23, p. 235426, 2011.
- [31] T. Gunst, T. Markussen, A.-P. Jauho, and M. Brandbyge, “Thermoelectric properties of finite graphene antidot lattices,” *Phys. Rev. B*, vol. 84, no. 15, p. 155449, Oct. 2011.
- [32] H. Karamitaheri, M. Pourfath, M. Pazoki, R. Faez, and H. Kosina, “Graphene-Based Antidots for Thermoelectric Applications,” *J. Electrochem. Soc.*, vol. 158, no. 12, pp. K213–K216, 2011.
- [33] H. Karamitaheri, M. Pourfath, R. Faez, and H. Kosina, “Geometrical effects on the thermoelectric properties of ballistic graphene antidot lattices,” *J. Appl. Phys.*, vol. 110, no. 5, p. 054506, 2011.

- [34] J. Y. Kim, J.-H. Lee, and J. C. Grossman, “Thermal transport in functionalized graphene,” *ACS Nano*, vol. 6, no. 10, pp. 9050–9057, 2012.
- [35] J. Y. Kim and J. C. Grossman, “High-Efficiency Thermoelectrics with Functionalized Graphene,” *Nano Lett.*, vol. 15, pp. 2830–2835, 2015.
- [36] C.-R. Wang et al., “Enhanced Thermoelectric Power in Dual-Gated Bilayer Graphene,” *Phys. Rev. Lett.*, vol. 107, no. 18, p. 186602, Oct. 2011.
- [37] S.-G. Nam, D.-K. Ki, and H.-J. Lee, “Thermoelectric transport of massive Dirac fermions in bilayer graphene,” *Phys. Rev. B*, vol. 82, no. 24, p. 245416, Dec. 2010.
- [38] N. Xiao et al., “Enhanced thermopower of graphene films with oxygen plasma treatment,” *ACS Nano*, vol. 5, no. 4, pp. 2749–2755, Apr. 2011.
- [39] W. Cai et al., “Thermal Transport in Suspended and Supported Monolayer Graphene Grown by Chemical Vapor Deposition,” *Nano Lett.*, vol. 10, pp. 1645–1651, 2010.
- [40] S. Chen et al., “Raman measurements of thermal transport in suspended monolayer graphene of variable sizes in vacuum and gaseous environments,” *ACS Nano*, vol. 5, no. 1, pp. 321–328, Jan. 2011.

- [41] J. S. Reparaz et al., “A novel contactless technique for thermal field mapping and thermal conductivity determination: two-laser Raman thermometry,” *Rev. Sci. Instrum.*, vol. 85, no. 3, p. 034901, Mar. 2014.
- [42] D. L. Nika and A. A. Balandin, “Two-dimensional phonon transport in graphene,” *J. Phys. Condens. Matter*, vol. 24, no. 23, p. 233203, 2012.
- [43] G. Kresse and J. Furthmüller, “Efficient iterative schemes for ab initio total-energy calculations using a plane-wave basis set,” *Phys. Rev. B*, vol. 54, no. 16, pp. 11169–11186, 1996.
- [44] G. Kresse, “From ultrasoft pseudopotentials to the projector augmented-wave method,” *Phys. Rev. B*, vol. 59, no. 3, pp. 1758–1775, 1999.
- [45] J. P. Perdew and Y. Wang, “Accurate and simple analytic representation of the electron-gas correlation energy,” *Phys. Rev. B*, vol. 45, no. 23, pp. 13244–13249, 1992.
- [46] G. K. H. Madsen and D. J. Singh, “BoltzTraP. A code for calculating band-structure dependent quantities,” *Comput. Phys. Commun.*, vol. 175, no. 1, pp. 67–71, 2006.
- [47] S. Plimpton, “Fast Parallel Algorithms for Short-Range Molecular Dynamics,” *J. Comput. Phys.*, vol. 117, no. 1, pp. 1–19, 1995.

- [48] D. A. Weitz, D. J. Pine, P. N. Pusey, and R. J. A. Tough, “Nondiffusive Brownian motion studied by diffusing-wave spectroscopy,” *Phys. Rev. Lett.*, vol. 63, no. 16, pp. 1747–1750, 1989.
- [49] S. Viscardy, J. Servantie, and P. Gaspard, “Transport and Helfand moments in the Lennard-Jones fluid. II. Thermal conductivity,” *J. Chem. Phys.*, vol. 126, p. 184513, 2007.
- [50] J. Tersoff, “Modeling solid-state chemistry: Interatomic potentials for multicomponent systems,” *Phys. Rev. B*, vol. 39, no. 8, pp. 5566–5568, 1989.
- [51] J. Tersoff, “Erratum: Modeling solid-state chemistry: Interatomic potentials for multicomponent systems [*Phys. Rev. B*39, 5566 (1989)],” *Phys. Rev. B*, vol. 41, no. 5, p. 3248, 1990.
- [52] L. A. Girifalco, M. Hodak, and R. S. Lee, “Carbon nanotubes, buckyballs, ropes, and a universal graphitic potential,” *Phys. Rev. B*, vol. 62, no. 19, pp. 13104–13110, 2000.
- [53] R. W. Havener, H. Zhuang, L. Brown, R. G. Hennig, and J. Park, “Angle-resolved raman imaging of interlayer rotations and interactions in twisted bilayer graphene,” *Nano Lett.*, vol. 12, no. 6, pp. 3162–3167, 2012.

- [54] K. Kim et al., “Raman Spectroscopy Study of Rotated Double-Layer Graphene: Misorientation-Angle Dependence of Electronic Structure,” *Phys. Rev. Lett.*, vol. 108, no. 24, p. 246103, Jun. 2012.
- [55] Z. Ni, Y. Wang, T. Yu, Y. You, and Z. Shen, “Reduction of Fermi velocity in folded graphene observed by resonance Raman spectroscopy,” *Phys. Rev. B*, vol. 77, p. 235403, 2008.
- [56] H. Cho, H. Park, T. P. Russell, and S. Park, “Precise placements of metal nanoparticles from reversible block copolymer nanostructures,” *J. Mater. Chem.*, vol. 20, no. 24, pp. 5047–5051, 2010.
- [57] J. G. Son, W. K. Bae, H. Kang, P. F. Nealey, and K. Char, “Placement Control of Nanomaterial Block Copolymer Thin Films,” *ACS Nano*, vol. 3, no. 12, pp. 3927–3934, 2009.
- [58] J. Lee et al., “Uniform graphene quantum dots patterned from self-assembled silica nanodots,” *Nano Lett.*, vol. 12, no. 12, pp. 6078–6083, Dec. 2012.
- [59] J. H. Seol et al., “Two-dimensional phonon transport in supported graphene,” *Science (80-. )*, vol. 328, no. 5975, pp. 213–216, Apr. 2010.

- [60] M. T. Pettes, I. Jo, Z. Yao, and L. Shi, "Influence of polymeric residue on the thermal conductivity of suspended bilayer graphene," *Nano Lett.*, vol. 11, no. 3, pp. 1195–1200, 2011.
- [61] H. Li et al., "Thermal conductivity of twisted bilayer graphene," *Nanoscale*, vol. 6, no. 22, pp. 13402–13408, 2014.
- [62] S. Ghosh et al., "Dimensional crossover of thermal transport in few-layer graphene," *Nat. Mater.*, vol. 9, no. 7, pp. 555–558, 2010.
- [63] P. E. Hopkins et al., "Reduction in the thermal conductivity of single crystalline silicon by phononic crystal patterning," *Nano Lett.*, vol. 11, no. 1, pp. 107–112, 2011.
- [64] J. Tang et al., "Holey silicon as an efficient thermoelectric material," *Nano Lett.*, vol. 10, no. 10, pp. 4279–4283, 2010.
- [65] A. Balandin and K. Wang, "Significant decrease of the lattice thermal conductivity due to phonon confinement in a free-standing semiconductor quantum well," *Phys. Rev. B*, vol. 58, no. 3, pp. 1544–1549, 1998.
- [66] S. Ghosh et al., "Extremely high thermal conductivity of graphene: Prospects for thermal management applications in nanoelectronic circuits," *Appl. Phys. Lett.*, vol. 92, p. 151911, 2008.

- [67] Y. M. Zuev, W. Chang, and P. Kim, “Thermoelectric and magnetothermoelectric transport measurements of graphene,” *Phys. Rev. Lett.*, vol. 102, no. 9, pp. 1–4, 2009.
- [68] M. Kim, N. S. Safron, E. Han, M. S. Arnold, and P. Gopalan, “Electronic Transport and Raman Scattering in Size- Controlled Nanoperforated Graphene,” *ACS Nano*, vol. 6, no. 11, pp. 9846–9854, 2012.
- [69] N. D. K. Tu, J. Choi, C. R. Park, and H. Kim, “Remarkable Conversion between n- and p-Type Reduced Graphene Oxide on Varying the Thermal Annealing Temperature,” *Chem. Mater.*, vol. 27, no. 21, pp. 7362–7369, 2015.
- [70] G. J. Snyder and E. S. Toberer, “Complex thermoelectric materials,” *Nat. Mater.*, vol. 7, no. 2, pp. 105–114, 2008.
- [71] J. Wang, R. Zhao, M. Yang, Z. Liu, and Z. Liu, “Inverse relationship between carrier mobility and bandgap in graphene,” *J. Chem. Phys.*, vol. 138, no. 8, p. 084701, 2013.

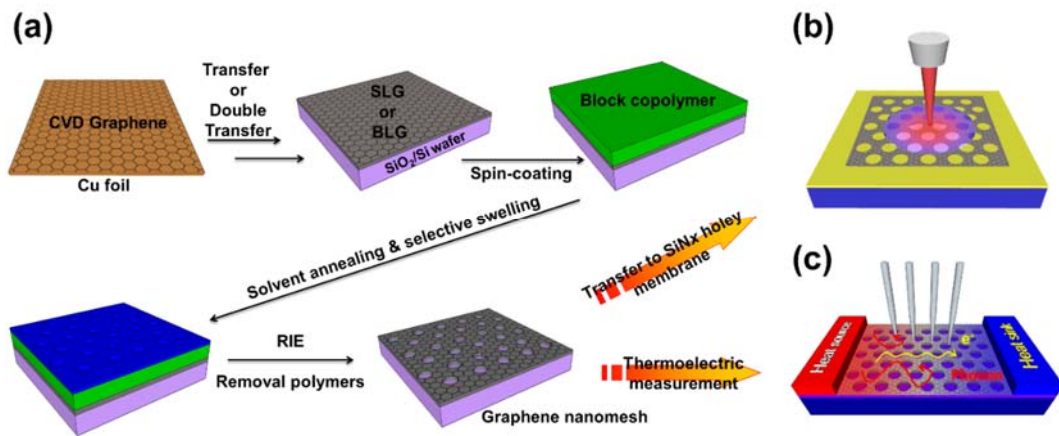
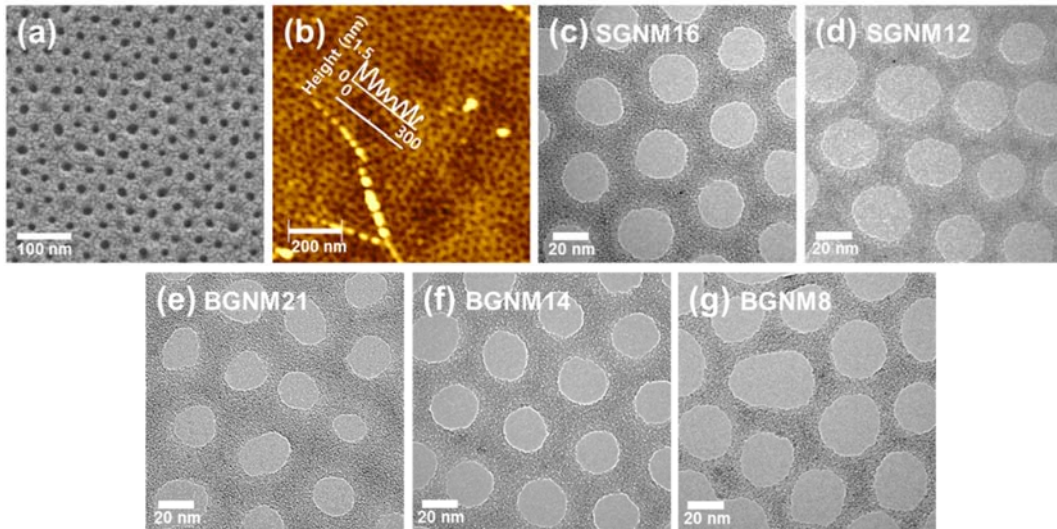
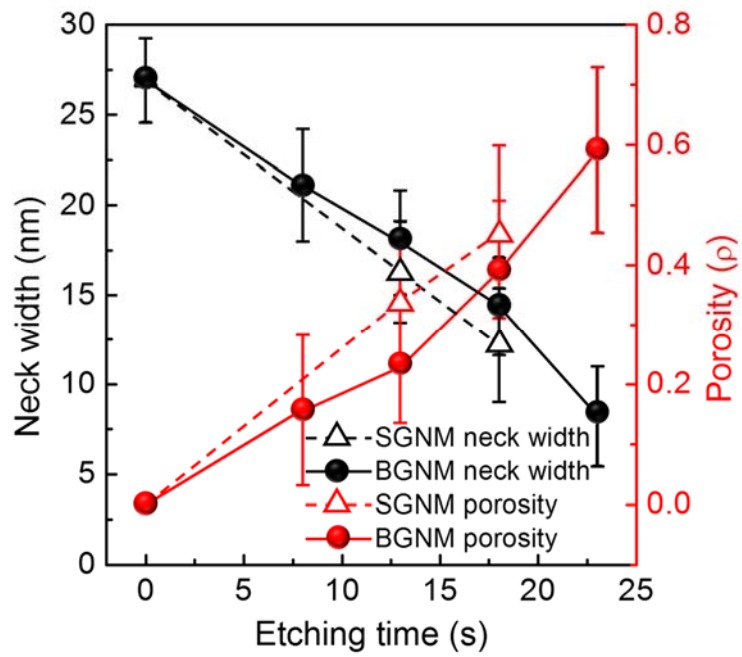


Figure 3.1. Fabrication and thermal measurements of a sub-10 nm GNM.



**Figure 3.2. Structures of the GNM**



**Figure 3.3. Neck width and porosity of the GNMs. Neck width and porosity of the SGNMs and BGNMs as a function of RIE time from the image analysis.**

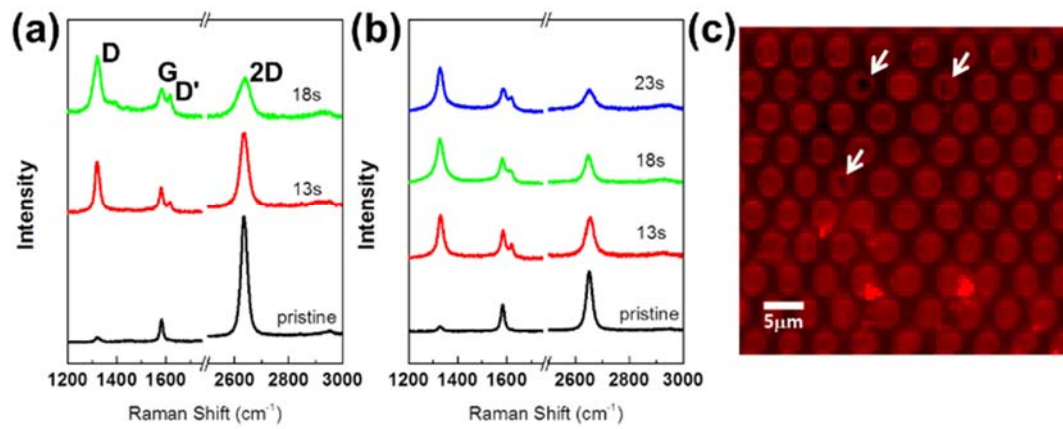


**Figure 3.4. Raman spectra and mapping image of the GNMs.**

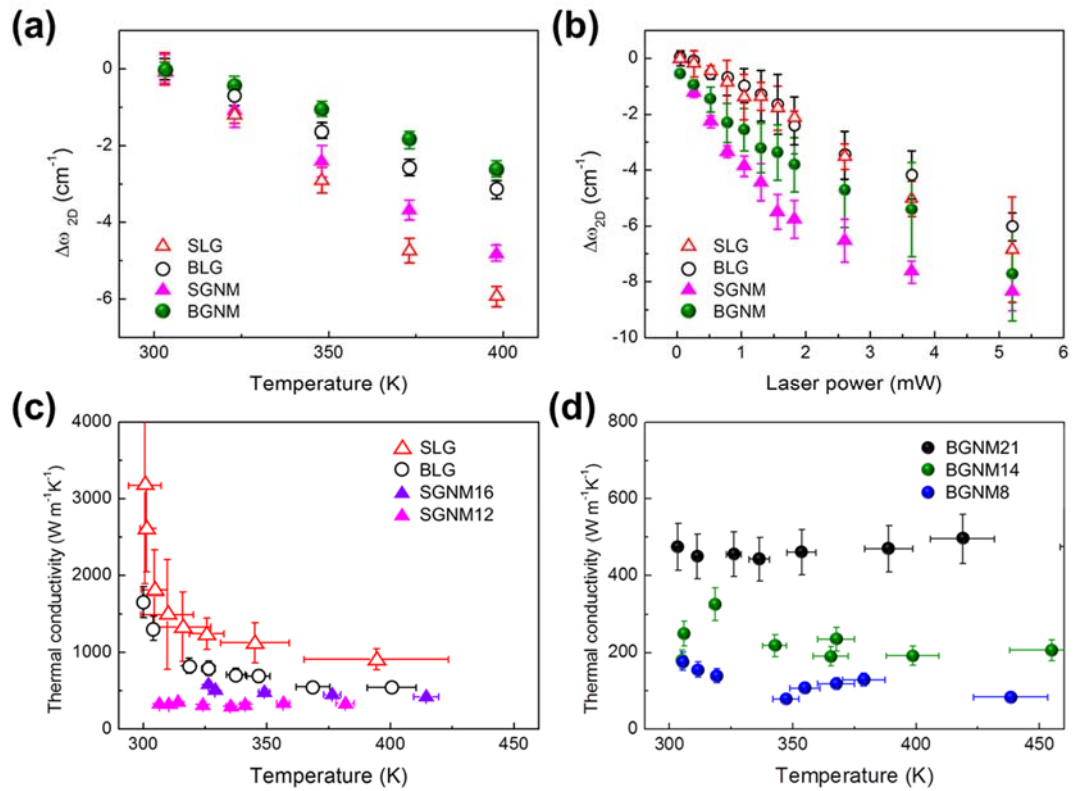


**Figure 3.5. Thermal conductivity of the suspended SLG, BLG, SGNM and BGNM using an optothermal Raman technique**

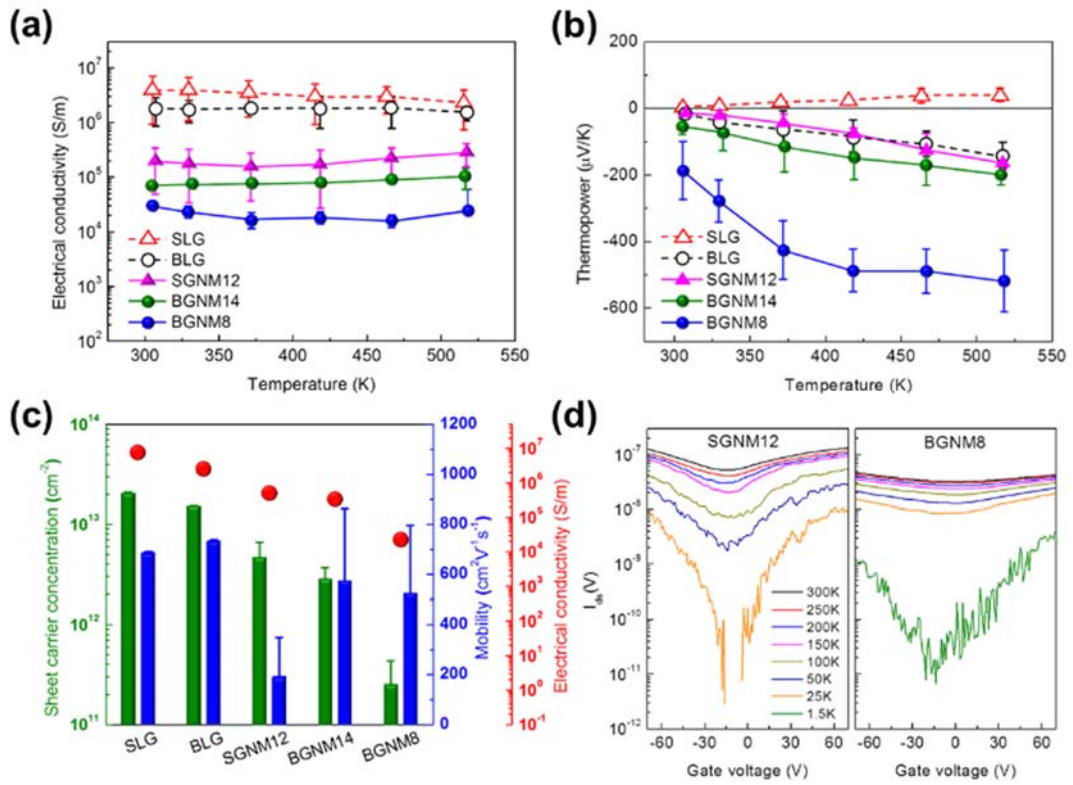
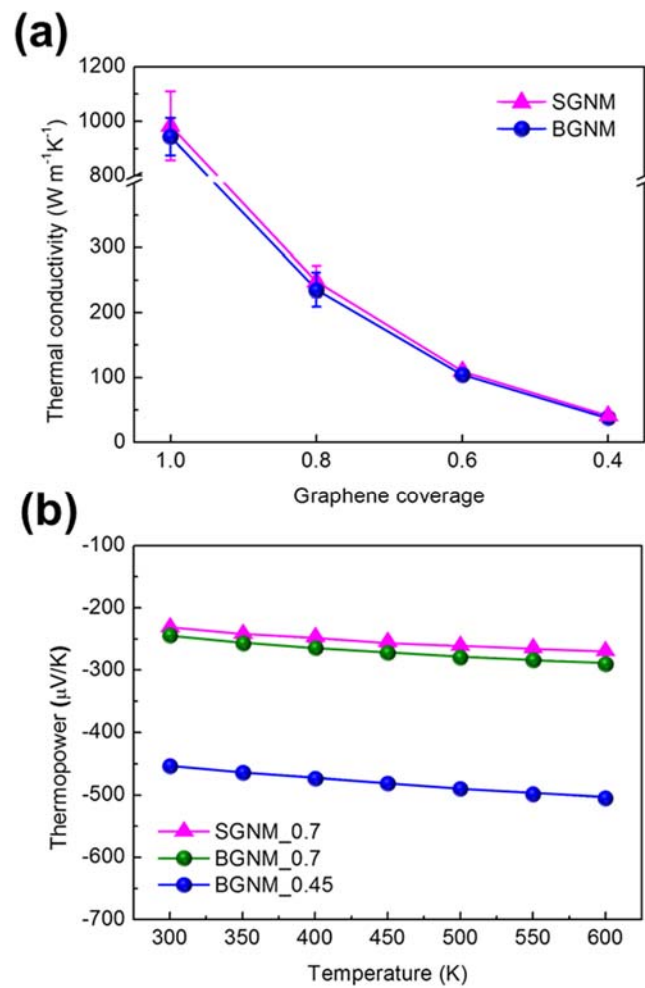
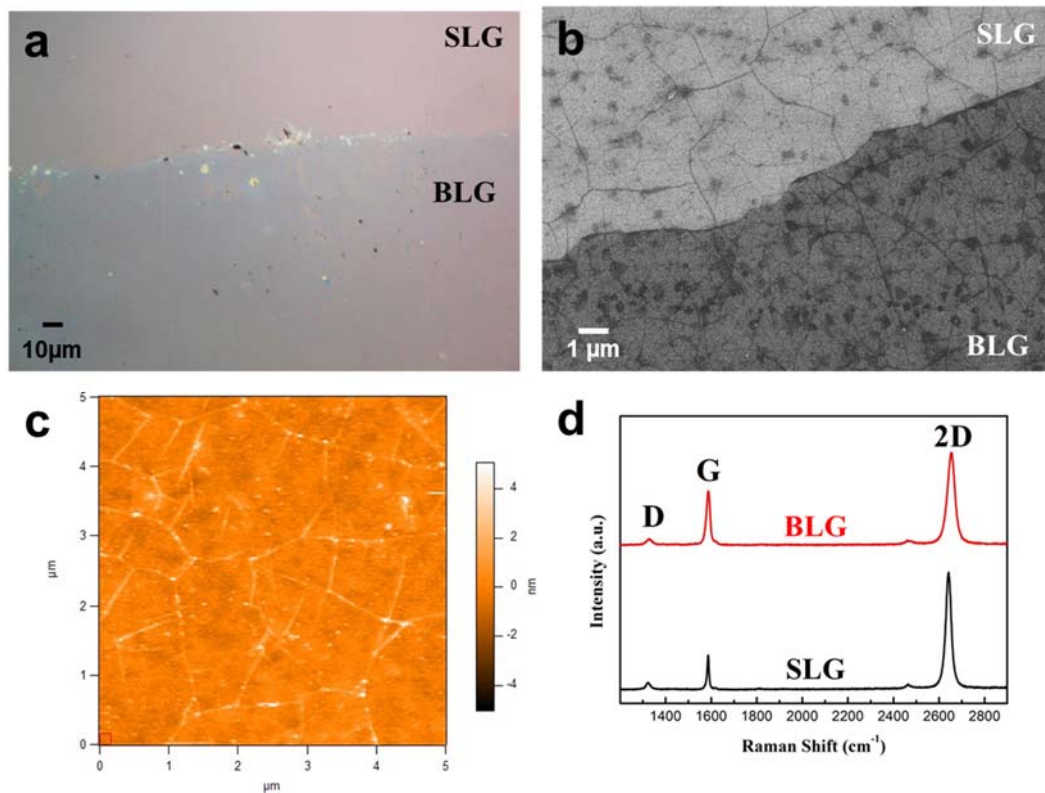


Figure 3.6. Electric and thermoelectric properties of graphenes and GNMs.



**Figure 3.7. Theoretical prediction of thermal conductivity and thermoelectric properties of graphenes and GNMs.**



**Figure 3.8. (a) Optical microscope image and (b) SEM image of edge area between CVD grown single layer graphene (SLG) and repeatedly transferred bilayer graphene (BLG) on SiO<sub>2</sub> (100 nm)/Si substrates.**

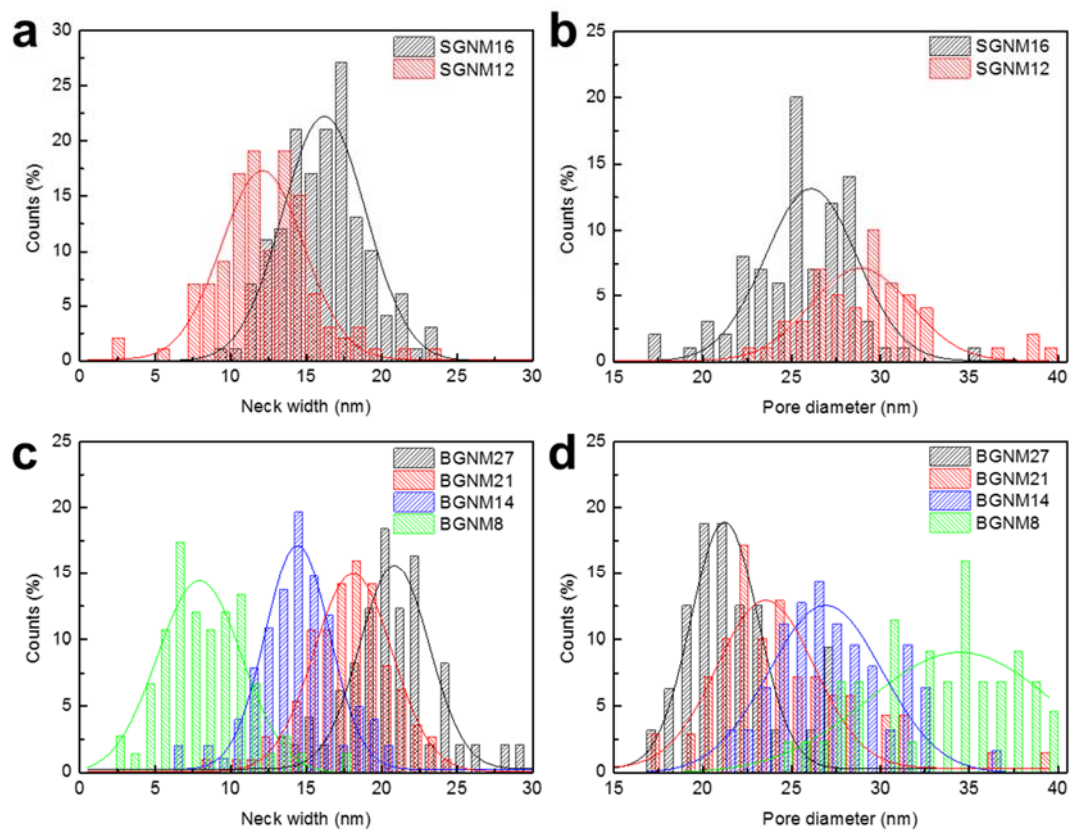


**Figure 3.9.** The radius of (a, c) neck width and (b, d) pore diameter of (a, b) SGNM and (c, d) BGNM as a function of RIE time.

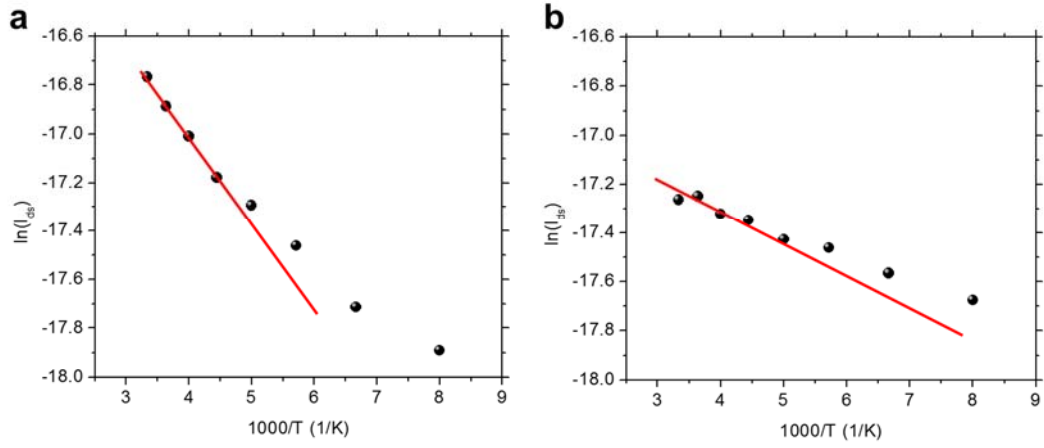


**Figure 3.10.** Arrhenius plot for the conductivity of a, SGNM12 and b, BGNM8 plotted with respect to the inverse of the operating temperature from 150 K to 300 K.

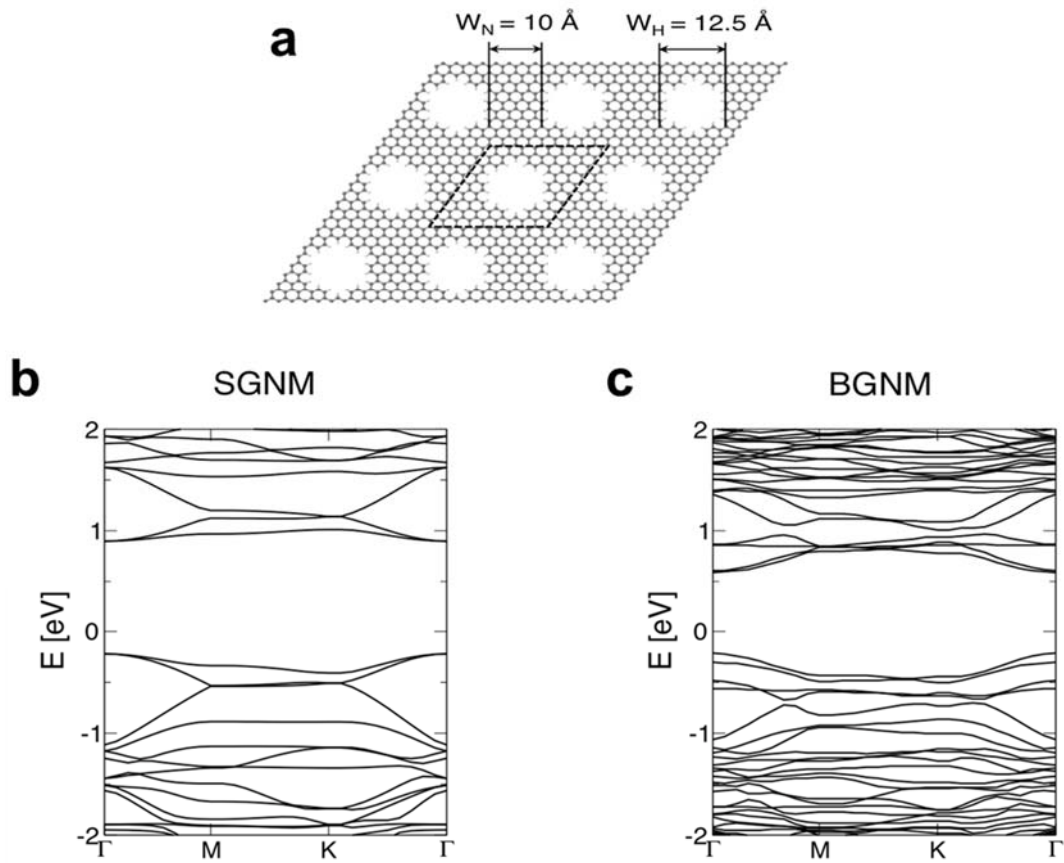


**Figure 3.11. (a) Structure and (b and c) theoretical prediction of thermal conductivity and thermoelectric properties of graphenes and GNMs.**

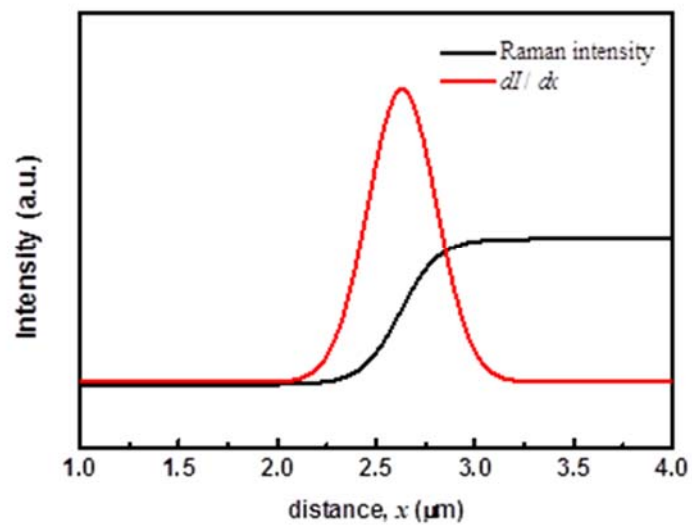
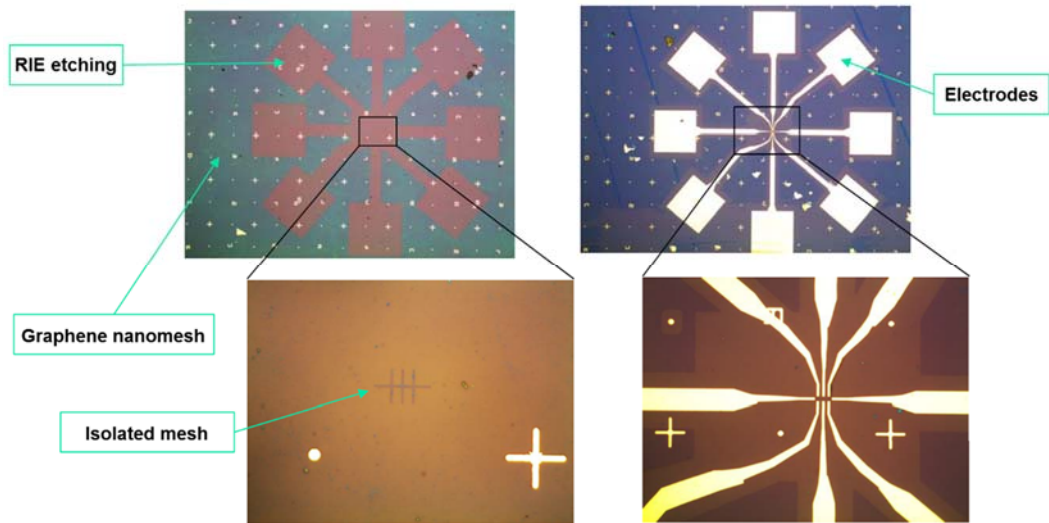


Figure 3.12. Raman intensity at 520 cm<sup>-1</sup> of cleaved Au/Si substrate



**Figure 3.13. The fabrication process of cross-shaped isolated mesh area and source and drain electrodes of the GNM FETs using E-beam lithography.**

## **Chapter 4**

# **Van der Waals Heterostructure of Graphene Nanostructure and Molybdenum Disulfide for Superior Thermoelectric Materials**

## 4.1. Introduction

Thermoelectric materials that can generate electricity from waste heat will play an important role in the global sustainable energy solution[1]–[3] . Low dimensional materials open new routes to high performance thermoelectric properties due to their unique density of states with confined electrons and holes[4]–[8]. Two dimensional transition metal dicalcogenides (TMDCs) represent a new class of high performance thermoelectric materials[9]. 2 D molybdenum disulfide ( $\text{MoS}_2$ ) is one of TMDCs which have high thermopower and very low thermal conductivity[6]. The theoretical Seebeck coefficient of suspended  $\text{MoS}_2$  is over  $500 \mu\text{V}\cdot\text{K}^{-1}$  and the theoretical electrical conductivity is  $100,000 \text{ S}\cdot\text{m}^{-1}$  at room temperature[10]. The theoretical power factor ( $S^2\cdot\sigma$ ) is over  $10,000 \mu\text{W}\cdot\text{m}^{-1}\text{K}^{-2}$  at 300 K. However, the difficulty of measuring the electrical conductivity, thermal conductivity and thermoelectrical properties of  $\text{MoS}_2$ , the experimental study is still limited. [11], [12].

To modify the properties of 2 D materials including graphene and  $\text{MoS}_2$ , heterostructure of 2 D materials comes into limelight[9], [13], [14]. The properties of heterostructure can be tuned by changing the materials, directions, orders and even sizes. Vertical and parallel heterostructures are reported by several

researchers[9], [13], and the materials has superior properties than single 2 D materials. MoS<sub>2</sub> with 1.89 eV direct bandgap has low electrical conductivity[15], it means that to apply MoS<sub>2</sub> with large area, the electrical conductivity should be enhanced. Several approaches to enhance the electrical conductivity of the MoS<sub>2</sub>, such as treating MoS<sub>2</sub> with chemical dopant, changing the phase of the MoS<sub>2</sub>.

Meanwhile, graphene, 2D carbon allotrope with superior electrical and thermal properties are widely used as an electrode for thin film materials[16]–[18]. Hence the electrical conductivity of the graphene is very high level up to  $10^7 \text{ S}\cdot\text{m}^{-1}$ [16], the graphene electrode can be used for the current collectors[19]. However, the Seebeck coefficient of the single layer graphene is only  $\sim 100 \mu\text{V}\cdot\text{K}^{-1}$ [20], applying graphene into thermoelectrics is not widely used. On the other hand, nano patterned graphene shows significantly enhanced thermoelectric properties and reduced thermal conductivity[8], [21]–[25]. In case of graphene nano ribbons, the Seebeck coefficient enhancement is achieved while the electrical conductivity keeps high with carrier confinement effect[26]–[30]. In this paper, we prepared graphene nano ribbons (GNRs) from CVD graphene and block copolymer self-assembly to enhance the electrical property of MoS<sub>2</sub> selectively. GNRs have electrical conductivity individually, however, the electrical conductivity in centimeter scale cannot be measured as the GNR is disconnected to each other. GNRs were transferred to CVD grown MoS<sub>2</sub> which has lower electrical

conductivity, but has superior thermoelectric properties. By introducing heterostructure of GNRs and MoS<sub>2</sub>, the heteromaterial with high electrical conductivity, high Seebeck coefficient and low thermal conductivity could be achieved.

## **4.2. Experimental**

### **Preparation of MoS<sub>2</sub> from CVD method**

Atomic layer of molybdenum disulfide was prepared by chemical vapor deposition (CVD). MoS<sub>2</sub> was grown on SiO<sub>2</sub>/Si with 300 nm oxide layer directly. SiO<sub>2</sub>/Si wafer was cleaned using organic solvent. Baking process and oxygen plasma treatment was followed. Branched polyethylenimine (MW 800 g/mol) 1% solution was spin coated to the substrate, and baked at 120 °C in vacuum for 30 min. After baking process, PEI thin film was washed with DI water several times to remove extra PEI. PEI treated substrate was dipped into ammonium tetrathiomolybdate (ATM) 10 mM solution for 10 min, and rinsed with DI water several times and baked at 120 °C in vacuum for 30 min. ATM/PEI coated substrate was placed to the furnace and baked at 700 °C for 1 hour. ATM decomposed at 500 °C to MoS<sub>2</sub>, and PEI decomposed perfectly over 400 °C. MoS<sub>2</sub> layer from this process is used right after thermolysis.

### **Fabrication of graphene**

Graphene was prepared by chemical vapor deposition method. First, copper foil (Alfa Aesar) with 25 μm thickness was cleaned with acetone, methanol

and IPA and dried with N<sub>2</sub>. Cleaned copper foil was put into the furnace and lower the pressure to  $2.3 \times 10^{-4}$  Torr level. Waiting for 5 minutes, 100 sccm of 99.999% hydrogen gas was flowed for 30 min and ramp the temperature to 1000 °C at the heating rate of 30 °C/min. The copper foil is annealed at 1000 °C with hydrogen flow for 30 min again to flat the surface of the foil. To grow graphene, 100 sccm of 99.999% methane gas and 40 sccm of 99.999% hydrogen gas was flowed for 10 min. at 1000 °C. After the growth process, the chamber is cooled down rapidly within 20 min. To transfer graphene, poly(methyl methacrylate) (MW: 350,000 g/mol) 4% anisole solution is spin coated as an assistance layer. Copper was etched by immersing in a 114 g/L of ammonium persulfate ((NH<sub>4</sub>)<sub>2</sub>S<sub>2</sub>O<sub>8</sub>) aqueous solution for 1 hour and PMMA/graphene film floating on the Cu etchant was washed by D.I. water several times. PMMA/graphene film was transferred by scooping up to the device or substrate and dried at 60 °C. To fabricate fine quality graphene, solvent annealing process was done. PMMA coated graphene on the substrate was put into a jar of 9.7 ml with acetone and sealed with controlled vent and the jar was put in the hood for an hour to spread the film to the substrate perfectly. After the solvent annealing process, PMMA was removed by dipping into acetone for 30 min and rinsed using methanol and IPA. To prevent contamination, graphene on substrate was kept in the vacuum.

## **Preparation of graphene nanoribbon from block copolymer self-assembly**

Polystyrene-block-poly(2-vinylpyridine) (PS-b-P2VP) (MW: 50,000 g/mol – 17,500 g/mol) 0.3 wt% solution in chloroform is spin coated directly onto bilayer graphene to form 30 nm thin film of block copolymer. PS-b-P2VP film is solvent annealed by tetrahydrofuran in 9.3 ml chamber with controlled leakage to form the cylinder patterns. The cylinder pattern of PS-b-P2VP is applied as a mask for lithography process. Oxygen plasma treatment was done for 25 s to 35 s to control the line width of the GNR. After oxygen plasma treatment, the polymeric residue was removed by thermal annealing at 500 °C.

## **Fabrication of GNR/MoS<sub>2</sub> van der Waals Heterostructure**

PMMA is spin coated to GNR as an assistance layer. Sacrificial layer of substrate was removed by dipping in HF 5% solution for 10 min, then PMMA/GNR is floating on HF solution. PMMA/GNR is carefully fishing out to fresh water 2 ~ 3 times and fishing again with MoS<sub>2</sub> on SiO<sub>2</sub>/Si wafer. To remove water molecules between the junction of GNR and MoS<sub>2</sub>, further thermal annealing was processed at 200 °C. After the thermal annealing process, acetone rinsing was followed to remove PMMA assistance layer.

## **Characterization of GNR/MoS<sub>2</sub> van der Waals Heterostructure**

To measure TEM. GNR MoS<sub>2</sub> was transferred again to silicon nitride (SiN<sub>x</sub>) TEM grid with 2.5 μm hole diameter without supporting layer. Raman spectroscopy of heterostructure was also taken from suspended heterostructure. The thermal conductivity of heterostructure was measured by optothermal Raman technique. The details of optothermal Raman technique is discuss in result and discussions. The Seebeck coefficient was measured with Seepel machine, which build -2, -1, 0, 1 and 2 K of temperature difference and measuring the thermoelectric voltage and the reliability is 0.99 for each samples.

### 4.3. Results and Discussion

Electrical and thermoelectric properties of MoS<sub>2</sub> was measured after chemical doping MoS<sub>2</sub> by benzyl viologen (BV)[31]. By doping MoS<sub>2</sub> with BV, the electrical conductivity is dramatically enhanced to several S/m, however the Seebeck coefficient is reduced to several hundreds  $\mu\text{V/K}$ . Hence MoS<sub>2</sub> with BV is stable in water unlike pristine MoS<sub>2</sub>, GNR could be fished up with MoS<sub>2</sub> with BV on substrate. By doping MoS<sub>2</sub> film, the electrical conductivity could be measured in centimeter scale. The electrical conductivity of MoS<sub>2</sub> single layer has a semi conducting properties, so the electrical conductivity could be tuned by chemical doping or external environmental conditions[15]. The electrical conductivity of doped MoS<sub>2</sub> is enhanced to 1 S/m.

To enhance the electrical conductivity of the MoS<sub>2</sub>, graphene nanoribbon was applied to the top of the MoS<sub>2</sub> film. GNR was prepared by BCP nanolithography[26],[32]. Graphene transferred to SiO<sub>2</sub>/Si wafer was covered by PS-b-P2VP thin film. Using THF as a solvent annealing material, parallel cylinder pattern was produced. Line width of GNR could be controlled by changing the oxygen plasma etching time from 20 s to 35 s. The morphology of GNR is shown in figure 4.8. To control the electrical and thermoelectrical properties, the line width

should be tuned from tens of nanometer to sub-10 nanometers. The electrical conductivity of GNR cannot be measured in centimeter scale with 4-point probe. GNR with different line width is coated by PMMA and transferred to MoS<sub>2</sub> film.

The morphology and the quality of GNR/MoS<sub>2</sub> heterostructure were measured by transmission electron microscope (TEM) and Raman spectroscopy. TEM image and selected area electron diffraction (SAED) show GNR/MoS<sub>2</sub> heterostructure was successfully prepared by our methods. In SAED patterns, the inner hexagonal peaks indicate MoS<sub>2</sub> monolayer and outer doubled hexagonal peaks indicate bilayer graphene nanoribbons on MoS<sub>2</sub>. Hence the lattice size of the MoS<sub>2</sub> is larger than that of graphene, the SAED pattern of MoS<sub>2</sub> is shown in narrower q-values. Randomly produced GNR structure is observed with TEM, which is encouraged structure for measuring the thermal conductivity. The thermal conductivity is measured with optothermal Raman technique, which calculates the thermal conductivity from the heat dissipation. GNR with randomly oriented morphology could spread heat and electron randomly, which makes optothermal Raman technique trustable.

The Raman spectroscopy of GNR/MoS<sub>2</sub> heterostructure is displayed in Figure 4.4. The signature peak of MoS<sub>2</sub> is shown in the range of 383 ~ 430 cm<sup>-1</sup>, and the that of graphene is shown around 1580 cm<sup>-1</sup> and 2600 cm<sup>-1</sup>. Figure 4.5

shows the Raman trace of signature peaks of MoS<sub>2</sub> (383 cm<sup>-1</sup>) and graphene (1580 cm<sup>-1</sup>) in suspended GNR/MoS<sub>2</sub> heterostructure. GNR/MoS<sub>2</sub> heterostructure is well formed and transferred perfectly to the silicon nitride TEM grid. The thermal conductivity and the thermoelectric power will be measured within several months.

To measure electrical properties of GNR/MoS<sub>2</sub> heterostructure, we measured the electrical conductivity as a function of temperature. GNR/MoS<sub>2</sub> shows significantly enhanced electrical conductivity about 1000 times than BV doped MoS<sub>2</sub>. It is the highest value for MoS<sub>2</sub> single layer materials. However, the contact resistance affects to the electrical properties of GNR/MoS<sub>2</sub> heterostructure, the contact of two atomic layer should be tuned to have lower contact resistances.

## 4.4. Conclusion

In this part, we introduced graphene nanoribbon/molybdenum disulfide van der Waals heterostructure having higher electrical conductivity. We assumed that GNR which has higher electrical conductivity than MoS<sub>2</sub> will act as highways for electron to enhance the electrical conductivity and mobility. We successfully fabricate the heterostructure of GNR and MoS<sub>2</sub> heterostructure with block copolymer nanolithography, and the dimension of the materials was tuned. However, the thermal properties and thermoelectric properties were not measured yet. The contact resistance between GNR and MoS<sub>2</sub> should be tuned with chemical doping or thermal annealing process, the heterostructure with enhanced thermoelectric properties can be gained.

## 4.5 Reference

- [1] S. J. Kim, J. H. We, and B. J. Cho, “A wearable thermoelectric generator fabricated on a glass fabric,” *Energy Environ. Sci.*, vol. 7, pp. 1959–1965, 2014.
- [2] O. Bubnova et al., “Optimization of the thermoelectric figure of merit in the conducting polymer poly ( 3 , 4-ethylenedioxythiophene ),” *Nat. Mater.*, vol. 10, no. 6, pp. 429–433, 2011.
- [3] H. Cheng et al., “Flexible cellulose-based thermoelectric sponge towards wearable pressure sensor and energy harvesting,” *Chem. Eng. J.*, vol. 338, no. September 2017, pp. 1–7, 2018.
- [4] K. Hippalgaonkar et al., “High thermoelectric power factor in two-dimensional crystals of MoS<sub>2</sub> Kedar,” *Phys. Rev. B*, vol. 95, no. 11, p. 115407, 2017.
- [5] S. Ghosh et al., “Dimensional crossover of thermal transport in few-layer graphene.,” *Nat. Mater.*, vol. 9, no. 7, pp. 555–558, 2010.
- [6] H. G. Shin et al., “Vertical and In-Plane Current Devices Using NbS<sub>2</sub>/n-MoS<sub>2</sub> van der Waals Schottky Junction and Graphene Contact,” *Nano Lett.*, vol. 18, no. 3, pp. 1937–1945, 2018.
- [7] M. R. Neupane, “Electronic and vibrational properties of 2D materials from monolayer to bulk,” 18th Int. Work. Comput. Electron. IWCE 2015, pp. 2–3, 2015.

- [8] J. Oh et al., “Significantly reduced thermal conductivity and enhanced thermoelectric properties of single- and bi-layer graphene nanomeshes with sub-10 nm neck-width,” *Nano Energy*, vol. 35, no. January, pp. 26–35, 2017.
- [9] Y. Liu et al., “Thermal Conductance of the 2D MoS<sub>2</sub>/h-BN and graphene/h-BN Interfaces,” *Sci. Rep.*, vol. 7, no. March, pp. 1–8, 2017.
- [10] J. Y. Oh et al., “Chemically exfoliated transition metal dichalcogenide nanosheet-based wearable thermoelectric generators,” *Energy Environ. Sci.*, vol. 9, no. 5, pp. 1696–1705, 2016.
- [11] M. P. Zaitlin and A. C. Anderson, “Phonon thermal transport in noncrystalline materials,” *Phys. Rev. B*, vol. 12, no. 10, pp. 4475–4486, 1975.
- [12] J. H. Seol et al., “Two-dimensional phonon transport in supported graphene,” *Science (80-. )*, vol. 328, no. 5975, pp. 213–216, Apr. 2010.
- [13] Y. Chen et al., “High-Performance Photovoltaic Detector Based on MoTe<sub>2</sub>/MoS<sub>2</sub> Van der Waals Heterostructure,” *Small*, vol. 1703293, p. 1703293, 2018.
- [14] J. Tersoff, “Modeling solid-state chemistry: Interatomic potentials for multicomponent systems,” *Phys. Rev. B*, vol. 39, no. 8, pp. 5566–5568, 1989.
- [15] K. F. Mak, C. Lee, J. Hone, J. Shan, and T. F. Heinz, “Atomically thin MoS<sub>2</sub>: A new direct-gap semiconductor,” *Phys. Rev. Lett.*, vol. 105, no. 13, pp. 2–5, 2010.

- [16] X. Li et al., “Large area synthesis of high quality and uniform graphene films on copper foils,” *Science* (80-. ), vol. 324, no. 5932, pp. 1312–1314, 2009.
- [17] K. S. Novoselov et al., “Two-dimensional gas of massless Dirac fermions in graphene,” *Nature*, vol. 438, no. 7065, pp. 197–200, 2005.
- [18] J. Y. Kim, J.-H. Lee, and J. C. Grossman, “Thermal transport in functionalized graphene,” *ACS Nano*, vol. 6, no. 10, pp. 9050–9057, 2012.
- [19] J. Jiang et al., “Effect of Graphene Modified Cu Current Collector on the Performance of Li<sub>4</sub>Ti<sub>5</sub>O<sub>12</sub> Anode for Lithium-Ion Batteries,” *ACS Appl. Mater. Interfaces*, vol. 8, no. 45, pp. 30926–30932, 2016.
- [20] X. Li, J. Yin, J. Zhou, Q. Wang, and W. Guo, “Exceptional high Seebeck coefficient and gas-flow-induced voltage in multilayer graphene,” *Appl. Phys. Lett.*, vol. 100, no. 18, 2012.
- [21] M. Kim, N. S. Safron, E. Han, M. S. Arnold, and P. Gopalan, “Fabrication and characterization of large-area, semiconducting nanoporated graphene materials,” *Nano Lett.*, vol. 10, no. 4, pp. 1125–1131, Apr. 2010.
- [22] Y. H. Lee, J. Oh, S. S. Lee, H. Kim, and J. G. Son, “Highly Ordered Nanoconfinement Effect from Evaporation-Induced Self-Assembly of Block Copolymers on In Situ Polymerized PEDOT:Tos,” *ACS Macro Lett.*, vol. 6, no. 4,

pp. 386–392, 2017.

[23] A. A. Balandin, “Thermal properties of graphene and nanostructured carbon materials.,” *Nat. Mater.*, vol. 10, no. 8, pp. 569–581, Aug. 2011.

[24] T. Feng and X. Ruan, “Ultra-low thermal conductivity in graphene nanomesh,” *Carbon N. Y.*, vol. 101, pp. 107–113, 2016.

[25] J. Bai, X. Zhong, S. Jiang, Y. Huang, and X. Duan, “Graphene nanomesh.,” *Nat. Nanotechnol.*, vol. 5, no. 3, pp. 190–194, Mar. 2010.

[26] G. Liu et al., “Epitaxial graphene nanoribbon array fabrication using BCP-assisted nanolithography,” *ACS Nano*, vol. 6, no. 8, pp. 6786–6792, 2012.

[27] F. Mazzamuto et al., “Enhanced thermoelectric properties in graphene nanoribbons by resonant tunneling of electrons,” *Phys. Rev. B*, vol. 83, no. 23, p. 235426, 2011.

[28] J. Bai, X. Duan, and Y. Huang, “Rational Fabrication of Graphene Nanoribbons Using a Nanowire Etch Mask,” *Nano Lett.*, vol. 9, no. 5, pp. 2083–2087, 2009.

[29] Y. Ouyang and J. Guo, “A theoretical study on thermoelectric properties of graphene nanoribbons,” *Appl. Phys. Lett.*, vol. 94, p. 263107, 2009.

[30] M. Han, B. Özyilmaz, Y. Zhang, and P. Kim, “Energy Band-Gap

Engineering of Graphene Nanoribbons,” *Phys. Rev. Lett.*, vol. 98, no. 20, p. 206805, May 2007.

[31] D. Kiriya, M. Tosun, P. Zhao, J. S. Kang, and A. Javey, “Air-stable surface charge transfer doping of MoS<sub>2</sub> by benzyl viologen,” *J. Am. Chem. Soc.*, vol. 136, no. 22, pp. 7853–7856, 2014.

[32] J. G. Son et al., “Sub-10 nm Graphene Nanoribbon Array Field-Effect Transistors Fabricated by Block Copolymer Lithography,” *Adv. Mater.*, vol. 25, pp. 4723–4728, Jun. 2013.



**Figure 4.1. Preparation of GNR/MoS<sub>2</sub> heterostructure**

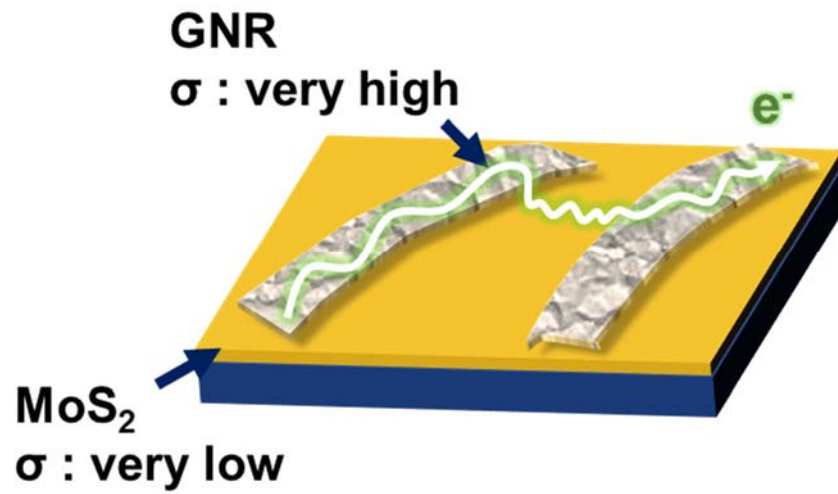


Figure 4.2. Schematic image of GNR/MoS<sub>2</sub> heterostructure

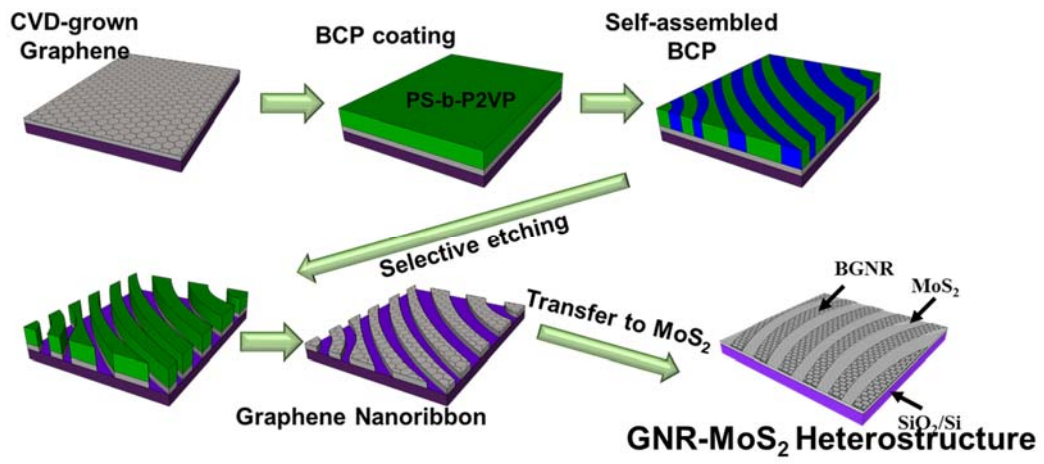
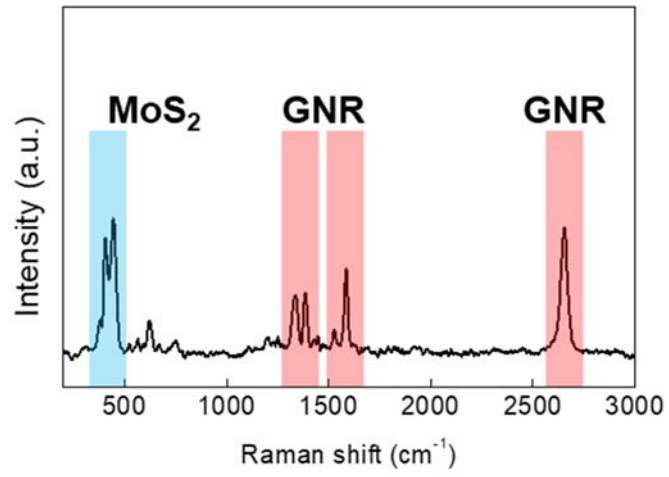
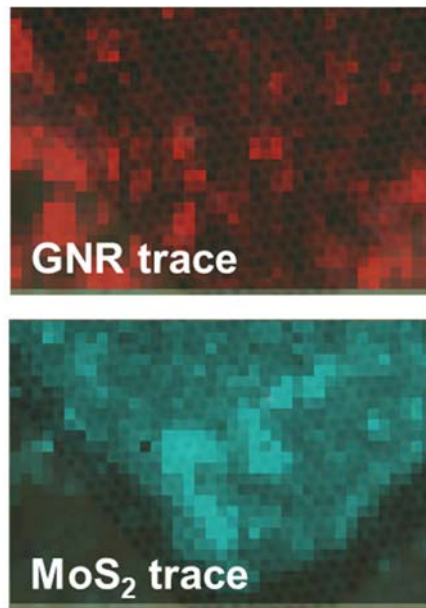


Figure 4.3. Schematic image of preparation of GNR/MoS<sub>2</sub> heterostructure



**Figure 4.4. Raman spectroscopy of GNR/MoS<sub>2</sub> heterostructure**



**Figure 4.5. Raman mapping of GNR/MoS<sub>2</sub> heterostructure.**

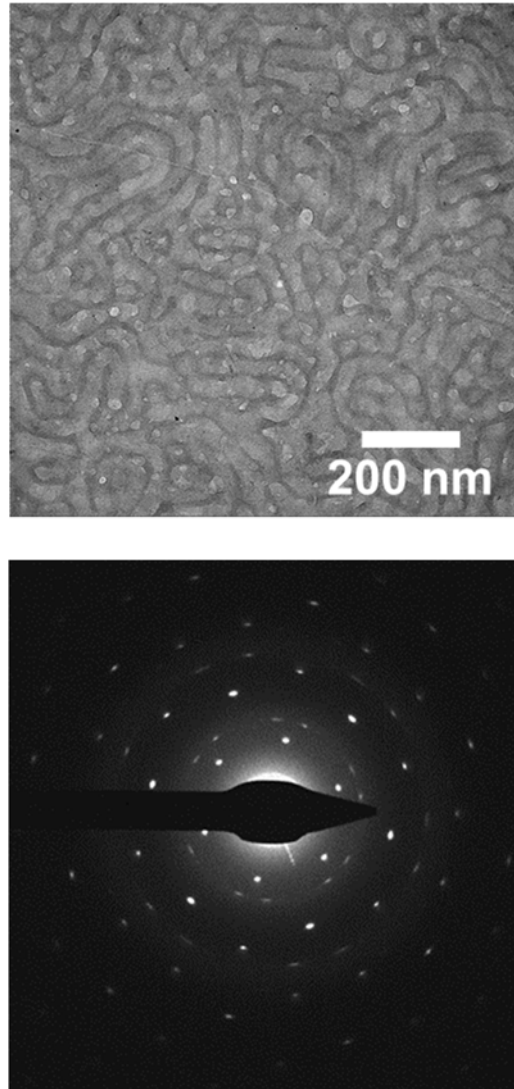


**Figure 4.6. TEM image and SAED pattern of GNR/MoS<sub>2</sub> heterostructure**

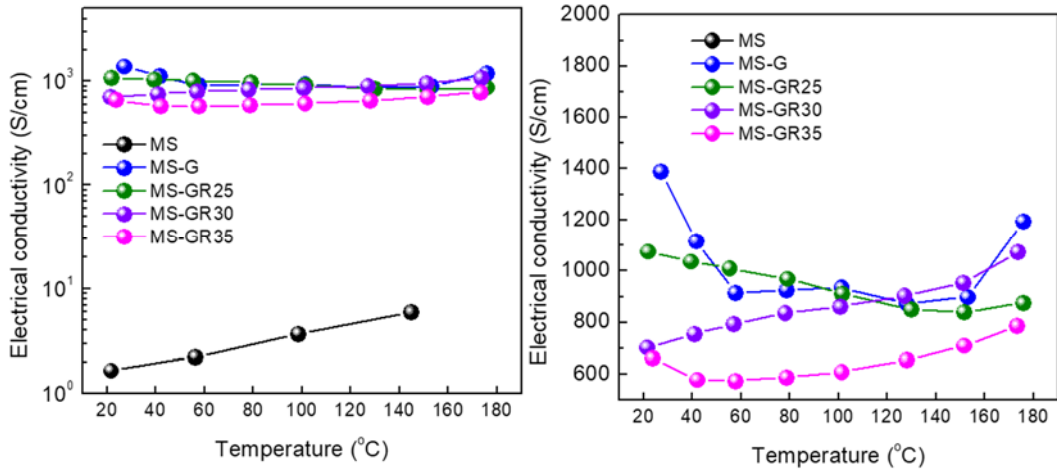


**Figure 4.7. The electrical conductivity of GNR/MoS2 heterostructure**

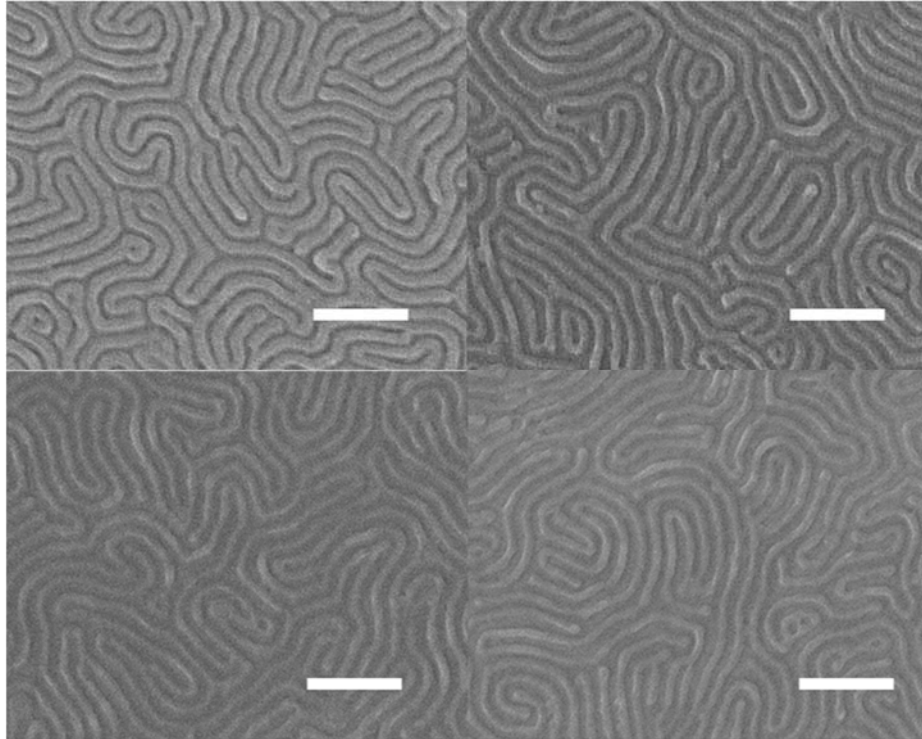


**Figure 4.8. SEM image of GNR with different linewidth**

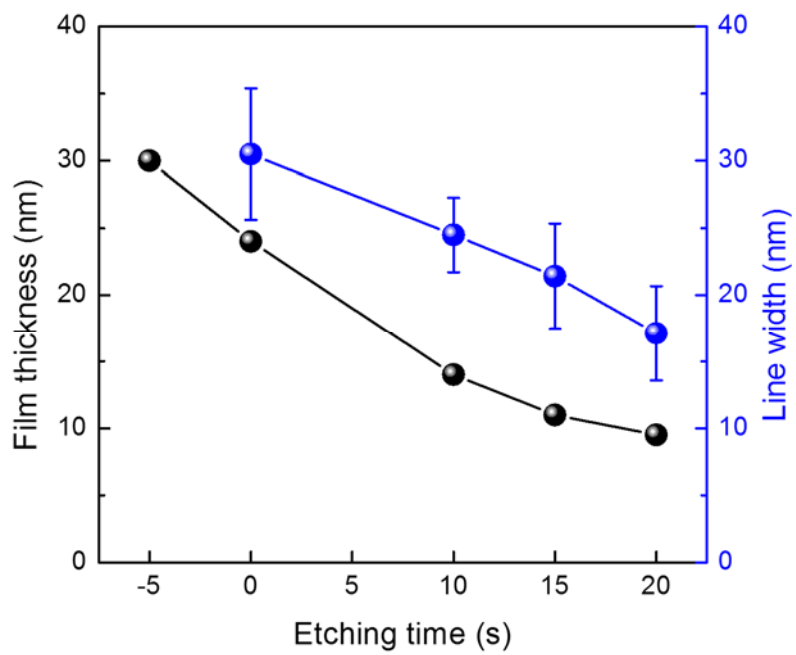


**Figure 4.9. Film thickness and line width versus etching time**

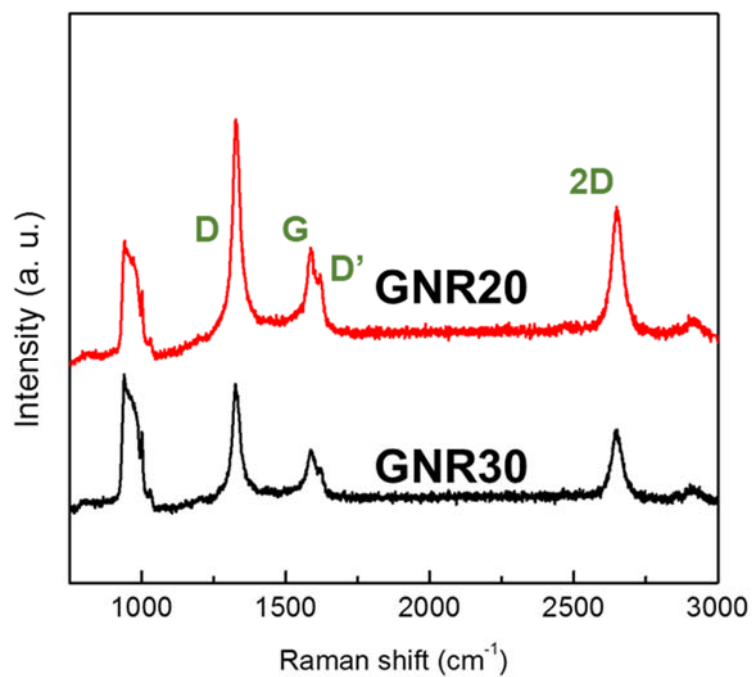


**Figure 4.10. Raman spectroscopy of GNR with different etching time**

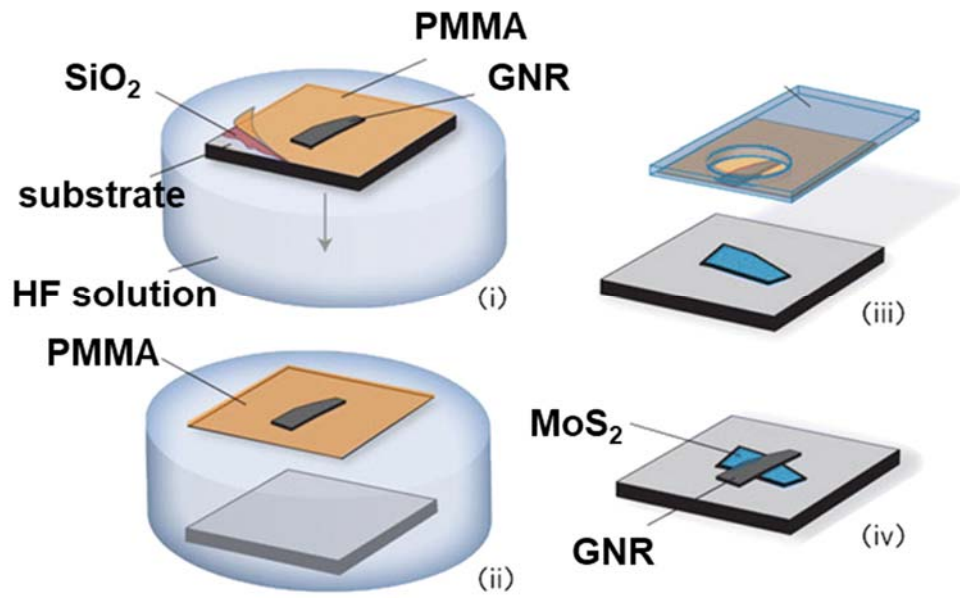


Figure 4.11. Schematic image of preparing GNR/MoS<sub>2</sub> heterostructure

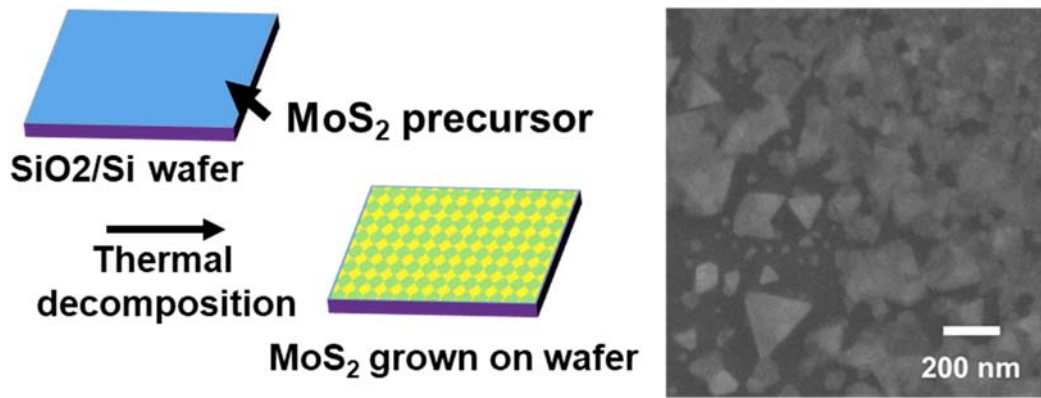


Figure 4.12. Schematic image of preparing MoS<sub>2</sub> and SEM image of MoS<sub>2</sub> on substrate.

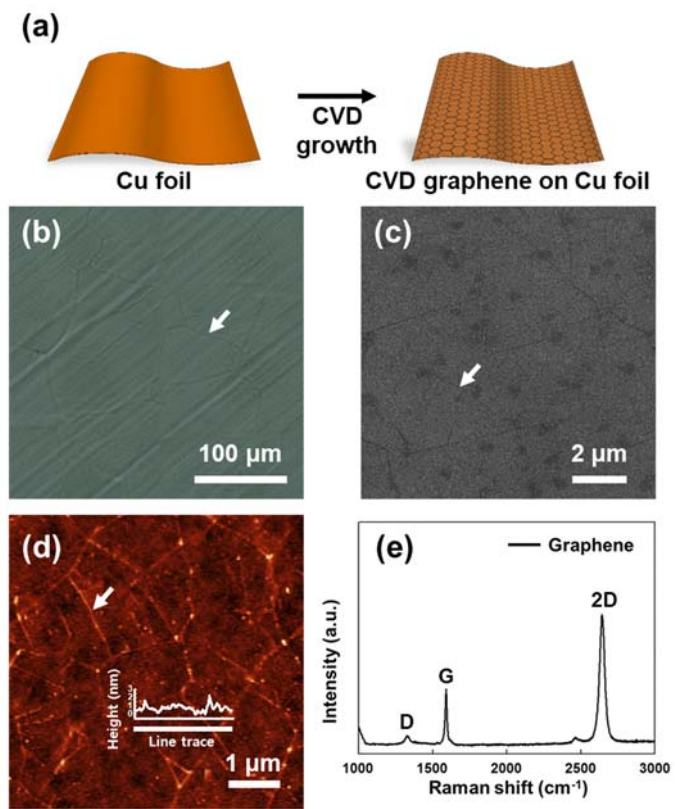


Figure 4.13. Basic properties of CVD graphene.

## **Chapter 5**

# **Coaxial Struts and Microfractured Structures of Compressible Thermoelectric Foams for Self-powered Pressure Sensors**

## 5.1. Introduction

Increasing data communication from machine to machine, from machine to human and from human to human requires a means of collecting data from various sensors. One of the most important sensors for humans is the pressure sensor that provides information on various systems, including blood pressure[1], heart rate[2] and respiration rate[3]. Ideally, wearable sensors would be especially selective in response to specific stimuli and offer the flexibility and stretchability[4] to accommodate mechanical deformation of the skin[5]–[12]. Wearable sensors that adhere to the body or are implanted in the skin are currently limited by power problems, including frequent recharging and battery replacement. To address this issue, small-scale energy-harvesting technologies that convert the body's energy into electrical energy[13] have been developed based on triboelectric[14], [15], mechanoelectric[16], [17], piezoelectric[18]–[21], and thermoelectric[22]–[24] effects.

There has been great interest in thermoelectric generation systems for energy harvesting from human heat based on the Seebeck effect, in which a temperature gradient is converted into electrical energy. Several studies have demonstrated flexible and wearable thermoelectric generators (TEGs) for body heat harvesting using conventional rigid semiconductor TE materials; however, these materials are

limited in their use and form for wearable devices[25]–[27]. Recently, conducting polymers have been studied as flexible TEG materials[28], [29]. Conducting polymers have moderate Seebeck coefficients, high electrical conductivities, and low thermal conductivities; these properties are conducive to high thermoelectric performance[28], [30]. Due to their low toxicity and ease of processing with various coating or printing technologies, conducting polymers are well suited for next-generation devices, offering a low cost, low power consumption, and good flexibility[5], [22], [27]. Poly(3,4-ethylenedioxythiophene) (PEDOT) is one of the most conductive polymers; thus, PEDOT-based TE materials have been widely studied for improved thermoelectric properties, and can be tuned via doping concentration or epitaxial-assisted crystallinity[10], [30], [31].

Foam, a three-dimensional (3D) cellular material with open cells, is made up of an interconnected network of solid struts that form the edges of cells. The cellular microstructure has a porous morphology; this allows for the absorption of other materials[32]–[34], while offering the advantages of low-density[32], [33], structural compressibility[6], [32], [33], and elasticity[32], [33]. Moreover, by infiltrating the foam with conductive materials such as graphene[6], [35], carbon nanotubes[36], or conducting polymers[37], 3D structures with electrical conductivity can be prepared easily. Therefore, many approaches for highly sensitive piezo-resistive-type pressure sensors have been studied in preparation for

the development of conductive cellular structures, such as conductive foams from neat conductive materials[9], [37], [38], elastic polymers/conductive materials composites[5], [39]–[41], and coating of a polymer sponge with conductive materials[6], [35]. Recently, thermoelectric and piezo-resistive characteristics-based temperature–pressure dual sensors from PEDOT:poly(styrenesulfonate) (PSS) on deformable microstructure frames (D. Zhu et al.)[9], and aerogel structures of PEDOT:PSS with elastomeric cross-linkers (X. Crispin et al.)[37], [38] have been reported; these sensors exhibit highly sensitive, independent measurements of pressure and temperature without crosstalk. However, PEDOT:PSS is a brittle material due to the high content of conjugated functional groups and crystallization, which are not suitable for sensors that undergo repeated stretching and compression. To maintain mechanical elasticity and long-term stability as a piezo-resistive-type pressure sensor, only a limited amount of brittle PEDOT:PSS coating can be applied to a porous sensor structure, thereby limiting energy production[5], [38]. Thus, the sensitivity of pressure sensors and the energy production of thermoelectric materials are in conflict with one another; a new structural approach is required to maintain the advantages of the incorporated sensor materials.

In this article, we propose a coaxial strut structure of poly(styrene-ethylene/butylene-styrene)(SEBS)-PEDOT:PSS-melamine foam (SPM) with a

partially fractured microstructure to create an energy-efficient, highly sensitive self-powered pressure sensor. Conventional melamine foam (MF) has a micro-sized cellular structure that acts as a compressible and elastic core framework. The intermediate PEDOT:PSS layer is an active material with thermoelectric properties and high electrical conductivity. A rubbery block copolymer, SEBS, is used for the outer shells due to its superior mechanical elasticity; SEBS also protects the brittle PEDOT:PSS layer, this stabilizing the mechanical properties of the coaxial foam even with a relatively thick PEDOT:PSS layer that generates more thermoelectric power and has high electrical conductivity. Given that the thick PEDOT:PSS is relatively insensitive to pressure changes, the coaxial foam is compressed to 1/20 to induce partial microfractures of the PEDOT:PSS in the SEBS shell only. This serves to maintain high thermoelectric performance and electrical conductivity, but also greatly enhances pressure sensitivity. In this study, the coaxial foam was assembled as a wearable TEG. Our wearable prototype generated 338 nW when attached to the forearm in an external environment; pressure readings ranged from 1 to 28 kPa, with a fast response and long-term stability over more than 10,000 cycles of pressure loading and unloading. We also demonstrated proof-of-concept of a self-powered pressure sensor without external power supply.

## **5.2. Experimental**

### **Preparation of PM and SPM foams**

Highly conductive PEDOT:PSS (Sigma Aldrich, highly conductive grade) 3-4 wt% solution was infiltrated into melamine foam (BASF, Basotech®) and dried at 60 °C for 6 hours. The infiltration process was repeated from 1 to 5 times to prepare PM1 to PM5. To prepare SPM, the PM was immersed in SEBS solution (1 wt%, THF) for 1 hours and dried at 60 °C in vacuum. To improve the sensitivity to the pressure, each cell was compressed for 5% of thickness for original thickness to induce micro-fractures of PEDOT:PSS on melamine struts.

### **Characterization of Thermoelectric Properties of PM and SPM**

The thermal conductivity and Seebeck coefficient were measured as prepared pristine foam, and to measure electrical conductivity, a copper foil was pasted on the bottom and the top of PM and SPM by silver paste as electrode. Thermal conductivity of cubic foam was measured by TCi thermal conductivity measurement system (C-Therm Technologies Ltd.). For measurement of the through plane electrical conductivity of foam, copper foil was attached to the foam

on opposite faces and measured the resistance of the foam using Keithley 2000 multimeter. The electrical conductivity, the thermal conductivity and the thermopower of the SPM1 to SPM5 were measured along the in-plane direction. The thermopower and electrical conductivity of the SPM were measured by a TEP-600 (Seepel Instrument, Korea) thermoelectric measurement instrument.

### **Fabrication of Wearable Thermoelectric Generator**

21 cells of SPM5 with copper electrode on the top and the bottom of the foam were prepared for wearable thermoelectric generator. The SPMs were connected in series by electric copper wire with silver paste. Assembled TEG was dried at 60 °C in vacuum oven for 12 hours. For wearable TEG application, SEBS film was used as a soft and stretchable substrate. SEBS pellet (Kraton, G1657) was pressed at 120 °C for 10 min. to prepare ~200 μm. The SEBS shows sticky characteristics, and two SEBS films can be attached on both sides with physical pressure. The SPM-based TEG covered with SEBS was applied to forearm to measure the electricity from human heat. The measurement on the forearm was executed at external condition (0 °C, approximate 20% humidity) without any cooling materials. To measure the output power as a function of temperature gradient, the SPM-based TEG was placed to the home-built thermoelectric measurement system. The peltier

pads for cooling and heating were placed to the top and make the temperature difference to 10 K to 20 K. The output voltage and current were measured by Kithley 2400 multimeter and the output power was calculated from these values. The output power per weight of the device was also calculated by dividing the output power by total weight of the active materials.

### **Pressure Test of SPM Foam**

Single cell of PM and SPM with the size of  $1 \times 1 \times 0.5 \text{ cm}^3$  were prepared for pressure measuring test. Figure 5.16 shows a high-cycle pressure sensitivity testing system consisting of an electric-dynamic type actuator, a power amplifier and a load cell[42]. Strain gage-based load cells have a capacity of 50 N. To amplify the output signal of the load cell, an analog amplifier (Instrument Division Co., Model 2210) was used. The electro-dynamic type actuator based on the speaker principle includes a field magnet and a moving bobbin with a coil. We used the PXI module (National Instrument<sup>TM</sup>) which consists of PXI-8106 embedded controller for system control and data processing, and PXI-6221 for signal acquisition of load-cell and force sensor. The applied force was converted into pressure with material dimension. Relative resistance variation ( $R/R_0$ ) as a function of pressure was measured with very low frequency of 0.1 Hz. The response and recovery test with

square wave of deformation was applied was done with frequency of 0.1 Hz. Over 10000 times of cyclic test of loading and unloading pressure of 4.4 kPa was done with high frequency of 10 Hz.

### **Self-Powered Pressure Sensor Test**

9 cells of SPM5 were connected in series for self-powered pressure sensor. Home-built thermoelectric measurement system was used to realize the continuous temperature gradient and Keithley 2400 was connected to the SPM based TEG directly to measure the thermoelectric current for pressure test. The pressure was applied to the top of the TEG and the changes of the current was recorded. While the pressure test was done, the temperature difference along the TEG was kept to  $\Delta T = 50$  K. The thermoelectric current was recorded as shown in the multimeter.

### 5.3. Results and Discussion

Figure 5.1 shows a schematic diagram of the coaxial strut preparation process of the 3D cellular open-cell structure with partial microfractures. MF, having a cellular structure (figure 5.2a) with a  $\sim 140$   $\mu\text{m}$  pore size and a  $5$ - $\mu\text{m}$  strut width shows highly compressible properties and high water uptake to pores. PEDOT:PSS-melamine (PM) foam was prepared by simply infiltrating the MF with PEDOT:PSS. MF was immersed in a 4 wt% of PEDOT:PSS aqueous solution and dried at  $60^\circ\text{C}$  for 5 h. To enhance thermoelectric power generation, the amount of PEDOT:PSS increased with subsequent infiltrations. This process was repeated one to five times to prepare PM1–PM5 samples. The PEDOT:PSS coating layer on melamine struts (figure 5.2b) forms conductive paths through the interconnected 3D cellular open-cell structure. With repeated PEDOT:PSS coatings, the strut widths increased linearly around  $1$   $\mu\text{m}/\text{time}$ , as shown in figure 5.8. However, the brittle nature of the PEDOT:PSS, and lack of a specific interaction between PEDOT:PSS and MF, causes the PEDOT:PSS particles to break away from the MF skeleton under repetitive mechanical deformation, as shown in figure 5.9. For structural stability, even under high loading conditions of PEDOT:PSS, a highly elastic SEBS shell was introduced to PM struts. The PM foam was also simply immersed into a SEBS solution in THF and dried at  $60^\circ\text{C}$  for 12 h. The prepared coaxial SPM maintained

its cellular structure; figure 5.2c shows a scanning electron microscopy (SEM) image of the thin SEBS outer shell. MF, PM, and SPM exhibited very low densities of 0.0078, 0.026–0.18, and 0.089–0.27 g cm<sup>-3</sup>, respectively. Foams of size 1 × 1 × 0.5 cm<sup>3</sup> were used in the TEG module and pressure sensor assemblies.

To enhance pressure sensitivity, a microfractured structure was adopted for the conductive material[6]. We strongly compressed PM and SPM foams to 1/20 to induce partial fracture of PEDOT:PSS. In the case of PM, the brittle PEDOT:PSS coating layer was broken by strong mechanical deformation, resulting in the fragmentation and delamination of large PEDOT:PSS particles from the melamine structure (figure 5.9a-b). In contrast, with SPM, partial microfracture of PEDOT:PSS occurred only within the protective SEBS outer shell, leaving PEDOT:PSS fragments in the shell.

Especially, it can be seen that the SEBS shell keeps the connecting paths well even in the part where the strut breaks due to the large pressure. (figure 5.9c-d). The fragments in the shells served to reconnect electrical conduction paths in accordance with the mechanical deformation; therefore, the resulting structure retained a high electrical conductivity and was sensitive to changes in resistance.

Figure 5.3 shows the electrical and thermoelectric properties of PM and SPM cells with different repeated times of PEDOT:PSS infiltration. As the infiltration amount increased, the thickness of the PEDOT:PSS layer increased from 7 to 10

$\mu\text{m}$  (figure 5.8). Thus, the electrical resistivity of PM decreased as a function of PEDOT:PSS infiltration, as shown in figure 5.3. The electrical resistivity of SPM was slightly higher as SEBS partially penetrated into the PEDOT:PSS conductive path; however, the resistivity of SPM remained low and decreased with subsequent infiltrations. The resistivity of SPM5 was only  $0.61 \pm 0.279 \Omega \text{ cm}^{-1}$ , which is sufficiently low for thermoelectric generation. The thermopower, electrical conductivity, and thermal conductivity of SPM were measured with respect to the number of PEDOT:PSS infiltration iterations. The thermopower of SPM remained in the range of 13.3 to 14.4  $\mu\text{V K}^{-1}$ , regardless of the number of infiltrations, in agreement with the thermopower readings of spin-coated PEDOT:PSS thin film. On the other hand, the electrical and thermal conductivities increased linearly as a function of PEDOT:PSS infiltration time due to thicker conductive layers. The electrical conductivities of SPMs increased up to  $6 \text{ S cm}^{-1}$ , which is a fairly high value among highly porous cellular structures of conductor materials. The thermal conductivities of SPMs remained lower than  $0.066 \text{ W m}^{-1} \text{ K}^{-1}$ , which is five times lower than that of PEDOT:PSS thin film ( $0.31 \text{ W m}^{-1} \text{ K}^{-1}$ )[43], even after five iterations of PEDOT:PSS infiltration, owing to their porous structures.

The low thermal conductivity of SPM maintained the thermal gradient of the heat source and heat sink, thus allowing it to generate electricity for a long period of time. Due to the isotropic porous structure of MF, we observed similar values in

electrical conductivity, thermal conductivity, and thermopower, regardless of the measurement direction, as shown in figure 5.10.

For thermoelectric generation,  $1 \times 1 \times 0.5 \text{ cm}^3$ -sized SPM foam was prepared. The SPM5 single cell exhibited 0.4 mV with a 30 K vertical temperature gradient (figure 5.4), a reasonable value ( $\sim 13.3 \text{ } \mu\text{V/K}$ ) compared with the measured thermopowers of conventional Seebeck measuring instruments (figure 5.3b). Twenty-one SPM5 cells were connected in series for thermoelectric generation (figure 5.4b); the total electrical resistance of the TEG from these SPM5 cells was  $\sim 22 \text{ } \Omega$ , which indicates that the contact resistance between the electrode and the foam of our TEG was negligible. Two 200- $\mu\text{m}$  SEBS films were attached to both sides of our assembled TEGs for optimal adhesion/contact. In the proof-of-concept of wearable TEGs, a high thermoelectric voltage of 2.6 mV was maintained for a considerable period of time in an external environment when worn on the forearm (figure 5.4c); this performance was attributed to the low thermal conductivity of our TEG prototype. The output power density of the TEG of SPM5 was measured with a fixed temperature gradient (figure 5.4d); the maximum output power at  $\Delta T = 20 \text{ K}$  was 338 nW from our TEG, and 448.7 nW/g with 21 SPM5 cells. The SPM also can be compressed with lateral direction (figure 5.11). And the foam can recover the original shape by releasing external stress, meaning that the foam can fit the body to gather thermal energy from the rough surface. Laterally compressed

foam also has compressibility with vertically applied pressure (figure 5.11d-f)

A thermoelectric sponge was also applied to the pressure sensing material, as shown in Fig. 5. S-H Yu et al.[6] demonstrated that pre-strained foam that induces the breakage of the conductive backbone has high pressure sensitivity. A pre-strain method for high sensitivity was applied to our PM and SPM foams to induce the microfractured structure of PEDOT:PSS layers without and with the SEBS outer shells. Figure 5a and b shows the resistance changes of PM and SPM foams before and after 95% compression with repeated pressure loading (6 kPa) and unloading. Pristine PM foam was sensitive to changes in resistance with pressure change, but also showed a gradual increase in resistance with repeated testing, due to the externally exposed conductive paths of brittle PEDOT:PSS (figure 5.9). In contrast, pristine SPM with SEBS shells, as protective layers, exhibited reliable resistance behavior with repeated pressure testing. After 95% compression, PM did not recover to its original thickness and their relative resistance  $R/R_0$  decreased, while compressed SPM recovered its original thickness within a short time owing to the rubbery SEBS outer shells and the  $R/R_0$  of SPM foam increased due to occurring microfractures. When additional strong compression was applied to the compressed SPM, the resistance shows no more significant changes. Therefore, the resistance of compressed PM did not change under additional pressure, as the conductive paths were stuck together before and after loading compression, whereas the resistance

of compressed SPM was more sensitive to pressure changes up to 1.7 times and showed a stable response. Digital images of PM1 and SPM1, before and after compression, are shown in figure 5.12. Figure 5.5c-f shows the resistance and  $R/R_0$  changes of PM1, PM5, SPM1, and SPM5 after compression. Given that the resistance of SPM1 with a thin PEDOT:PSS layer was higher than that of SPM5, SPM1 was more sensitive than SPM5, with a  $R/R_0$  change of about 1.5 times larger at the same pressure.

Figure 5.6 shows the resistance behavior with pressure loading. Pressures up to 30 kPa were applied to PM1 and SPM1 samples in figure 5.6a. The resistance of SPM1 changed with the applied pressure along the inverse curve down to  $\sim 1/10$  of the original resistance, whereas the resistance of PM1 did not change due to the fixed thickness from the pre-press process. Under five cycles of repeated loading and unloading with different pressures, from 4.4 to 25 kPa, SPM1 worked very well as a rapid-response pressure sensor (figure 5.6b). The resistance behavior of SPM3 and SPM5 with 95% compression was also tested with pressure loading (figure 5.13). The change in relative resistance of SPM3 and SPM5 under pressure is restricted as SPM3 and SPM5 have higher modulus compared with SPM1. However, SPM3 and SPM5 could bear under higher pressure, which means that higher pressure can be detected with SPM3 and SPM5. To observe the response and recovery behavior of SPM1, resistance and pressure changes from the load cell in

a single 8-kPa pressure cycle were analyzed over time (figure 5.6c). figure 5.6d and e shows the detailed response and recovery behavior of SPM1. The response time of SPM1 was less than 10 ms when pressure was applied, but stabilization time was 97 ms because of an overshooting in given force. The SPM1 pressure sensor followed the same trend as that of the applied force trace, showing highly sensitive and agile sensor performance. Because the SEBS shell helps the foam to recover its original shape, the recovery time of the relative resistance was also less than 10 ms; however, additional time around 56 ms was needed to stabilize the resistance readings due to residual vibrations. The resistance difference versus time for (figure 5.14a-c) SPM3 and (figure 5.14d-f) SPM5 with 35 kPa for the observation of response and recovery behaviors. The response time of SPM3 and SPM5 was only a few ms when the pressure was applied, however, the stabilization time was about 100 ms because of an overshooting in given force. The blue line displaying the given force read by load cells and the red line showing the relative resistance of SPMs show the same tendency with given pressure. The green dotted line shows the peak of relative resistance and pressure read by load cell, and the gap of two lines is narrower than 5 ms. The response and recovery behaviour of SPM3 and SPM5 was tested by loading and unloading pressure of 30 to 40 kPa (figure 5.14). The response and recovery behaviours show same tendency with varied conductive wall thickness. The repeated test loading and unloading pressure of 4.4 kPa was

executed for over 10,000 cycles at 10 Hz, as shown in Fig. 6f. Even under repetitive pressure loadings at high frequency, the SPM1 foam exhibited reliable and stable pressure-sensing performance.

The SPM foam with high thermoelectric and piezo-resistive pressure-sensing properties was applied in a proof-of-concept, self-powered pressure sensor system with temperature variation, as shown in figure 5.7a. The temperature gradient was applied to the SPM-based TEG without loading pressure, and the thermoelectric current was measured with a Keithley 2400 multimeter as  $\sim 170 \mu\text{A}$  at  $\Delta T = 50 \text{ K}$ . We repeatedly applied pressure to the SPM-based TEG and measured the thermoelectric current with a pressure load under a constant temperature difference. The thermoelectrical current ratio ( $I/I_0$ ) of the SPM-based TEG with repeated loading and unloading of pressure (17 kPa and 24 kPa) is shown in figure 5.7b. We confirmed that thermoelectric current changes of the SPM foam according to the applied pressure can be detected without the need for any external power source, with the exception of the measuring instruments. We also varied the temperature gradient from -20 K to 20 K to establish the effect of the temperature different between the surface and the environment. Figure 5.15 shows the measured I-V curve with different pressure and temperature gradient. The thermoelectric current is changed under pressure at the same temperature gradient. And the slope of the I-V curve keeps constant under different temperature gradient meaning that the

resistance does not change with varied temperature.

## 5.4. Conclusion

We developed a coaxial SEBS/PEDOT:PSS/MF structure for a self-powered pressure sensor based on the thermoelectric effect and piezo-resistive properties. Our device configuration has the structural benefit of a coaxial SPM structure for better fit to the human body. A thermoelectric voltage of 2.6 mV could be generated on human skin. Additionally, the SEBS shell protects the brittle PEDOT:PSS layer on the melamine strut from repetitive mechanical deformation and maintains stable performance with higher PEDOT:PSS content. Furthermore, partial microfracture of the PEDOT:PSS in the SEBS shell only significantly enhanced the pressure sensitivity, while maintaining high conductivity and thermoelectric performance. For pressure sensor applications, the SPM showed superior pressure-sensitive characteristics with microfractured coaxial struts; the response and recovery times of SPM less than 10 ms, with 8 kPa of applied pressure. The long-term stability of the SPM pressure sensor was confirmed from stable output signals over 10,000 cycles of repeated pressure loading/unloading. The SPM-based TEG was also applied to a proof-of-concept self-powered pressure sensor based on thermoelectricity and piezo-resistivity. A coaxial structure for a 3D cellular conductor-based pressure sensor that additionally can generate energy from waste heat is a promising platform for manufacturing stably deformable materials for

long-term operation of self-powered wearable devices. Moreover, compressed SPM shows higher electrical conductivity with narrower cover area which make the thermoelectric generator more efficient. This coaxial cellular platform can be applied to various types of self-powered pressure sensors and energy harvesting devices and, more generally, could serve as an ideal structure for various deformable devices in future applications such as passive radio-frequency identification.

## 5.5. References

- [1] Y. Lee et al., “Flexible Ferroelectric Sensors with Ultrahigh Pressure Sensitivity and Linear Response over Exceptionally Broad Pressure Range,” *ACS Nano*, vol. 12, pp. 4045–4054, 2018.
- [2] S. Gong et al., “A wearable and highly sensitive pressure sensor with ultrathin gold nanowires,” *Nat. Commun.*, vol. 5, pp. 1–8, 2014.
- [3] J. Park et al., “Tailoring force sensitivity and selectivity by microstructure engineering of multidirectional electronic skins,” *NPG Asia Mater.*, pp. 1–14, 2018.
- [4] E. Bilotti, R. Zhang, H. Deng, M. Baxendale, and T. Peijs, “Fabrication and property prediction of conductive and strain sensing TPU/CNT nanocomposite fibres,” *J. Mater. Chem.*, vol. 20, no. 42, p. 9449, 2010.
- [5] P. J. Taroni et al., “Toward Stretchable Self-Powered Sensors Based on the Thermoelectric Response of PEDOT:PSS/Polyurethane Blends,” *Adv. Funct. Mater.*, vol. 28, no. 15, p. 1704285, 2018.
- [6] H. Bin Yao et al., “A flexible and highly pressure-sensitive graphene-polyurethane sponge based on fractured microstructure design,” *Adv. Mater.*, vol. 25, no. 46, pp. 6692–6698, 2013.
- [7] H. Cheng et al., “Flexible cellulose-based thermoelectric sponge towards

wearable pressure sensor and energy harvesting,” *Chem. Eng. J.*, vol. 338, no. September 2017, pp. 1–7, 2018.

[8] T. Someya et al., “Conformable , flexible , large-area networks of pressure and thermal sensors with organic transistor active matrixes,” *PNAS*, vol. 102, no. 35, pp. 12321–12325, 2005.

[9] F. Zhang, Y. Zang, D. Huang, C. Di, and D. Zhu, “Flexible and self-powered temperature–pressure dual-parameter sensors using microstructure-frame-supported organic thermoelectric materials,” *Nat. Commun.*, vol. 6, no. May, pp. 1–10, 2015.

[10] Y. H. Lee, J. Oh, S. S. Lee, H. Kim, and J. G. Son, “Highly Ordered Nanoconfinement Effect from Evaporation-Induced Self-Assembly of Block Copolymers on In Situ Polymerized PEDOT:Tos,” *ACS Macro Lett.*, vol. 6, no. 4, pp. 386–392, 2017.

[11] J. Ge et al., “A Stretchable Electronic Fabric Artificial Skin with Pressure-, Lateral Strain-, and Flexion-Sensitive Properties,” *Adv. Mater.*, vol. 28, no. 4, pp. 722–728, 2016.

[12] S. Y. Kim, E. Jee, J. S. Kim, and D. H. Kim, “Conformable and ionic textiles using sheath-core carbon nanotube microyarns for highly sensitive and reliable pressure sensors,” *RSC Adv.*, vol. 7, pp. 23820–23826, 2017.

- [13] J. A. Paradiso, "Energy Scavenging for Mobile and Wireless Electronics Electronics," *IEEE Pervasive Comput.*, vol. 4, no. 1, pp. 18–27, 2005.
- [14] G. Zhu et al., "Toward Large-Scale Energy Harvesting by a Nanoparticle-Enhanced Triboelectric Nanogenerator," *Nano Lett.*, vol. 13, pp. 847–853, 2013.
- [15] S. Yang, J. Chen, X. Bei, G. Zhu, and Z. Lin, "Two-dimensional rotary triboelectric nanogenerator as a portable and wearable power source for electronics," *Nano Energy*, vol. 17, pp. 10–16, 2015.
- [16] R. Riemer et al., "Biomechanical energy harvesting from human motion: theory, state of the art, design guidelines, and future directions," *J. Neuroeng. Rehabil.*, vol. 8, no. 1, p. 22, 2011.
- [17] P. Niu, P. Chapman, R. Riemer, and X. Zhang, "Evaluation of motions and actuation methods for biomechanical energy harvesting," *PESC Rec. - IEEE Annu. Power Electron. Spec. Conf.*, vol. 3, pp. 2100–2106, 2004.
- [18] J. Zhao and Z. You, "A Shoe-Embedded Piezoelectric Energy Harvester for Wearable Sensors," *Sensors*, vol. 14, pp. 12497–12510, 2014.
- [19] W. Jung, M. Lee, M. Kang, and H. Gyu, "Powerful curved piezoelectric generator for wearable applications," *Nano Energy*, vol. 13, pp. 174–181, 2015.
- [20] W. Wu, S. Bai, M. Yuan, Y. Qin, Z. L. Wang, and T. Jing, "Lead Zirconate

Titanate Nanowire Textile Nanogenerator for Wearable,” ACS Nano, vol. 6, no. 7, pp. 6231–6235, 2012.

[21] S. Baek et al., “Flexible piezocapacitive sensors based on wrinkled microstructures: toward low-cost fabrication of pressure sensors over large areas,” RSC Adv., vol. 7, no. 63, pp. 39420–39426, 2017.

[22] M. Hyland, H. Hunter, J. Liu, E. Veety, and D. Vashaee, “Wearable thermoelectric generators for human body heat harvesting,” Appl. Energy, vol. 182, pp. 518–524, 2016.

[23] Y. Shi, Y. Wang, D. Mei, B. Feng, and Z. Chen, “Design and Fabrication of Wearable Thermoelectric Generator Device for Heat Harvesting,” Ieee Robot. Autom. Lett., vol. 3, no. 1, pp. 373–378, 2018.

[24] J. Choi et al., “Flexible and Robust Thermoelectric Generators Based on All-Carbon Nanotube Yarn without Metal Electrodes,” ACS Nano, vol. 11, no. 8, pp. 7608–7614, 2017.

[25] J. Bahk, H. Fang, and A. Shakouri, “Flexible thermoelectric materials and device optimization for wearable energy harvesting,” J. Mater. Chem. C, vol. 3, pp. 10362–10374, 2015.

[26] S. J. Kim, J. H. We, and B. J. Cho, “A wearable thermoelectric generator

fabricated on a glass fabric,” *Energy Environ. Sci.*, vol. 7, pp. 1959–1965, 2014.

[27] E. Jin Bae, Y. Hun Kang, K.-S. Jang, and S. Yun Cho, “Enhancement of Thermoelectric Properties of PEDOT:PSS and Tellurium-PEDOT:PSS Hybrid Composites by Simple Chemical Treatment,” *Sci. Rep.*, vol. 6, no. 1, p. 18805, 2016.

[28] O. Bubnova and X. Crispin, “Towards polymer-based organic thermoelectric generators,” *Energy Environ. Sci. View*, vol. 5, pp. 9345–9362, 2012.

[29] E. J. Bae, Y. H. Kang, K.-S. Jang, C. Lee, and S. Y. Cho, “Solution synthesis of telluride-based nano-barbell structures coated with PEDOT:PSS for spray-printed thermoelectric generators,” *Nanoscale*, vol. 8, no. 21, pp. 10885–10890, 2016.

[30] O. Bubnova et al., “Optimization of the thermoelectric figure of merit in the conducting polymer poly ( 3 , 4-ethylenedioxythiophene ),” *Nat. Mater.*, vol. 10, no. 6, pp. 429–433, 2011.

[31] W. Lee, Y. H. Kang, J. Y. Lee, K.-S. Jang, and S. Y. Cho, “Improving the thermoelectric power factor of CNT/PEDOT:PSS nanocomposite films by ethylene glycol treatment,” *RSC Adv.*, vol. 6, no. 58, pp. 53339–53344, 2016.

[32] H. Liang, Q. Guan, L. Chen, Z. Zhu, W. Zhang, and S. Yu, “Macroscopic-Scale Template Synthesis of Robust Carbonaceous Nanofiber Hydrogels and

Aerogels and Their Applications,” *Angewandte*, vol. 51, pp. 5101–5105, 2012.

[33] H. Sun, Z. Xu, and C. Gao, “Multifunctional , Ultra-Flyweight , Synergistically Assembled Carbon Aerogels,” *Adv. Mater.*, vol. 25, pp. 2554–2560, 2013.

[34] Y. He et al., “An environmentally friendly method for the fabrication of reduced graphene oxide foam with a super oil absorption capacity,” *J. Hazard. Mater.*, vol. 260, pp. 796–805, 2013.

[35] A. Rinaldi, A. Tamburrano, M. Fortunato, and M. S. Sarto, “A Flexible and Highly Sensitive Pressure Sensor Graphene Nanoplatelets,” *Sensors*, vol. 16, p. 2148, 2016.

[36] Y. Yang, M. C. Gupta, V. Charlottes, K. L. Dudley, and R. W. Lawrence, “Novel Carbon Nanotube – Polystyrene Foam Composites for Electromagnetic Interference Shielding,” *Nano Lett.*, vol. 5, no. 11, pp. 2131–2134, 2005.

[37] Z. U. Khan et al., “Thermoelectric Polymers and their Elastic Aerogels,” *Adv. Mater.*, vol. 28, no. 22, pp. 4556–4562, 2016.

[38] S. Han, F. Jiao, Z. U. Khan, J. Edberg, S. Fabiano, and X. Crispin, “Thermoelectric Polymer Aerogels for Pressure–Temperature Sensing Applications,” *Adv. Funct. Mater.*, vol. 27, no. 44, p. 1703549, 2017.

- [39] B. C. Tee, C. Wang, R. Allen, and Z. Bao, “An electrically and mechanically self-healing composite with pressure- and flexion-sensitive properties for electronic skin applications,” *Nat. Nanotechnol.*, vol. 7, no. DECEMBER, p. 825-, 2012.
- [40] A. Sanli, A. Benchirouf, C. Müller, and O. Kanoun, “Sensors and Actuators A : Physical Piezoresistive performance characterization of strain sensitive multi-walled carbon nanotube-epoxy nanocomposites,” *Sensors Actuators A. Phys.*, vol. 254, pp. 61–68, 2017.
- [41] K. H. Kim, S. K. Hong, N. S. Jang, S. H. Ha, H. W. Lee, and J. M. Kim, “Wearable Resistive Pressure Sensor Based on Highly Flexible Carbon Composite Conductors with Irregular Surface Morphology,” *ACS Appl. Mater. Interfaces*, vol. 9, no. 20, pp. 17499–17507, 2017.
- [42] J. Liu, X. Wang, D. Li, N. E. Coates, R. A. Segalman, and D. G. Cahill, “Thermal conductivity and elastic constants of PEDOT:PSS with high electrical conductivity,” *Macromolecules*, vol. 48, no. 3, pp. 585–591, 2015.
- [43] J. H. Song, Y. S. Shin, and Y. S. Im, “Construction of Small Sized, Electro-Dynamic Type Bending Fatigue Testing Machine,” *Korean KSME Trans. A*, vol. 13, no. 1, pp. 199–203, 1989.

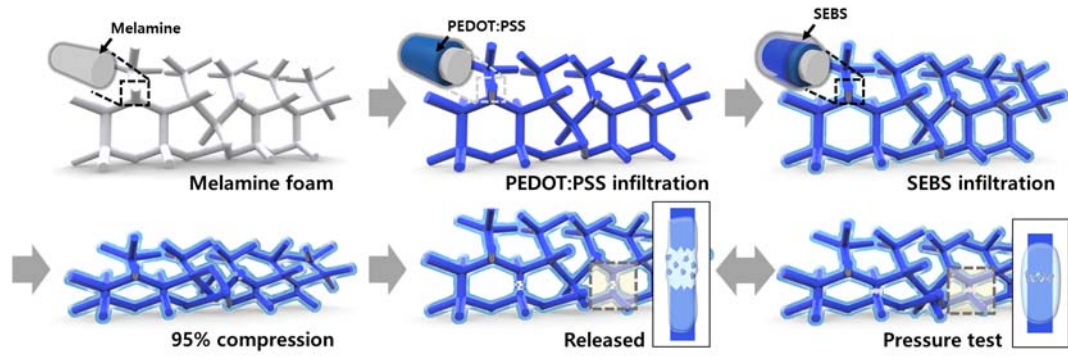


**Figure 5.1. Schematic image of preparing coaxial 3D cellular conductor with micro-fractured morphology**

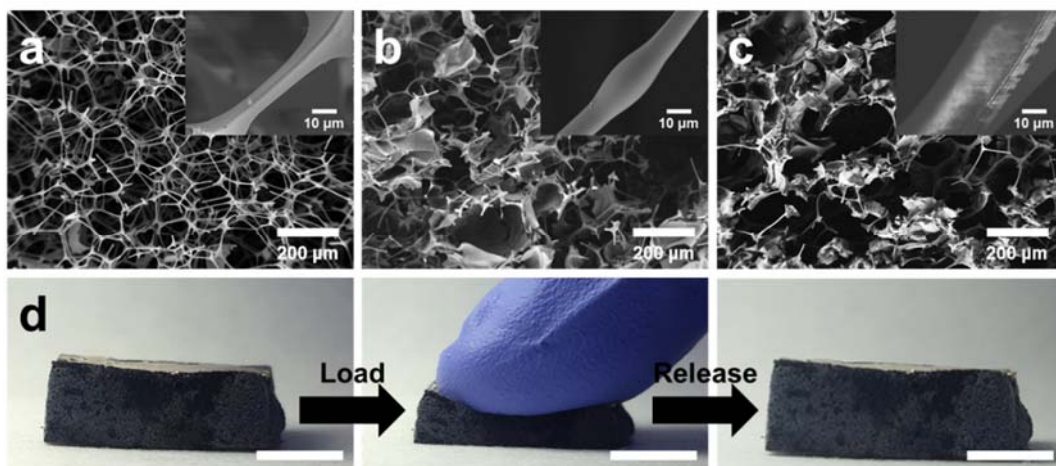


**Figure 5.2.** (a-c) SEM image of melamine foam (MF), PEDOT:PSS infiltrated foam (PM), and PM covered with SEBS (SPM)

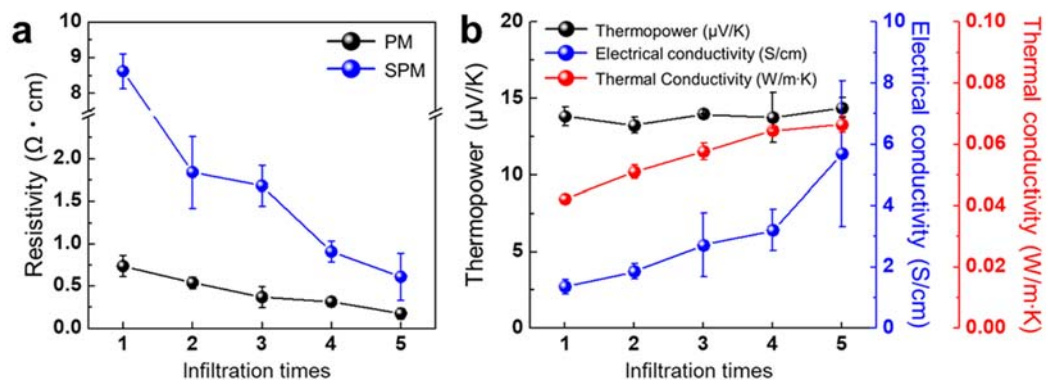


**Figure 5.3. Characteristics of the PEDOT:PSS-melamine (PM) foam and SEBS-PEDOT:PSS-melamine (SPM) foam with differently repetitive PEDOT:PSS infiltration process**

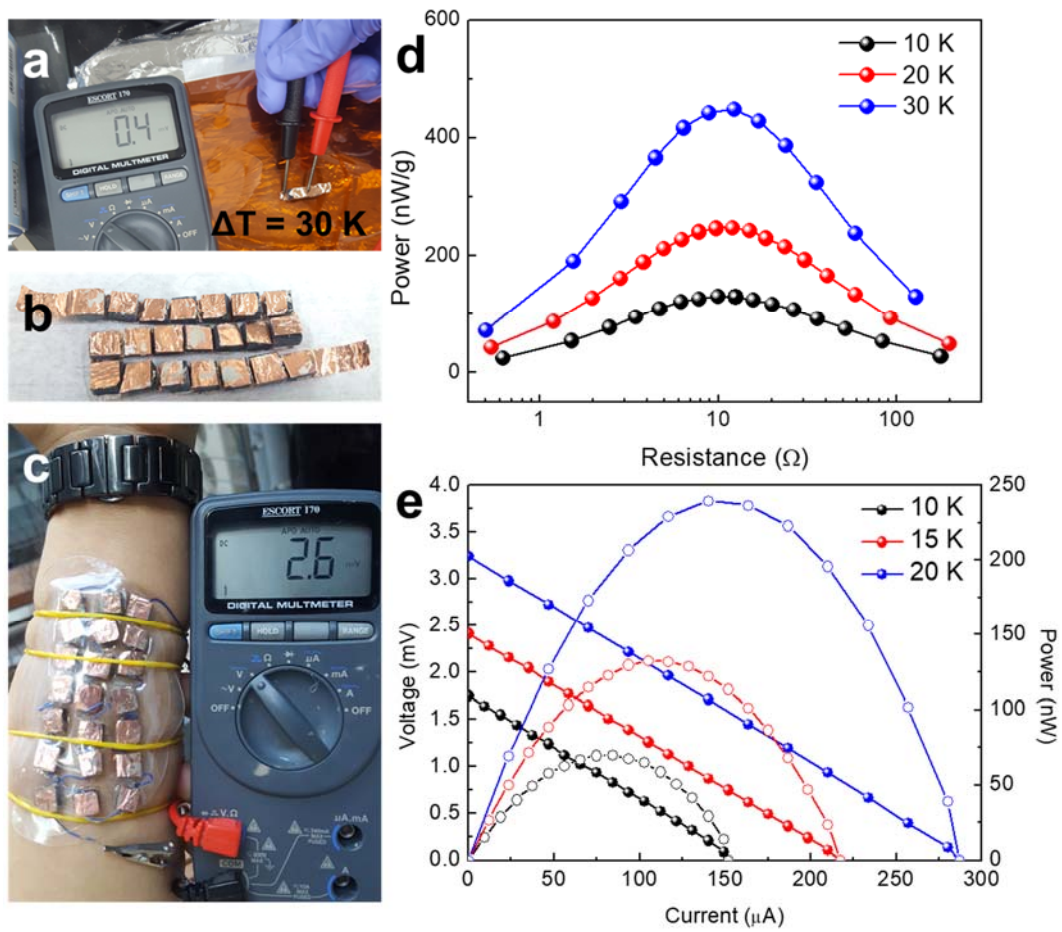
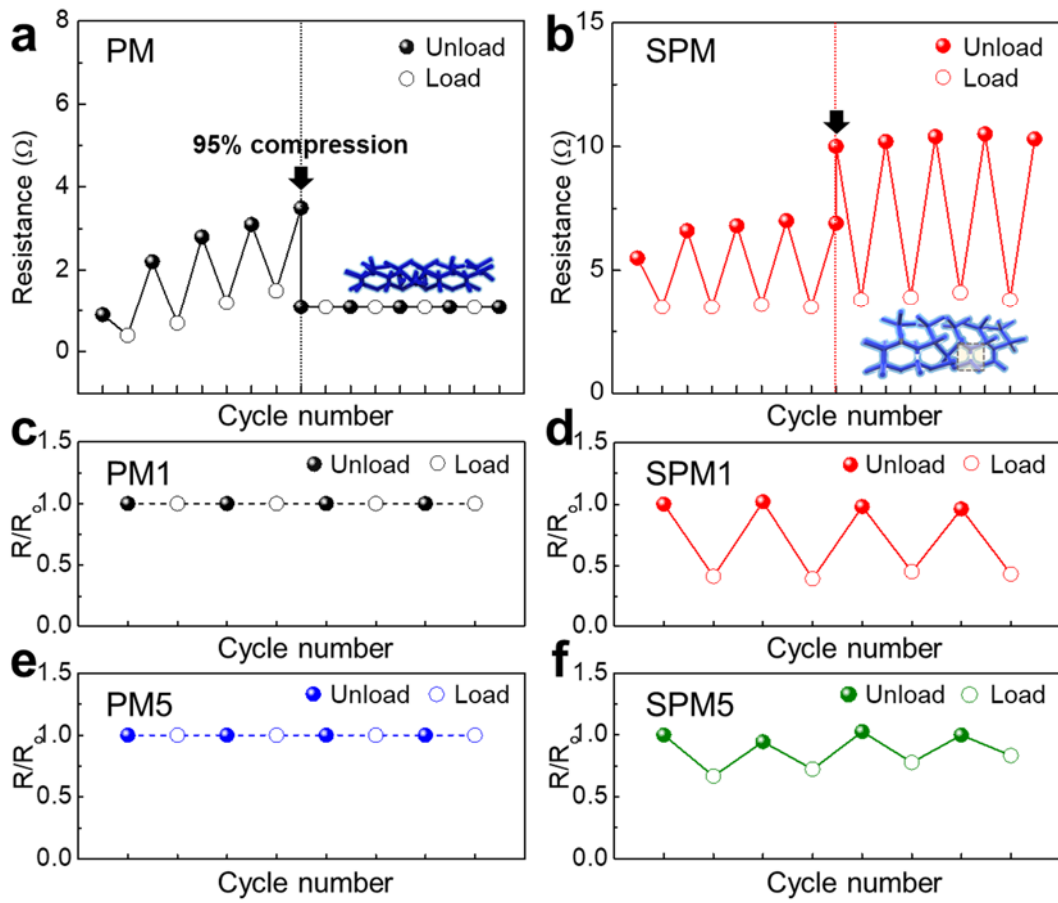
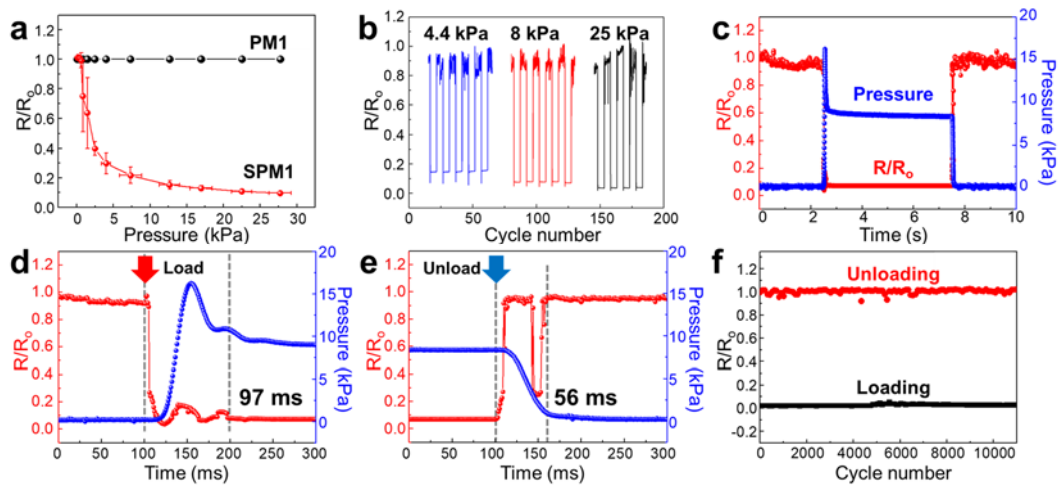


Figure 5.4. Thermoelectric module of SPM5.



**Figure 5.5. Resistance change under pressure of (a) PM and (b) SPM**



**Figure 5.6. Pressure sensing performance of 95% compressed PM and SPM foams**

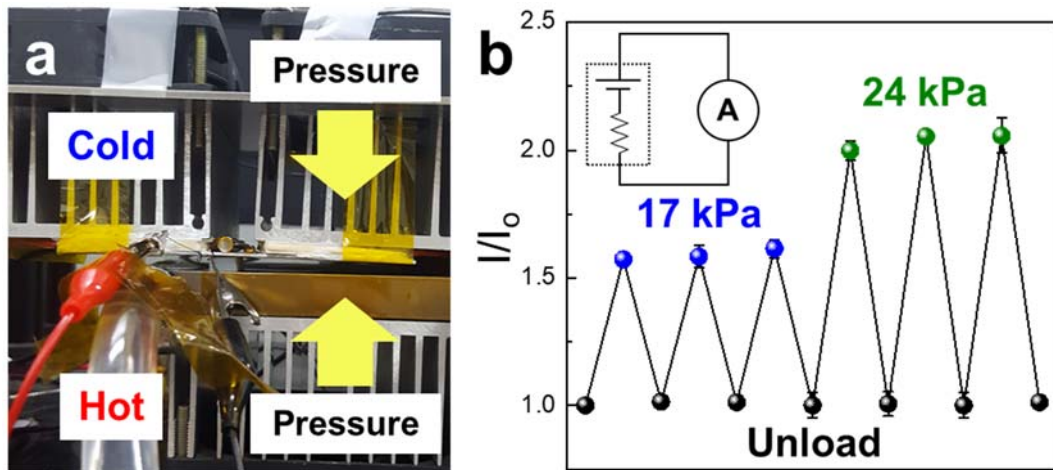
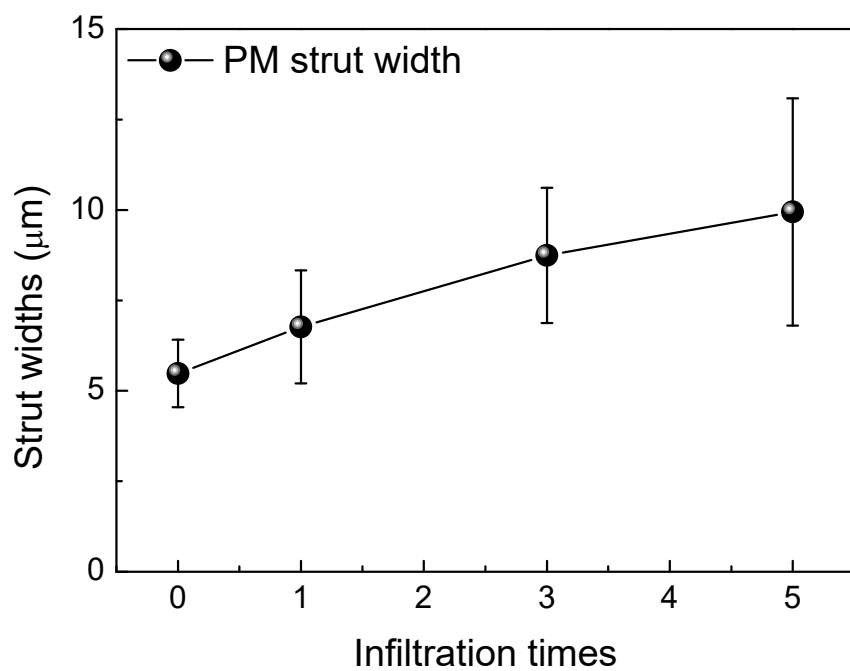
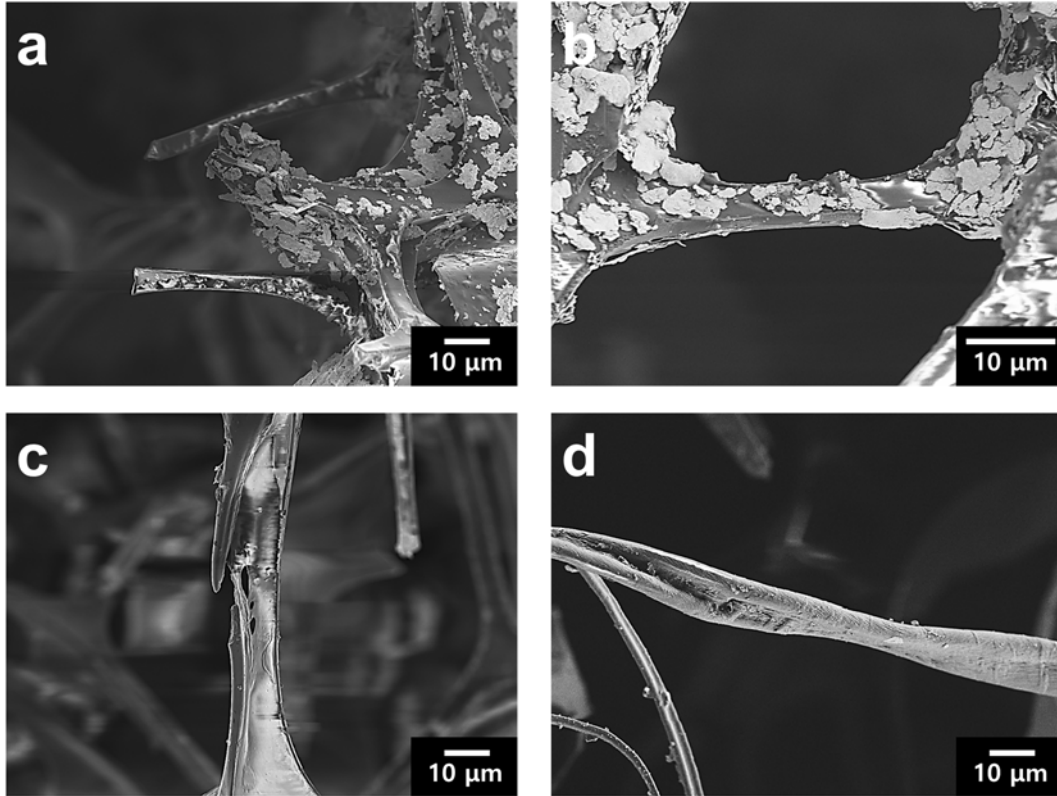


Figure 5.7. (a) Digital image of self-powered pressure sensor test and (b)  $I/I_0$  with repeated pressure loading and unloading test under temperature difference of 50 K.



**Figure 5.8.** The strut widths as a function of PEDOT:PSS infiltration times.



**Figure 5.9. SEM image of PM (a, b) and SPM (c, d) after repeated pressure loading and unloading test.**

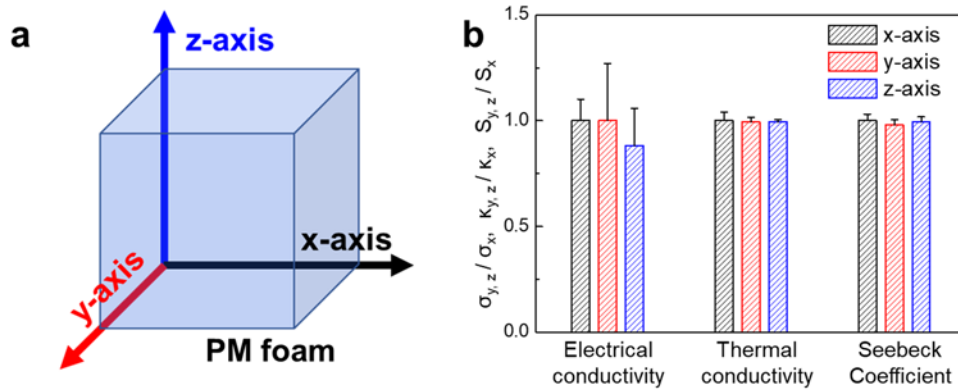


**Figure 5.10. (a) Schematic image of PM foam with measurement direction, (b) relative electrical conductivity, thermal conductivity and Seebeck coefficient against to horizontal direction (x-axis).**

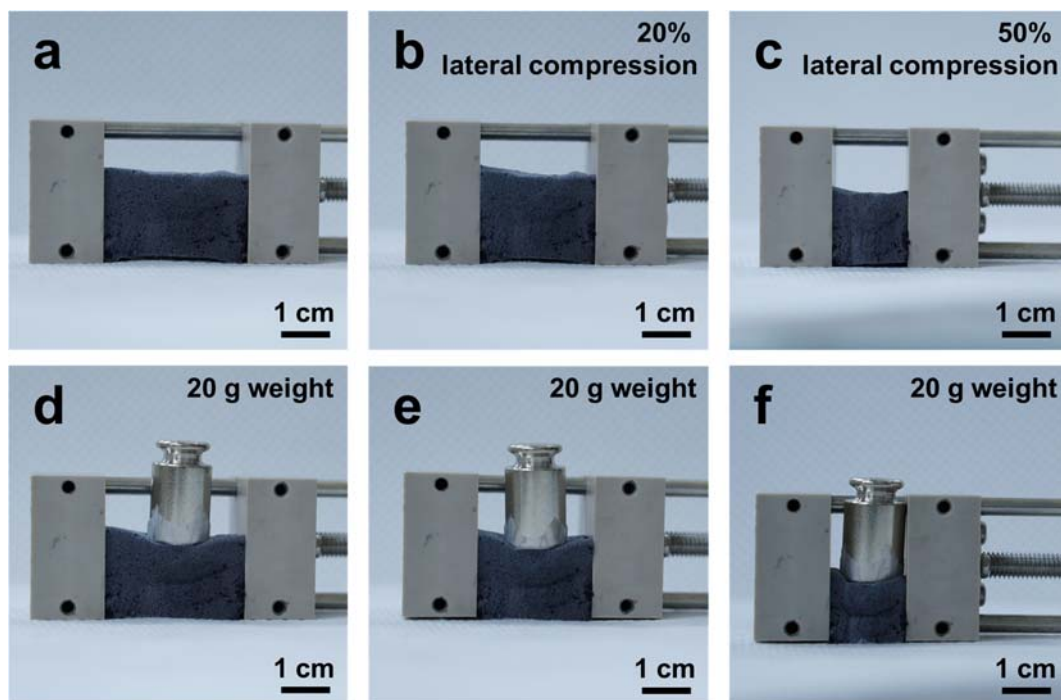


**Figure 5.11. Digital image of SPM1 and laterally compressed SPM1 foam. SPM1 is compressed with external strain machine.**

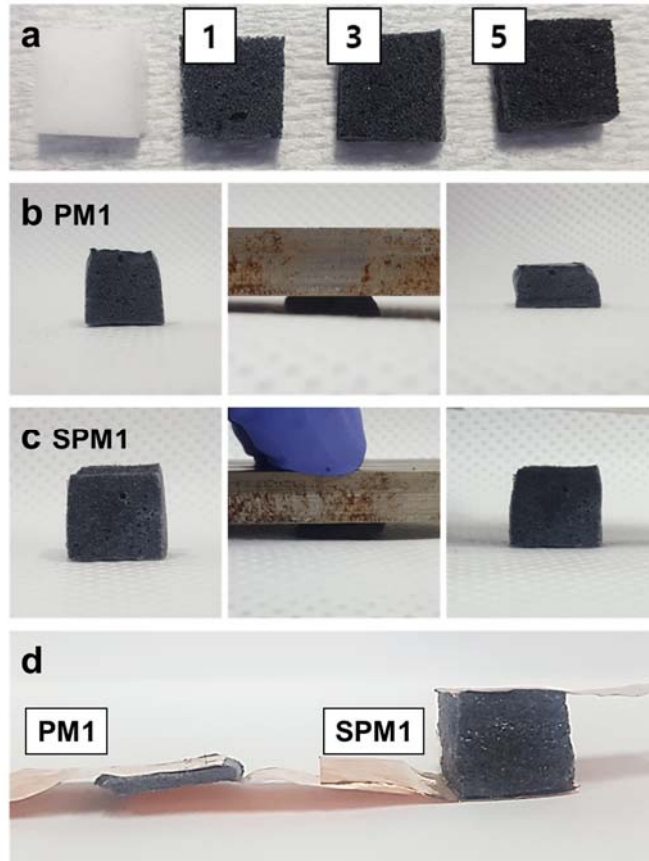


**Figure 5.12. Digital images of PM and SPM. (a) The digital image of MF and PM with different infiltration number.**

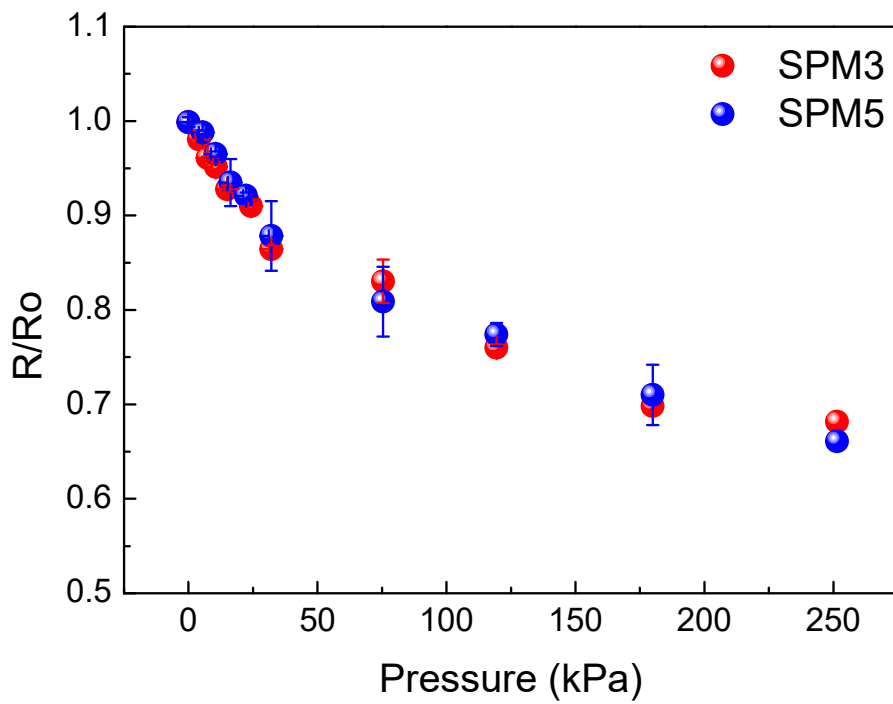


**Figure 5.13. Pressure-sensing performance of 95%-compressed SPM foams with different thickness of PEDOT:PSS conductive path.**

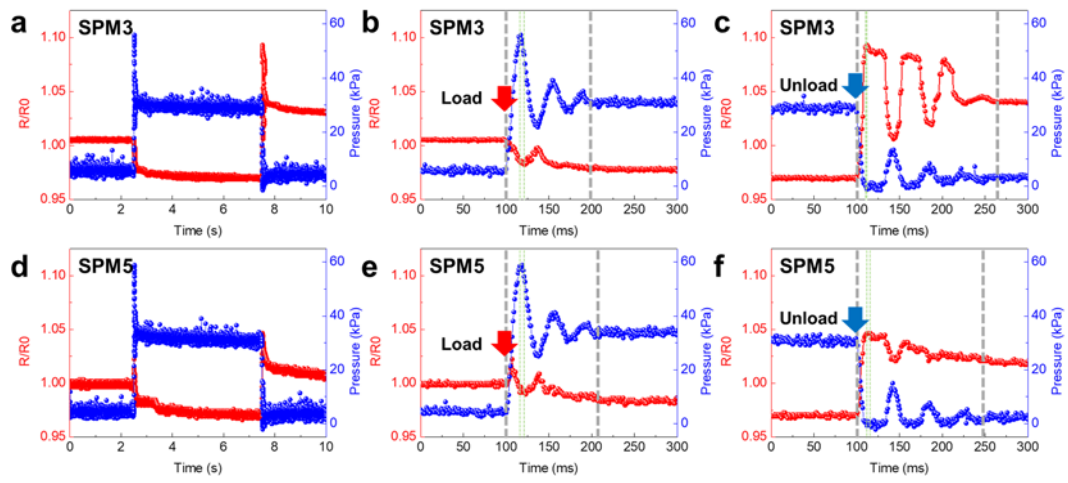


**Figure 5.14. Pressure-sensing performance of 95%-compressed SPM3 and SPM5.**

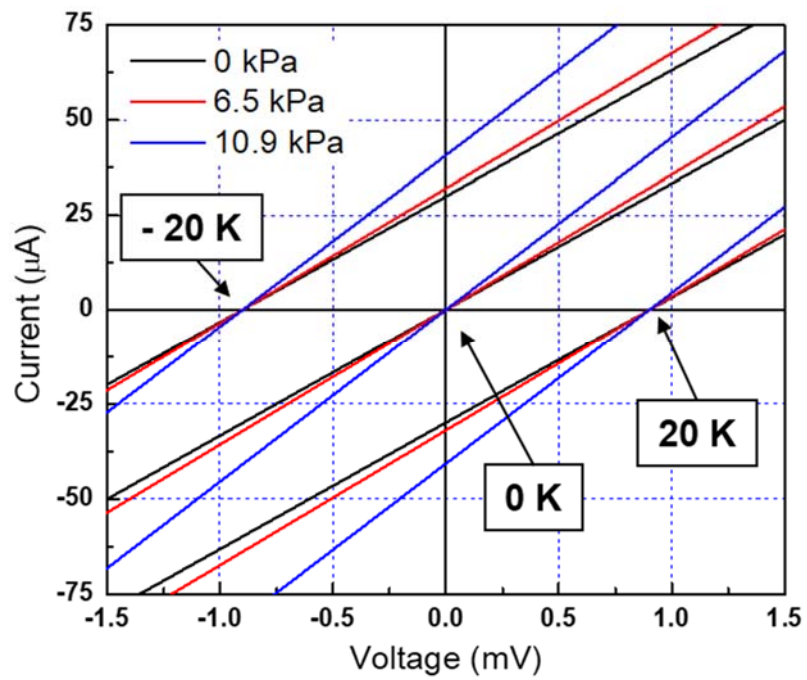


**Figure 5.15. The measured I-V curves of self-powered pressure sensor based on 9 of SPM5 cells.**

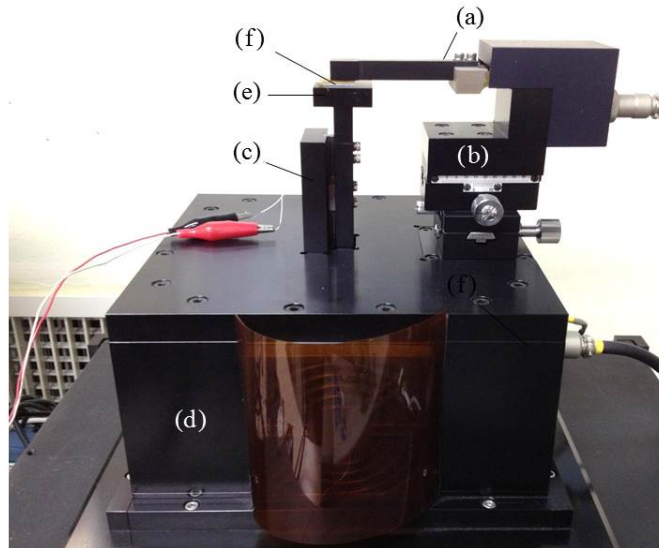


**Figure 5.16. Fatigue test setup with moving coil linear stage to evaluate the durability of the sensor**

## 초 록

본 연구에서는 블록공중합체의 나노 구조 제어를 통한 저차원 물질의 나노 패턴의 제작 및 분석 방법에 대해 기술하였다. 첫째로, 수직의 배향을 갖는 블록공중합체의 나노 구조를 제작하기 위하여 블록공중합체의 표면에 가교된 층을 도입하였다. 기존의 방법과 달리 본 연구에서 제시된 방법을 이용할 경우 다양한 종류의 블록공중합체에서 수직의 배향을 가질 것이라는 것을 세 가지 서로 다른 블록공중합체 (polystyrene-*b*-poly(methyl methacrylate) (PS-*b*-PMMA)와 polystyrene-*b*-polydimethylsiloxane (PS-*b*-PDMS), polystyrene-*b*-poly(2-vinylpyridine) (PS-*b*-P2VP))에 적용하여 증명하였다. 표면의 플라즈마 처리를 통하여 가교가 진행된 블록공중합체는 블록공중합체에 대하여 물리적으로 블록공중합체의 이동을 제한함으로써 수직 구조를 가지도록 유도함을 확인하였다. 또한 바닥 면까지 수직의 배향을 가지는 블록공중합체 나노 구조를 제시하기 위해 상부와 하부 모두 가교 층을 도입하였다. 하부의 가교된 블록공중합체

층은 중립의 표면에너지를 가지므로 블록공중합체에 대해 효과적으로 수직 구조를 제시할 수 있다. 해당 방법은 쉽고 빠른 시간에 넓은 영역에서 어떠한 블록공중합체에도 적용이 가능하기 때문에 다양한 나노 구조를 도입하기에 적합한 방법이다.

둘째로 10 나노 이하의 그래핀 나노메쉬 구조를 블록공중합체 나노 패턴 방식으로 제작하여, 뛰어난 열전 성능과 낮은 열 전도도를 가진다는 것을 밝혔다. 10 나노 미터의 크기를 가지는 그래핀 나노 구조(나노 리본 혹은 나노메쉬)는 양자 감금 효과와 포논 가장자리산란으로 인해 전기적 특성뿐만 아니라 열 전도성 및 열전 특성이 크게 변화될 것으로 예상된다. 블록공중합체의 자기 조립으로 대면적, 10나노 이하의 단일 및 이중 층 그래핀 나노메쉬를 제작하고, 열전도도와 열전성능 및 전기 전달 특성을 측정하여 양자 감금, 포논 가장자리 산란 및 교차 평면 커플링의 효과를 확인하였다. 그래핀 나노구조의 열 전도도를 측정하기 위해 공중에 띄운 후 열전도도를 측정하였으며, 다양한 샘플 중에서 8 나노미터의 폭을 갖는 이중 층 그래핀 나노메쉬는  $78 \text{ W} \cdot \text{m}^{-1} \cdot \text{K}^{-1}$  로 매우 낮은 열전도도를 가짐을 확인하였다. 또한 열전 특성 또한  $-520 \mu\text{V} \cdot \text{K}^{-1}$ 의 높은 값을 가지는 것을 확인하였으며, 이러한 결과는 고전 역학 및 쿼텀-메카니컬 시뮬레이션을 통해 결과를 뒷받침

할 수 있다.

마지막으로 앞선 연구에서 진행한 열전 물질의 성능과 열전 구조 제어의 기술을 바탕으로 열전 발전에 직접적으로 적용하기 위하여 셀룰러 구조를 가지는 멜라민 폼과 PEDOT:PSS 의 복합체를 제조하여, 자가 발전형 압력 센서로 적용이 가능함을 확인하였다. 본 연구에선 신체 활동을 감지하기 위한 센서로서, 장기간 사용하기에 적합한 자가발전형 압력센서로의 적용을 하였다. 전도성 고분자를 기반으로 하며 동시에 압력센서로 적용이 가능한 방법을 적용하였으며 기계적인 안정성과 압력센서의 민감도를 증가시키기 위하여 poly(styrene-ethylene/butylene-styrene) (SEBS)-poly(3,4-ethylenedioxythiophene):poly(styrenesulfonate) (PEDOT:PSS)-melamine foam (MF) 의 삼중 구조를 제안하였으며, 고감도, 고효율의 자가발전형 압력센서로서의 거동이 보임을 확인하였다. 특히 기존의 보고된 적 없는 삼중 구조를 제안함으로써 높은 기계적 안정성과 복원력을 보인다는 것을 확인하였다. 삼중 구조를 가지는 열전 소재는 열전발전모듈로 조립되어, 외부 전원 공급 장치 없이 팔뚝에서 340 nW의 발전 효율을 보임을 확인하였다.

주요어: 블록공중합체, 나노 패턴, 그래핀, 이황화몰리브덴, 헤테로구조,  
구조제어, 열전, 열전도도, 웨어러블, 압축 센서

학번: 2014-30252

성명: 오진우